Novel Quantum Devices for Computation and Sensing

By

Abigail Shearrow

A dissertation submitted in partial fulfillment
of the requirements for the degree of

Doctor of Philosophy
(Physics)

at the
UNIVERSITY OF WISCONSIN-MADISON
2025

Date of final oral examination: 02/04/2025

The dissertation is approved by the following members of the Final Oral Committee:
Robert McDermott, Professor, Physics
Britton Plourde, Professor, Physics
Peter Timbie, Professor, Physics
Jennifer Choy, Professor, Electrical and Computer Engineering

Efforts, partial and unsatisfactory, 123

—Helen Mirra, *Instance the Determination*

Abstract

Josephson junction-based devices have demonstrated utility in a breadth of applications ranging from quantum computation to sensing and metrology. In this thesis we introduce two novel superconducting devices: a mm-wave detector utilizing a Josephson junction for impedance matching to free space to enhance power absorption efficiency and a protected qubit relying on engineered composite Josephson elements. First we introduce a novel quantum sensor, consisting of impedance-matched Josephson junction-based slot antennas embedded in a microwave kinetic inductance detector. We discuss operating principles and design of such devices. We present data on the response of devices to a thermal quasiparticle distribution and the calibration of the detector using a blackbody source. And finally spectroscopic characterization of the devices with a Josephson emitter. In the second part of this thesis we describe work toward the design, control, and characterization of a novel protected qubit, the charge-parity qubit, consisting of a composite pi-periodic Josephson element shunted by a large capacitance. Such a device provides protection against local noise at the hardware level and aspires to substantially reduce the overhead needed for quantum error correction. Together these projects demonstrate the versatility of the Josephson junction to superconductive quantum devices.

Acknowledgments

Many people made this possible. A few are noted here, but this list is by no means exhaustive.

I am immensely thankful to have had Robert McDermott as my advisor. In my time in the McDermott lab Robert always pushed me to become a better, more well-rounded researcher. When I was deciding where to go for graduate school I knew I wanted to be in a lab where I would have the opportunity to be involved in ever piece of my PhD project from simulation and design to fabrication and measurement, and I could not have ended up in a better lab from that perspective. Robert encouraged me to do things I did not think I was capable of and I would not be the researcher I am today without his guidance. I'd also like to thank Britton Plourde for years of kindness and guidance, particularly on the topological project. I wish we'd overlapped more in Wisconsin.

I am indebted to Brad Christensen, Ed Leonard, Alex Opremcak, Chris Wilen, and Chuan-Hong (Vincent) Liu for patiently answering my questions and building a scalable lab. And to Sohair Abdullah, Shravan Patel, Matthew Snyder, Spencer Weeden, Gabe Spahn, Elam Blackwell, Rupesh Kannan, Le-Chih Cho and Yutaka Takeda for making the lab a fun and constructive place to work. Their enthusiasm and willingness to share the burden of any lab activity is a great asset to the McDermott lab.

David Harrison joined the lab as a post-doc at the end of my third year, bringing so much kindness and positivity to the lab while also being one of the most amazing experimentalists I've had the opportunity to work closely with. Whether it was pushing through a last minute fab run the day before a cleanroom shutdown or turning around the Leiden fridge twice in one week, working closely with Dave on the detector project always inspired me to work hard and have fun doing it. Also, thank you for teaching me that sometimes a hack saw is the best solution and working experiments aren't necessarily pretty experiments.

Similarly, I am thankful to Gabriel Bernhardt, for helping me through what felt like a never-ending barrage of equipment failures (a catastrophic circulating pump failure,

premature tip seal replacements, deposition tool repairs, and a compressor logic board replacement, to name a few) at the end of my PhD. I would not have finished this PhD on time without his invaluable technical support.

Nate Earnest-Noble instilled in me a powerful intuition for fabrication, layout, and design at the very start of my career, the benefits of which have been immeasurable. Without his kindness and support I would not have pursued a research career after undergrad. I'd like to thank David Schuster. The two years I spend pursuing research full-time in his lab after undergrad but before graduate school were integral to my decision to pursue a research career working on superconducting qubits. Further thanks are owed to my other Schuster lab friends: Akash Dixit, Ravi Naik, Gerwin Koolstra, Vatsan Chakram, and Sasha Anferov, who showed me that experimental physics research can be a joyful communal experience. Long live the pit!

Lisa Everett's friendship is quite possibly the best thing to come out of my time in Wisconsin. Without her constant kindness, support and encouragement from day one I would not have found the strength to finish this degree.

I am thankful to my parents, Kim and Fritz Shearrow, and my sister, Amelia Shearrow, for always encouraging and supporting me to pursue whatever I was interested in. While we were physically far apart during my PhD they found ways to support me nonetheless, just as they always have. I'm grateful for their support while I was unexpectedly stranded at their house in Atlanta, GA at the beginning of the pandemic and for the times they came to visit me in Madison, WI. I am thankful for their guidance in navigating my job offers last summer and I am particularly grateful for their help planning a wedding four months before I defended.

Finally, I'm thankful to Xavier Zahnle for sticking with me through four years of undergrad, our respective PhDs (including six years long-distance), a pandemic, and countless work-related and personal obstacles. I cannot express how fortunate I am to have had his unwavering support all these years.

Contents

Chapter 1

Josephson junction based quantum devices

Since their proposal by B. D. Josephson in 1962 [1] and subsequent demonstration by P. W. Anderson and J. M. Rowell in 1963 [2] Josephson junctions have prompted a flourishing field of research. They have found utility in applications including but not limited to: metrology, spectroscopy, sensing, and quantum computation. In this thesis we report on two novel quantum devices that demonstrate the utility and breadth of application of the Josephson junction. In this Chapter we introduce the Josephson junction, starting with the DC and AC Josephson effects. From these equations we derive the Josephson frequency, which makes a reappearance in Chapter 6 in the context of a transmit-receive experiment to characterize the spectral response of the quantum sensor discussed in the first half of this thesis. We go on to derive the Josephson inductance and Josephson energy, which are critical to the design and operation of the composite Josephson elements discussed in the second half of this thesis (starting from Chapter 8). Particulars of the junction fabrication process are left to Appendix B.1.

Consider the case of two superconducting films in close proximity with one another (shown in Fig. 1.1 (a)). The macroscopic superconducting state of each superconductor

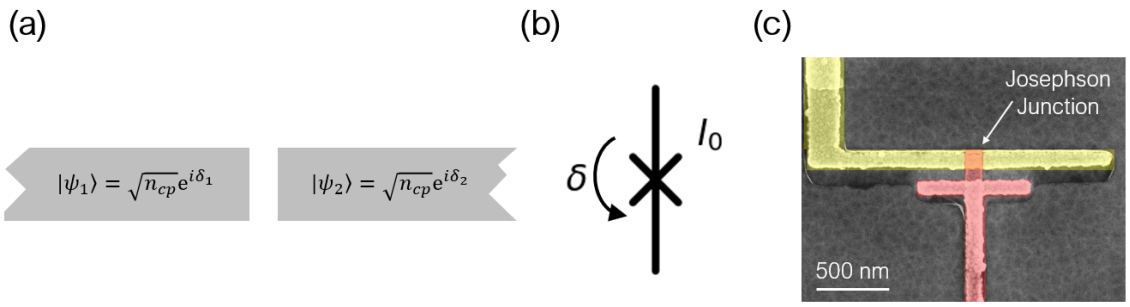

Figure 1.1: (a) A Josephson junction is two superconductors separated by a weak link. The overlap in the wavefunctions of the two superconductors allows for tunneling of Cooper pairs across the barrier. (b) Circuit element representation of the Josephson junction. I_0 is the junction critical current. δ is the phase difference across the junction. (c) Scanning electron micrograph of an Al-AlOx-Al Josephson junction, deposited via double-angle evaporation. The junction (orange) exists where the two superconducting electrodes (false color red and yellow) overlap.The weak link is a layer of aluminum oxide, a few nm thick, grown *in situ*.

can be described by the wavefunction [3, 4]

$$|\psi_{1,2}\rangle = \sqrt{n_{cp}}e^{i\delta_{1,2}} \tag{1.1}$$

where n_{cp} is the density of Cooper pairs, the charge carriers in the superconductor, and δ is the superconducting phase. In this case, it is convenient to work in terms of the difference between the two superconducting phases, $\delta = \delta_1 - \delta_2$. If there is sufficient overlap in the wavefunctions of the two superconducting states (a weak link), then it is possible for Cooper pairs to tunnel across the barrier, resulting in a supercurrent.

The electrical behavior of the Josephson junction, this weak link between two superconductors, is described by the Josephson relations [1]. The characteristic sinusoidal current-phase relation

$$I = I_0 \sin\delta \tag{1.2}$$

describes the supercurrent flowing across the Josephson junction. I_0 is the junction's critical current, while the voltage phase relation

$$2eV = \hbar\frac{\partial\delta}{\partial t} \tag{1.3}$$

describes the rate of change of the phase for a voltage, V, applied across the junction. It is sometimes convenient to rewrite Eq. 1.3 in terms of the flux quantum, $\Phi_0 = h/2e$

$$V = \frac{\hbar}{2e}\frac{\partial\delta}{\partial t} = \frac{\Phi_0}{2\pi}\frac{\partial\delta}{\partial t}. \tag{1.4}$$

Differentiating the first Josephson relation with respect to time

$$\frac{dI}{dt} = I_0 \cos\delta \frac{d\delta}{dt} \tag{1.5}$$

and substituting into the second relation, we have

$$V = \frac{\Phi_0}{2\pi}\frac{1}{I_0\cos\delta}\frac{dI}{dt}. \tag{1.6}$$

Recall the definition of an inductance,

$$V = L\frac{dI}{dt} \tag{1.7}$$

the ratio between the rate of change of the current and the voltage. Noting the similarity between the two expressions we see that the Josephson junction will represent a nonlinear inductance,

$$L(\delta) = \frac{\Phi_0}{2\pi}\frac{1}{I_0\sin\delta} = \frac{L_J}{\sin\delta} \tag{1.8}$$

where $L_J = \Phi_0/2\pi I_0$ is the Josephson inductance. The nonlinearity of the Josephson junction is a critical ingredient for the construction of superconducting qubits [5]. The junction's critical current is related to the normal state resistance, R_n

$$I_0 = \frac{\pi\Delta}{2eR_n}\tanh\left(\frac{\Delta}{2k_BT}\right) \tag{1.9}$$

where $\Delta = 1.76k_BT_c$ is the superconducting energy gap at zero temperature [3]. In the

low temperature limit, $T \ll T_c$ this reduces to [6]

$$I_0 = \frac{\pi\Delta}{2eR_n}. \tag{1.10}$$

This is the Ambegaokar-Baratoff relation which allows us to relate the Josephson inductance to the normal state resistance,

$$L_J = \frac{\hbar R_n}{\pi\Delta} \tag{1.11}$$

and by extension the Josephson energy (derived below). This is incredibly useful as it allows us to estimate the junction's energy scales from room temperature measurements of the normal state resistance.

One can then calculate the potential energy,

$$U = \int IV dt \tag{1.12}$$

from the Josephson relations.

$$U(\delta) = \int I_0 \sin\delta \frac{\Phi_0}{2\pi} d\delta = -\frac{I_0\Phi_0}{2\pi}\cos\delta \equiv -E_J\cos\delta \tag{1.13}$$

where $E_J = I_0\Phi_0/2\pi$ is the Josephson energy. Alternately, we can rewrite the Josephson energy in terms of the Josephson inductance,

$$E_J = \left(\frac{\Phi_0}{2\pi}\right)^2 \frac{1}{L_J}. \tag{1.14}$$

The Josephson junction will have some capacitive energy associated with it, depending on the area of the superconducting electrodes and the distance between them.

$$E_C = \frac{e^2}{2C_J}. \tag{1.15}$$

This is especially easy to see in the case of a junction where the weak link is an insu-

lating barrier. For instance, Al-AlOx-Al Josephson junctions deposited via double-angle evaporation (Fig. 1.1 (c)) will have some overlap capacitance associated with them due to the nature of their construction. For small-area Josephson junctions, this capacitance can be non-negligible. Together the Josephson energy, E_J, and the charging energy, E_C, determine behavior of superconducting circuits such as the Transmon qubit [5]. Starting in Chapter 8 we see how these energies, along with a linear inductive energy, E_L, (implemented as an array of large-area Josephson junctions [7]) can be used to design quantum circuits to engineer a desired potential landscape.

Finally, we can consider the temporal dynamics of the Josephson junction. Considering the case of a constant applied voltage, we can solve Eq. 1.3 for the time-dependent phase

$$\frac{2eV}{\hbar} = \frac{d\delta}{dt} \tag{1.16}$$

$$\delta(t) = \frac{2eV}{\hbar}t. \tag{1.17}$$

Substituting into the current-phase relation

$$I = I_0 \sin\left(\frac{2eV}{\hbar}t\right) \tag{1.18}$$

we see that a constant applied voltage will result in an oscillating current. Hence a voltage-biased Josephson junction will emit radiation at

$$f_J = \frac{2eV}{h} \tag{1.19}$$

the Josephson frequency. Evaluating the physical constants, $2e/h \approx 484$ GHz/mV, we see that for an applied DC bias voltage of 1-10 mV the junction will emit radiation in the mm-wave to THz regime. In Chapter 6 we show how this effect can be used to probe the spectral response of a novel mm-wave sensor. Finally, two analogies which are useful for understanding the dynamics of Josephson junctions are the driven pendulum and the tilted washboard potential [3]. However, within the scope of this thesis we constrain

ourselves to a relatively simple treatment of the Josephson junction, preferring to focus on applications.

The remainder of this thesis is split into two parts, each discussing the design, fabrication and operation of a novel Josephson junction-based quantum device. First, we discuss operation and design of a novel Josephson mm-wave quantum sensor. The sensor, a pair-breaking detector, is sensitive to changes in the quasiparticle distribution of the superconductor. We investigate response of the detector to a thermal quasiparticle distribution (Chapter 4) before calibrating the detector performance with a blackbody emitter (Chapter 5). Finally, we expose the detector to radiation emitted by a voltage-biased Josephson junction, to monitor the spectral response (Chapter 6). The second part of this thesis is concerned with work towards the development of a novel topologically protected qubit. Operation of this device relies on composite π-periodic Josephson elements, called plaquettes. We begin the second part of the thesis by motivating the need for protection at the hardware level, and aspiring to elucidate the origins of protection in this circuit (Chapter 8). We discuss construction of these composite Josephson elements (Chapter 9), as well as their design and control (Chapter 10). We present data on initialization of the devices and spectroscopy of higher excited states, and discuss steps towards coherent control of the devices (Chapter 11). The dissimilarity of these two projects demonstrates diversity of applications in which the Josephson junction finds utility.

Part I

Josephson mm-wave detectors

Chapter 2

Operating principles

The purpose of this chapter is to elucidate how a superconducting resonator can be used to detect changes in the quasiparticle distribution of a superconductor. We start by introducing the concept of quasiparticle excitations[1].We then introduce the complex surface impedance [8] of the superconducting film and its relation to the complex conductivity [9–11] before working through the circuit model description of the detector, relating the changes in the real and imaginary parts of the complex conductivity to the experimental observables: amplitude and phase. We conclude by discussing strategies to improve coupling to pair breaking radiation, in particular the addition of an antenna to aid absorption of pair-breaking radiation.

2.1 Superconductivity: Cooper pairs and quasiparticles

When cooled below the critical temperature, T_c, electrons pair, forming Cooper pairs, which condense into a macroscopic quantum state [12]. Cooper pairs allow for the lossless flow of current through the superconducting film, a hallmark of superconductivity [4, 13, 14]. In addition to Cooper pairs, there exist excitations out of the superconducting ground state, called quasiparticles. Quasiparticles are generated when energy greater than twice

[1]More correctly called Bogoliubov quasiparticles or Bogoliubons, but referred to as quasiparticles in this thesis

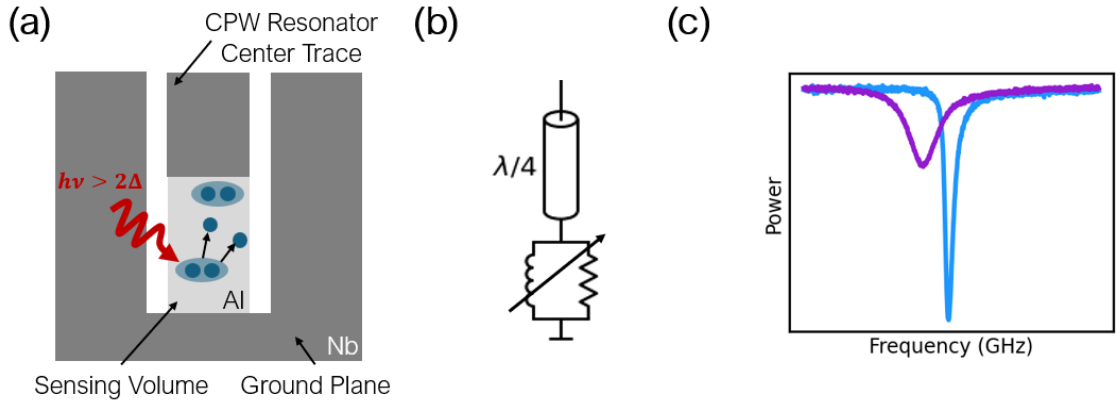

Figure 2.1: (a) Pair-breaking radiation ($hf > 2\Delta$) is absorbed by the superconductor, providing sufficient energy to break a Cooper resulting in two quasiparticle excitations. We employ a hybrid design consisting of a coplanar waveguide whose center conductor and ground plane are both niobium with an aluminum sensing volume at the current anti-node. (b) The pair-breaking detector consists of a superconducting resonator, shunted to ground via a high kinetic inductance nanowire. This nanowire can be modeled as an inductor in parallel with a resistor, the values of which are related to the quasiparticle distribution in the sensing volume via the Mattis Bardeen integrals [15] (c) Absorption of pair-breaking radiation results in a change in the quasiparticle distribution of the sensing volume, thus modifying the inductance and resistance. A change in inductance results in a shift in the frequency, and a modification of the resistance results in the resonator loss.

the superconducting gap[2], Δ, is absorbed, providing sufficient energy to break a Cooper pair resulting in the creation of two quasiparticles. Often, this pair-breaking energy is provided by the absorption of a photon with energy greater than 2Δ, although it can also be due to phonon-interactions [16]. The number of quasiparticles per unit volume in a superconductor is given by [17]

$$n_{qp} = 2N_0 \int_{\Delta}^{\infty} \rho(E) f(E) dE \tag{2.1}$$

where N_0 is the single spin density of states at the Fermi level [3] , and $\rho(E) = E/\sqrt{E^2 - \Delta^2}$ is the normalized quasiparticle density of states, with E the quasiparticle energy. For low

[2] $\Delta/e = 190\,\mu$V for aluminum.
[3] $N_0 = 1.72 \times 10^{10}\,\mu\text{m}^3\text{eV}^{-1}$ for aluminum [18].

temperatures ($k_BT \ll \Delta$) this simplifies to [19]:

$$n_{qp} = 2N_0\sqrt{2\pi k_B T\Delta}e^{-\Delta/k_BT}. \tag{2.2}$$

One may also work with the total number of quasiparticles, $N_{qp} = n_{qp}V$ or the reduced quasiparticle density [17], $x_{qp} = n_{qp}/n_{cp}$ where n_{cp} is the density of Cooper pairs. The reduced quasiparticle density is particularly useful as it is independent of geometry, and has an approximate analytical form [20]

$$x_{qp} \approx \sqrt{2\pi k_B T/\Delta}e^{-\Delta/k_BT}. \tag{2.3}$$

Once generated, quasiparticles will stay in the superconducting film until they recombine. For a thermal distribution of quasiparticles, the recombination time is given by [21]

$$\tau_{qp} = \frac{\tau_0}{\sqrt{\pi}}\left(\frac{k_BT_c}{2\Delta}\right)^{5/2}\sqrt{\frac{T_c}{T}}e^{\Delta/k_BT} \tag{2.4}$$

where $\tau_0 = 438$ ns [21] is the electron-phonon interaction time for aluminum. Note that due to the exponential dependence on temperature in both Eq. 2.2 and Eq. 2.4, the product of the number of quasiparticles and the quasiparticle lifetime will be independent of temperature

$$N_{qp}\tau_{qp} = \frac{\tau_0 N_0 (k_BT_c)^3 V}{2\Delta^2}. \tag{2.5}$$

We will revisit this in Chapter 4.

2.2 Surface impedance and the complex conductivity

Bardeen[4], Cooper, and Schrieffer introduced the microscopic theory of superconductivity in their seminal 1957 paper [12]. They define a complex conductivity describing the

[4]John Bardeen was born in Madison, Wisconsin and is buried in the Forest Hill Cemetery.

electrical response of a superconducting film,

$$\sigma = \sigma_1 - j\sigma_2. \tag{2.6}$$

The expressions for the real and imaginary parts of the complex conductivity are given by the Mattis Bardeen integrals [15]

$$\frac{\sigma_1}{\sigma_n} = \frac{2}{\hbar\omega}\int_{\Delta}^{\infty} \frac{[f(E) - f(E+\hbar\omega)](E^2 + \Delta^2 + \hbar\omega E)}{\sqrt{E^2+\Delta^2}\sqrt{(E+\hbar\omega)^2+\Delta^2}} dE \tag{2.7}$$

$$\frac{\sigma_2}{\sigma_n} = \frac{1}{\hbar\omega}\int_{\Delta-\hbar\omega}^{\Delta} \frac{[1 - 2f(E+\hbar\omega)](E^2 + \Delta^2 + \hbar\omega E)}{\sqrt{\Delta^2-E^2}\sqrt{(E+\hbar\omega)^2-\Delta^2}} dE \tag{2.8}$$

where $f(E)$ is the energy distribution the quasiparticles and σ_n is the normal state conductivity. For a thermal distribution of quasiparticles these expressions evaluate to

$$\frac{\sigma_1(T)}{\sigma_n} = \frac{4\Delta}{hf} e^{-\Delta/k_BT} \sinh\left(\frac{hf}{2k_BT}\right) K_0\left(\frac{hf}{2k_BT}\right) \tag{2.9}$$

$$\frac{\sigma_2(T)}{\sigma_n} = \frac{\pi\Delta}{hf}\left[1 - \sqrt{\frac{2\pi k_BT}{\Delta}} e^{-\Delta/k_BT} - 2e^{-\Delta/k_BT} e^{-hf/2k_BT} I_0\left(\frac{hf}{2k_BT}\right)\right] \tag{2.10}$$

where I_0 and K_0 are the modified Bessel functions of the first and second kind, respectively. Derivations can be found in [9, 10]. The real and imaginary parts of the complex conductivity can be related to the surface impedance of the superconductor,

$$Z_s = R_s + j\omega L_s = \sqrt{\frac{i\mu_0\omega}{\sigma_1 - j\sigma_2}} \tag{2.11}$$

for a bulk superconductor (film thickness, $d \gg \lambda_L$, the London penetration depth) in the local limit [8]

$$R_s = \sqrt{\frac{\mu_0\omega}{\sigma_2}}\frac{\sigma_1}{2\sigma_2} = \mu_0\omega\lambda_L\frac{\sigma_1}{2\sigma_2} \tag{2.12}$$

$$L_s = \sqrt{\frac{\mu_0}{\omega\sigma_2}} = \mu_0\lambda_L. \tag{2.13}$$

In the case of film of finite thickness, d, there is a correction to Eq. 2.11 [8]

$$Z_s = \sqrt{\frac{i\mu_0\omega}{\sigma_1 - j\sigma_2}} \coth\left(\frac{d}{\lambda_L}\sqrt{1 + j\frac{\sigma_1}{\sigma_2}}\right) \tag{2.14}$$

in which case Eq. 2.12 and Eq. 2.13 become [10]

$$R_s = \mu_0\omega\lambda_L \frac{\sigma_1}{2\sigma_2}\beta \coth(d/\lambda_L) \tag{2.15}$$

$$L_s = \mu_0\lambda_L \coth(d/\lambda_L) \tag{2.16}$$

defining

$$\beta = 1 + \frac{2d/\lambda_L}{\sinh(2d/\lambda_L)}. \tag{2.17}$$

In the following Sections, we will return to these expressions when we derive the change in frequency and internal quality factor of the resonator due to a change in the quasiparticle distribution of the superconductor. We further relate the change in experimental observables, amplitude and phase, to a change in the internal quality factor and frequency.

2.3 Pair-breaking detector: a simple circuit model

The detector developed in this thesis is a type of microwave kinetic inductance detector. It consists of a quarter wave coplanar waveguide (CPW) resonator shunted to ground via a high kinetic inductance nanowire. This nanowire can be modeled as an inductance, L_k, in parallel with a resistor, R_{qp}. The inductance is due to the inertia of the Cooper pairs while the resistance is due to the quasiparticle excitations. These quantities can be related to the Mattis Bardeen expressions for the real and imaginary parts of the complex conductivity [15]. In this section, working from this circuit model, we derive expressions for the change in the resonator loss, $1/Q$ where Q is the quality factor, and the fractional frequency shift, f/f_0. We then relate these quantities to the change in amplitude, A, and phase, θ, (observables in our experimental system).

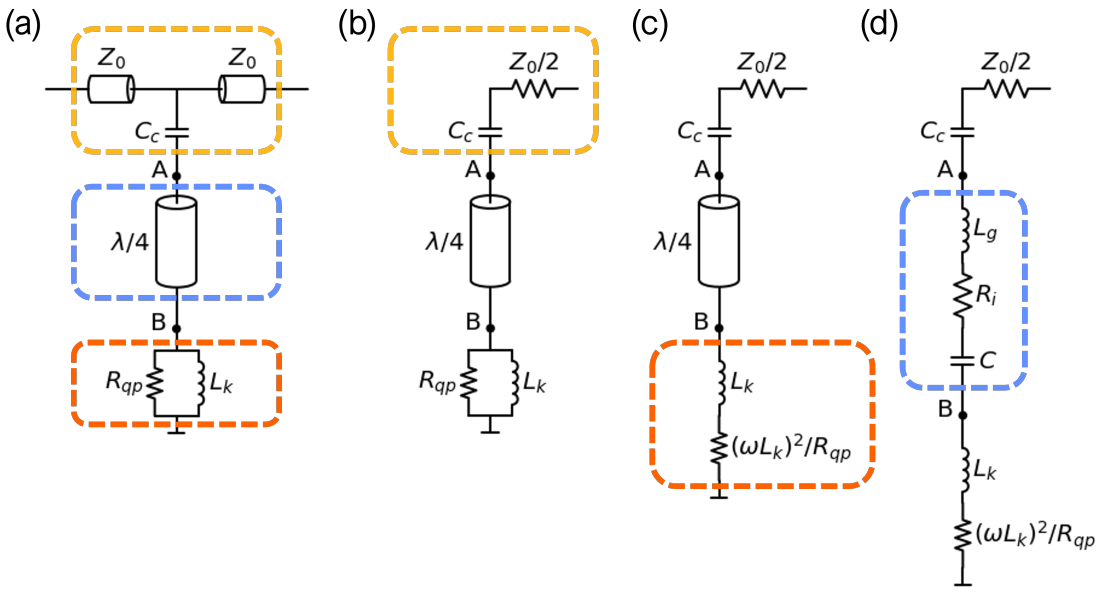

Figure 2.2: Circuit model of the Josephson mm-wave detector. (a) Capacitively coupled quarter wave coplanar waveguide resonator shunted to ground via a high kinetic inductance nanowire. The nanowire is modeled as an inductor in parallel with a resistor. The coupling circuit is indicated with a yellow box. The quarter wave resonator is indicated in blue, and the nanowire is shown in orange. (b) Assuming that the input and output impedance are the same, the coupling circuit can be rewritten as a resistor in parallel with the coupling capacitor, C_c. (c) The series-to-parallel mapping (see Appendix A.1 for details) applied to the nanowire circuit. (d) From the standpoint of the nanowire, the quarter wave resonator looks like an open circuit and can thus be mapped to a series LCR circuit [22] L_g is the geometric inductance, R_i the internal loss, and C the geometric capacitance.

2.3.1 Derivation of $\delta(1/Q_i)$ and $\delta f/f_0$

Fig. 2.2 (a) shows the full circuit representation of our detector. The coupling circuit, including the coupling capacitor, C_c and the feedline, with characteristic impedance $Z_0 = 50\,\Omega$ is shown in yellow. The $\lambda/4$ CPW resonator is shown in blue, and the nanowire circuit is indicated in orange. Assuming that the input and output impedance of the feedline is the same, we can rewrite the coupling circuit as is shown in Fig. 2.2 (b). An appealing feature of microwave kinetic inductance detectors that extends to our detector design is that frequency multiplexing allows for the creation of kilopixel arrays. Efficient frequency multiplexing requires a clear understanding of how the combined circuit resonates. The discussion of the coupling circuit is left to Appendix A.2. For the purposes of calculating the change in the resonator loss and the factional frequency shift we disregard the coupling circuit momentarily.

Starting from the circuit shown in Fig. 2.2(b), we map the parallel resistance, R_{qp}, and inductance, L_k, to an equivalent series resistance and inductance (see Appendix A.1 for details). In the high Q limit, the series inductance, $L_{\text{series}} \approx L_k$ and the series resistance $R_{\text{series}} \approx (\omega L_k)^2/R_{qp}$. The equivalent circuit is shown in Fig. 2.2(c). From the standpoint of the nanowire (node A) the capacitively coupled end of the CPW resonator looks like an open. Hence, we map the quarter wave resonator to an equivalent series LCR circuit [22] (Fig. 2.2(d)). With all circuit elements now in series, we write down an expression for the quality factor.

$$Q = \frac{\omega(L_g + L_k)}{R_{\text{series}}} = \frac{\omega(L_g + L_k)R_{qp}}{(\omega L_k)^2}. \tag{2.18}$$

Using the definition of the kinetic inductance fraction, $\alpha \equiv L_k/L_{\text{total}}$ we have

$$Q = \frac{1}{\alpha}\frac{R_{qp}}{\omega L_k} \tag{2.19}$$

Referring back to Eq. 2.12 and Eq. 2.13, we rewrite Eq. 2.19 in terms of the Mattis Bardeen expressions

$$Q = \frac{2}{\alpha\beta}\frac{\sigma_2}{\sigma_1} \tag{2.20}$$

Assuming that other loss channels in the resonator are low, this quality factor will dominate the internal quality factor, Q_i, of the resonator. Furthermore a change in the internal quality factor will be due to a change in the quasiparticle distribution of the nanowire. In the case of a thermal quasiparticle distribution, we can write down an expression for the change in the quality factor $\delta(1/Q)$.

$$\delta\left(\frac{1}{Q}\right) = \frac{1}{Q(T)} - \frac{1}{Q(T=0)} = \frac{\alpha\beta}{2}\left[\frac{\sigma_1(T)}{\sigma_2(T)} - \frac{\sigma_1(T=0)}{\sigma_2(T=0)}\right]. \tag{2.21}$$

Using the fact that for $T \ll T_c$, $\delta\sigma_2 \ll \delta\sigma_1$ [23] which implies $\sigma_2(T) \approx \sigma_2(T=0)$ we arrive at

$$\delta\left(\frac{1}{Q}\right) \approx \frac{\alpha\beta}{2}\frac{\delta\sigma_1}{\sigma_2}. \tag{2.22}$$

From Eq. 2.22 we see that a change in the quality factor of the detector will be due to a change in the real part of the complex conductivity and thus it is associated with the quasiparticle excitations.

We turn our attention now to finding an expression for the resonant frequency of the combined resonator-nanowire circuit. To do this we use the method of load lines. The impedance of the resonator is

$$Z_r(\omega) = R_i + j\left(\omega L_g - \frac{1}{\omega C}\right) \tag{2.23}$$

and the impedance of the nanowire is

$$Z_{nw}(\omega) = \frac{(\omega L_k)^2}{R_{qp}} + j\omega L_k. \tag{2.24}$$

On resonance, the imaginary part of the impedance at node B will be zero such that imaginary part of the nanowire impedance, $Z_{nw}(\omega)$, and the imaginary part of the resonator impedance, $Z_r(\omega)$, will cancel.

$$0 = \mathrm{Im}[Z_B(\omega)] = \left(\omega L_g - \frac{1}{\omega C}\right) + \omega L_k \tag{2.25}$$

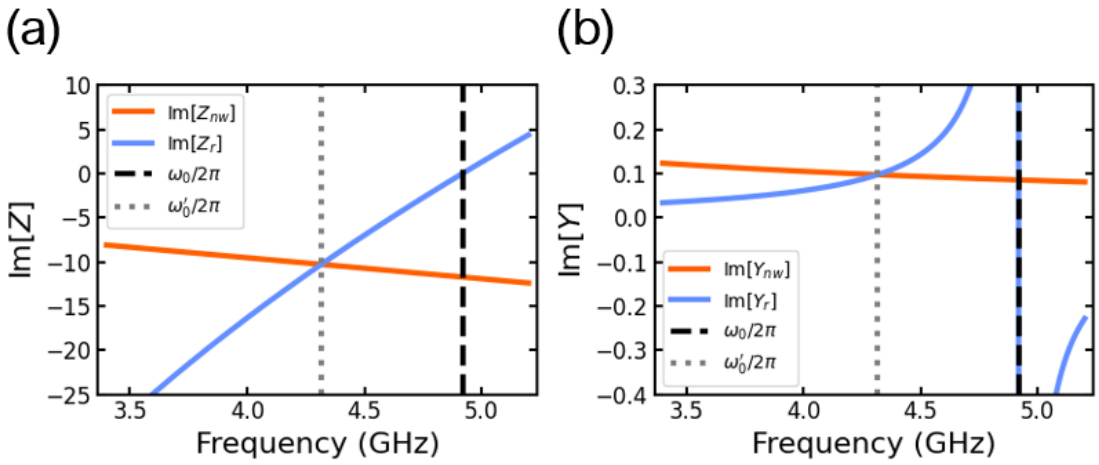

Figure 2.3: Load lines analysis for the combined resonator-nanowire circuit. (a) The imaginary part of the impedance. The imaginary part of the resonator's impedance is shown in blue. The nanowire's impedance is shown in orange. The intersection point defines the new resonance of the combined system. The gray dotted line shows the analytical expression derived in Section 2.3.1. The black dashed line shows the bare resonance of the $\lambda/4$ resonator. (b) The imaginary part of the resonator admittance (blue) and nanowire admittance (orange). The resonator has dispersive lineshape while the nanowire is monotonically decreasing. This results in two intersection points. The higher frequency corresponds to the bare quarter wave resonance. The lower frequency zero is the new resonance, including loading from the nanowire.

$$
\begin{aligned}
0 &= \omega^2(L_g + L_k)C - 1 \\
\omega^2 &= \frac{1}{(L_g + L_k)C} \\
\omega &\equiv \frac{1}{\sqrt{(L_g + L_k)C}}.
\end{aligned}
\tag{2.26}
$$

This defines a new resonance, including added inductance from the nanowire. The problem can equivalently be solved by setting the imaginary part of the admittance at node B to zero and solving for the frequency. In this case, there are two zeros. The higher frequency zero corresponds to the resonant frequency of the quarter wave resonator alone. The lower frequency zero is the resonant frequency including the nanowire. The solution is illustrated graphically in Fig. 2.3.

In the same way that we did for the quality factor, we can relate the change in the fractional frequency to a change in the complex conductivity. The change in the resonant

frequency will be due to a change in the kinetic inductance of the nanowire. We start by defining the temperature dependent resonant frequency

$$\omega(T) = \frac{1}{\sqrt{(L_g + L_k(T))C}} \tag{2.27}$$

rewriting this in terms of the change in the kinetic inductance, $\delta L_k = L_k(T) - L_k(T=0)$, we have

$$\omega(T) = \frac{1}{\sqrt{(L_g + L_k(T=0) + \delta L_k)C}}. \tag{2.28}$$

Define $L_0 = L_g + L_k(T=0)$, then

$$\omega(T) = \frac{1}{\sqrt{L_0 C(1 + \delta L_k/L_0)}} \equiv \frac{\omega(T=0)}{\sqrt{1 + \delta L_K/L_0}}. \tag{2.29}$$

For $T \ll T_c$ we have $\delta L_k/L_0 \ll 1$ allowing us to Taylor expand

$$\omega(T) \approx \omega(T=0)\left(1 - \frac{1}{2}\frac{\delta L_k}{L_0}\right). \tag{2.30}$$

Looking at the change in the fractional frequency shift,

$$\begin{aligned}
\frac{\delta\omega}{\omega_0} &= \frac{\omega(T) - \omega(T=0)}{\omega(T=0)} \\
&= \frac{\omega(T)}{\omega(T=0)} - 1 \\
&= -\frac{1}{2}\frac{\delta L_k}{L_g + L_k(T=0)} \\
&= -\frac{1}{2}\frac{\delta L_k}{L_g + L_k(T=0)}\frac{L_k(T=0)}{L_k(T=0)}
\end{aligned}$$

$$\frac{\delta\omega}{\omega_0} = -\frac{\alpha}{2}\frac{\delta L_k}{L_k(T=0)} \tag{2.31}$$

where we have used the definition of the kinetic inductance fraction

$$\alpha = \frac{L_k}{L_g + L_k}. \tag{2.32}$$

We can further relate the fractional frequency shift to the change in the imaginary part of the complex conductivity via the surface impedance (Eq. 2.11). Using the expression for the surface inductance of a bulk film from Eq. 2.13, and explicitly noting the temperature dependence,

$$\begin{aligned}\frac{\delta L_k}{L_k(T=0)} &= \frac{L_k(T) - L_k(T=0)}{L_k(T=0)} \\ &= \frac{L_k(T)}{L_k(T-0)} - 1 \\ &= \frac{\sqrt{\mu_0/\omega\sigma_2(T)}}{\sqrt{\mu_0/\omega\sigma_2(T=0)}} - 1 \\ &= \sqrt{\frac{\sigma_2(T=0)}{\sigma_2(T)}} - 1\end{aligned}$$

We play the same trick as before, rewriting $\sigma_2(T) = \sigma_2(T=0) = \delta\sigma_2$ and again making the low temperature approximation

$$\begin{aligned}\frac{\delta L_k}{L_k(T=0)} &= \sqrt{\frac{\sigma_2(T=0)}{\sigma_2(T=0)(1+\delta\sigma_2/\sigma_2(T=0))}} - 1 \\ &= \sqrt{\frac{1}{1+\delta\sigma_2/\sigma_2(T=0)}} - 1 \\ &= \left(1 - \frac{1}{2}\frac{\delta\sigma_2}{\sigma_2(T=0)}\right) - 1\end{aligned}$$

$$\frac{\delta L_k}{L_k(T=0)} = -\frac{1}{2}\frac{\delta\sigma_2}{\sigma_2(T=0)}. \tag{2.33}$$

Therefore, returning to Eq. 2.31

$$\frac{\delta\omega}{\omega(T=0)} = \frac{\alpha}{4}\frac{\delta\sigma_2}{\sigma_2(T=0)}. \tag{2.34}$$

For a finite thickness films there is an additional coth dependence [8] (see Eq. 2.14), we pick up an extra factor of $\beta = 1 + (2d/\lambda)/\sinh(2d/\lambda)$ [10] arriving at

$$\frac{\delta\omega}{\omega_0} = \frac{\omega(T) - \omega(T=0)}{\omega(T=0)} = \frac{\alpha\beta}{4}\frac{\delta\sigma_2}{\sigma_2}. \tag{2.35}$$

From Eq. 2.22 and Eq. 2.35 we see that the change in the quality factor will be mainly due to changes in the real part of the complex conductivity (due to fluctuations in the number of quasiparticles, N_{qp}). The change in the fractional frequency will be due to changes in the imaginary part of the complex conductivity and thus associated with changes in the number of Cooper pairs, N_{cp}. Of course noting that these two values are related. Having calculated the change in $\delta(1/Q_i)$ and $\delta f/f_0$ we can now relate these quantities to our experimental observables, amplitude and phase.

2.3.2 Relating $\delta(1/Q)$ and $\delta f/f_0$ to a change in amplitude and phase

For our detector, consisting of a $\lambda/4$ CPW resonator shunted to ground via a high kinetic inductance nanowire, we have derived the resonator response due to a change in the quasiparticle distribution in the nanowire. We can probe changes in these quantities experimentally by monitoring the amplitude or phase on resonance via a heterodyne measurement. In this section we relate changes in $\delta(1/Q)$ and f/f_0 to our experimental observables amplitude and phase. We start by deriving the expression for the forward scattering matrix element, S_{21}, of capacitively coupled $\lambda/4$ resonator (Fig. 2.4). Here we assume that the input and output impedance of the feedline are equal ($Z_0 = 50\,\Omega$). For discussion of how to model a small impedance mismatch, see [24]. We then relate our expression for S_{21} (depending on the internal quality factor and fractional detuning) to amplitude and phase on resonance. From here we relate $\delta(1/Q)$ and $\delta f/f_0$ to changes in amplitude and phase. The first part of this analysis follows closely an unpublished internal note by R. McDermott.

The circuit representation of a capacitively coupled $\lambda/4$ resonator is shown in Fig. 2.4 (b). The electrically open end of the quarter wave resonator, when placed sufficiently close to the feedline will have some capacitance, C_c, to the central strip of the transmission line. We assume here that the input and output impedance of the transmission line is uniformly $50\,\Omega$. The relationship between the coupling capacitance and the coupling quality factor, Q_c, is derived in Appendix A.2. From the standpoint of the coupling capacitor, the $\lambda/4$

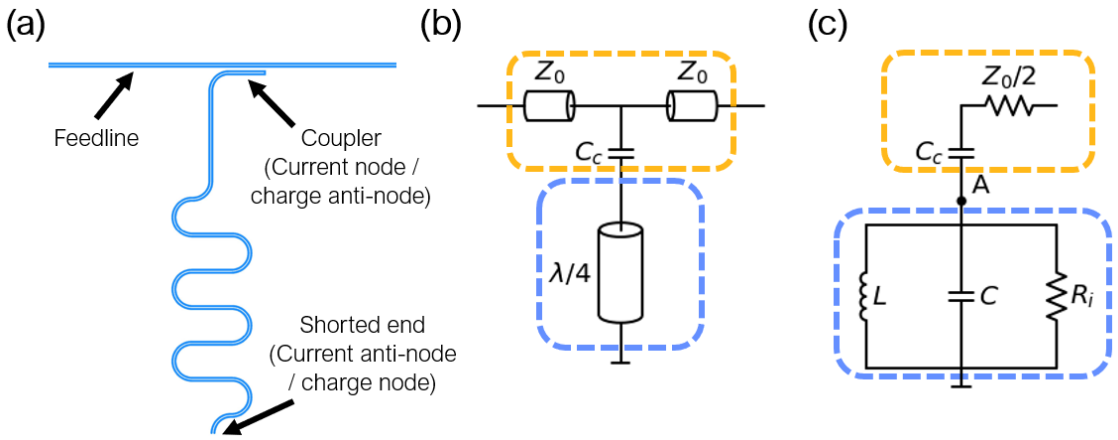

Figure 2.4: The quarter wave coplanar waveguide resonator. (a) Screen capture of the graphic design system (GDS) file of one of the hanger resonators used in this work. The device layout is defined in the GDS and transferred to the physical device in fabrication (in this case, using photolithography). Further details can be found in Chapter 3. Blue indicates areas where the superconductor is removed exposing the substrate. White areas are where superconductor remains. (b) Circuit representation of the capacitively coupled quarter wave resonator. (c) Equivalent parallel LCR tank circuit.

resonator looks like a short at the far end and can therefore be mapped to an equivalent LCR tank circuit [22]. We begin by deriving the expression for the new, loaded, resonant frequency of the combined LCR circuit and coupling circuit. To do this we employ the method of load lines.

First, we write down the expression for the admittance of the parallel LCR tank circuit

$$Y_r(\omega) = \frac{1}{R_i} + j\left(\omega C - \frac{1}{\omega L}\right). \tag{2.36}$$

We can rewrite this expression in terms of the resonant frequency, $\omega_0 = 1/\sqrt{LC}$, and the characteristic impedance of the resonator, $Z_0 = \sqrt{L/C} = \omega_0 L = 1/\omega_0 C$, along with the expression for the quality factor of a parallel LCR resonator [22], $Q_i = R_i/Z_0$. Resonators used in this work were designed to have $Z_0 = 50\,\Omega$, the same as the transmission line, so I will call both the impedance of the $\lambda/4$ resonator and the impedance of the feedline Z_0.

However, this need not necessarily be the case.

$$Y_r(\omega) = \frac{1}{Q_i Z_0} + j\frac{1}{Z_0}\left(\frac{\omega}{\omega_0} - \frac{\omega_0}{\omega}\right) \tag{2.37}$$

We define the fractional de-tuning from ω_0:

$$\delta = \frac{\omega - \omega_0}{\omega_0} \tag{2.38}$$

allowing us to simplify our expression for the admittance of the tank circuit:

$$Y_r(\delta) = \frac{1}{Z_0}\left(\frac{1}{Q_i} + j2\delta\right). \tag{2.39}$$

From Eq. 2.39 we have the expression for the impedance of the parallel LCR circuit:

$$\begin{aligned} Z_r(\delta) &= \frac{1}{Y_r(\delta)} = Z_0 \frac{1}{1/Q_i + 2j\delta}\frac{1/Q_i - j2\delta}{1/Q_i - j2\delta} \\ &= Z_0 \frac{1/Q_i - j2\delta}{1/Q_i^2 + (2\delta)^2} = Z_0 \frac{1/Q_i - j2\delta}{1/Q_i^2 + (2\delta)^2}\frac{Q_i}{Q_i} \\ &= Z_0 \frac{Q_i - 2j\delta Q_i^2}{1 + (2Q_i\delta)^2}. \end{aligned} \tag{2.40}$$

We now turn our attention to the impedance of the coupling circuit

$$Z_c(\omega) = \frac{Z_0}{2} - j\frac{1}{\omega C_c}. \tag{2.41}$$

The impedance of the combined circuit is therefore

$$Z_A(\omega, \delta) = Z_r(\delta) + Z_c(\omega) = \frac{Z_0}{2} + \frac{Z_0 Q_i}{1 + (2Q_i\delta)^2} - j\left[\frac{1}{\omega C_c} + \frac{2Z_0 Q_i^2 \delta}{1 + (2Q_i\delta)^2}\right]. \tag{2.42}$$

Looking at the circuit from the standpoint of node A (Fig. 2.4 (c)), we expect $\mathrm{Im}[Z_A]$ to have a zero on resonance. We now solve for new resonant frequency including loading

from the coupling circuit.

$$0 = \mathrm{Im}[Z_A(\delta,\omega)] = \frac{1}{\omega C_c} + \frac{2Z_0 Q_i^2 \delta}{1+(2Q_i\delta)^2} \tag{2.43}$$

$$\frac{-1}{\omega C_c} = \frac{2Z_0 Q_i^2 \delta}{1+(2Q_i\delta)^2}$$

Inverting the expression we have

$$-\omega C_c = \frac{1+(2Q_i\delta)^2}{2Z_0 Q_i^2 \delta}$$

$$-\omega C_c Z_0 = \frac{1/Q_i^2 + 4\delta^2}{2\delta}$$

$$-2Z_0 C_c \omega \delta = \frac{1}{Q_i^2} + 4\delta^2$$

Substituting back in for $\delta = \omega/\omega_0 - 1$ we have

$$-2Z_0 C_c \omega\left(\frac{\omega}{\omega_0}-1\right) = \frac{1}{Q_i^2} + 4\left(\frac{\omega}{\omega_0}-1\right)^2 = \frac{1}{Q_i^2} + 4\left[\left(\frac{\omega}{\omega_0}\right)^2 - 2\frac{\omega}{\omega_0} + 1\right].$$

We now use the definition, $Z = 1/\omega_0 C$:

$$-2\frac{C_c}{C}\frac{\omega}{\omega_0}\left(\frac{\omega}{\omega_0}-1\right) = \frac{1}{Q_i^2} + 4\left[\left(\frac{\omega}{\omega_0}\right)^2 - 2\frac{\omega}{\omega_0} + 1\right]$$

Dropping the term, $1/Q_i^2$ and making the high-Q approximation.

$$-2\frac{C_c}{C}\frac{\omega}{\omega_0}\left(\frac{\omega}{\omega_0}-1\right) = 4\left[\left(\frac{\omega}{\omega_0}\right)^2 - 2\frac{\omega}{\omega_0} + 1\right]$$

Gathering like-terms we solve for ω/ω_0.

$$0 = \frac{2C_c}{C}\left[\left(\frac{\omega}{\omega_0}\right)^2 - \frac{\omega}{\omega_0}\right] + 4\left[\left(\frac{\omega}{\omega_0}\right)^2 - 2\frac{\omega}{\omega_0} + 1\right] \tag{2.44}$$

Dividing everything by two and gathering like terms we have

$$0 = \left(\frac{C_c}{C} + 2\right)\left(\frac{\omega}{\omega_0}\right)^2 - \left(\frac{C_c}{C} + 4\right)\frac{\omega}{\omega_0} + 2. \tag{2.45}$$

Applying the quadratic formula we find the roots.

$$\begin{aligned} \frac{\omega}{\omega_0} &= \frac{\left(\frac{C_c}{C} + 4\right) \pm \sqrt{\left(\frac{C_c}{C} + 4\right)^2 - 8\left(\frac{C_c}{C} + 2\right)}}{2\left(\frac{C_c}{C} + 2\right)} \\ &= \frac{\left(\frac{C_c}{C} + 4\right) \pm \frac{C_c}{C}}{2\frac{C_c}{C} + 4} \end{aligned} \tag{2.46}$$

We take the lower frequency since this is the one that described loading by the coupling capacitor.

$$\frac{\omega}{\omega_0} = \frac{4}{2\frac{C_c}{C} + 4} = \frac{1}{1 + \frac{C_c}{2C}} \tag{2.47}$$

We define the new frequency of the coupled system to be

$$\omega_0' = \omega_0\left(\frac{1}{1 + \frac{C_c}{2C}}\right). \tag{2.48}$$

For the best signal to noise ratio (SNR), we target $Q_i \approx Q_c$ such that $Q \approx Q_i/2$. $Q_c \propto 1/C_c^2$ (see Appendix A.2 for full expression). As a result, we can make the approximation $C_c \ll C$ such that

$$\frac{\omega}{\omega_0} \approx 1 - \frac{C_c}{2C} \tag{2.49}$$

The approximate form of the loaded resonance in the high internal Q, weakly coupled limit is

$$\omega_0' = \omega_0\left(1 - \frac{C_c}{2C}\right). \tag{2.50}$$

For now, we're after the expression for transmission across the resonator. The forward

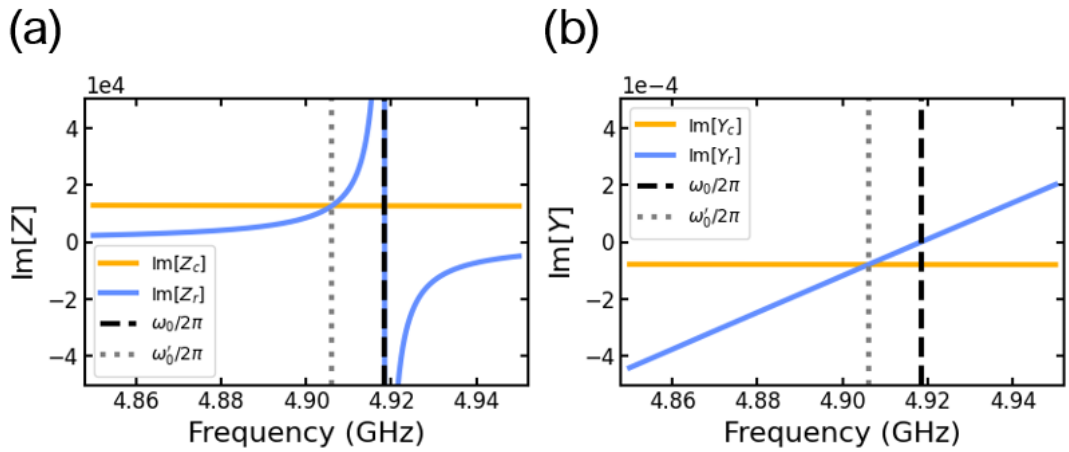

Figure 2.5: Load lines for resonator (blue) and coupling circuit (yellow). (a) The imaginary part of the impedance for the resonator and coupler. These intersect at two points. The higher frequency zero corresponds to the bare cavity resonance. The lower frequency zero is the loaded frequency of the combined resonator-coupler circuit. The bare frequency of the quarter wave resonator is indicated by the black dashed line. The analytical expression for the loaded resonance, Eq. 2.50 , is shown as a gray dotted line. (b) The imaginary part of the resonator impedance and coupler impedance.

scattering matrix element for a shunt impedance is

$$S_{21} = \frac{2}{2 + \frac{Z_0}{Z}}. \tag{2.51}$$

To evaluate this expression we need the impedance of the hanger resonator (including the coupling circuit) in terms of the de-tuning from the new resonance

$$\delta' = \frac{\omega - \omega_0'}{\omega_0'}. \tag{2.52}$$

Rewriting the expression for the total impedance of the coupling circuit and resonator in terms of the new fractional de-tuning, δ', we have

$$Z(\delta') = \frac{Q_c Z_0}{2Q_i}(1 + j2\delta - Q_i). \tag{2.53}$$

$$\frac{Z_0}{Z} = \frac{2Q_i}{Q_c}\frac{1}{1 + j2\delta' Q_i}$$

$$S_{21} = \frac{1}{1 + \frac{Q_i}{Q_c}\frac{1}{1+j2\delta' Q_i}}. \tag{2.54}$$

We rewrite this expression in terms of the loaded quality factor, Q_l,

$$\frac{1}{Q_l} = \frac{1}{Q_i} + \frac{1}{Q_c}. \tag{2.55}$$

$$\begin{aligned} S_{21} &= \frac{Q_c(1 + j2\delta' Q_i)}{Q_c(1 + j2\delta' Q_i) + Q_i} \\ &= \frac{Q_c + j2\delta' Q_l(Q_c + Q_i)}{(Q_c + Q_i)(1 + j2\delta' Q_l)} \\ &= \frac{Q_c/(Q_c + Q_i) + j2\delta' Q_l}{1 + j2\delta' Q_l} \end{aligned}$$

$$S_{21} = \frac{Q_l/Q_i + j2\delta' Q_l}{1 + j2\delta' Q_l} \tag{2.56}$$

S_{21} is the complex number describing transmission across the resonator. In Fig. 2.6 we plot this expression for $\omega_0'/2\pi = 5$ GHz, $Q_c = 1 \times 10^5$, and Q_i ranging between 1×10^5 and 1×10^6 (values representative of the devices studied in this thesis). Fig. 2.6 (a) shows the amplitude, $|S_{21}|$, displaying the expected Lorentzian lineshape. We see that the depth of the resonance gets shallower as Q_i decreases. Fig. 2.6 (b) shows the phase, $\angle S_{21}$. And in Fig. 2.6 (c) we show the real and imaginary parts of S_{21}, which sweep out a circle in the complex plane, the diameter of which decreases with Q_i.

For the case where $Q_i = Q_c$ we have $Q_l = Q_i/2 \Rightarrow Q_l/Q_i = 1/2$, the value of the circle off resonance is 1, and on resonance is $\frac{1}{2}$. The center of the circle then is located at

$$x_c = \frac{Q_l/Q_i + 1}{2}. \tag{2.57}$$

Hence, the amplitude and phase are given by [25]

$$A = \frac{\sqrt{(\mathrm{Re}[S_{21}] - x_c)^2 + \mathrm{Im}[S_{21}]^2}}{1 - x_c} \quad \text{and} \quad \theta = \arctan\left(\frac{\mathrm{Im}[S_{21}]}{x_c - \mathrm{Re}[S_{21}]}\right) \tag{2.58}$$

From Eq. 2.58 and our expression for S_{21}, keeping only first-order terms in Q_i and δ', we can write down expressions for amplitude and phase due to a change in $\delta(1/Q)$ and $\delta f/f_0$

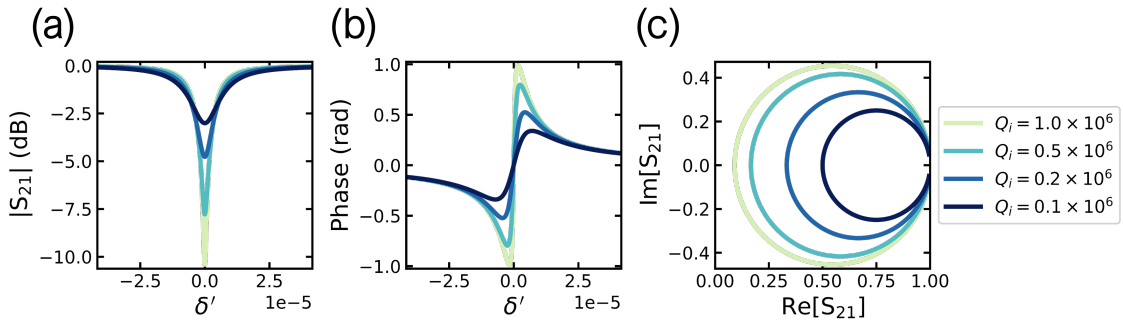

Figure 2.6: Calculated resonator response of a capacitively coupled quarter wave coplanar waveguide resonator. S_{21} is the forward scattering matrix element describing transmission across the resonator. (a) Transmission amplitude as a function of the fractional detuning from the resonant frequency, $\delta' = (\omega - \omega_0)/\omega_0$. (b) Phase as a function of δ'. (c) The real and imaginary parts of S_{21} plotted in the complex plane.

[26]

$$\tan\theta \approx \theta = \frac{\mathrm{Im}[S_{21}]}{\mathrm{Re}[S_{21}]} \approx -4Q_l\delta' \equiv -4Q_l\frac{\delta\omega}{\omega_0} \tag{2.59}$$

$$\delta A \approx 1 - A \approx -2Q_l\delta\left(\frac{1}{Q}\right) \tag{2.60}$$

where we have redefined $\omega_0 = \omega_0'$. For the remainder of this thesis, $\omega_0 = 2\pi f_0$ refers to the resonant frequency of the quarter wave resonator, including the added inductance of the Al sensor strip. The pair-breaking detector can be readout out by monitoring changes in the on resonance amplitude or phase. Having derived the change in the amplitude and phase due to a change in the quasiparticle distribution from a simple circuit model and the Mattis Bardeen expressions we have a complete model describing the operation of our detector. In the following chapters we will use this model to understand the response of our detector to a thermal quasiparticle distribution (Chapter 4) and to radiation emitted by a blackbody (Chapter 5).

2.4 Antenna physics

We showed in the previous sections that our pair-breaking detector will exhibit a response in both the resonator amplitude and phase due to a change in the quasiparticle distribution

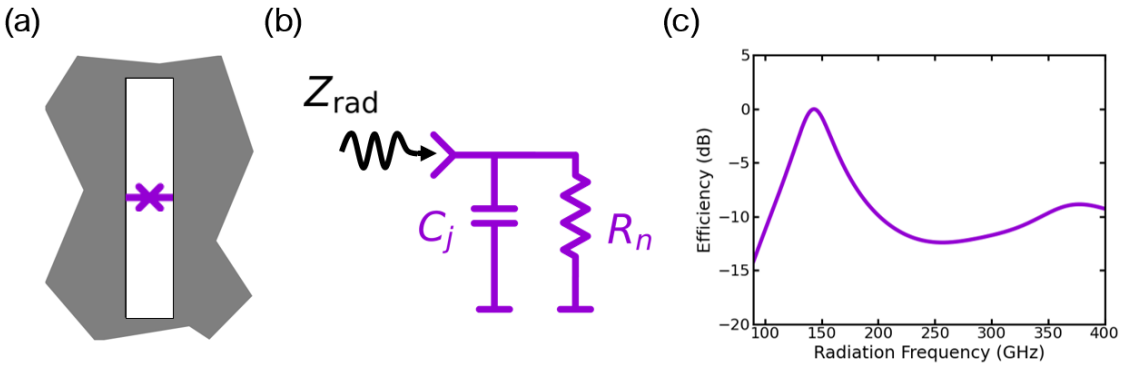

Figure 2.7: Josephson-assisted slot antenna. (a) The slot antenna, a large rectangular cavity in a conducting sheet, is driven by a Josephson junction located at the center of the slot. (b) Circuit representation of the Josephson junction, accurate for radiation frequencies above the Al gap ($f_{\rm rad} > 92$ GHz). (c) Efficiency, calculated from Eq. 2.63, with the radiation impedance simulated in CST Microwave Studio [29].

of the high kinetic inductance sensor strip. There are a number of different quasiparticle generation mechanisms, however in radio astronomy, the generation mechanism of interest is absorption of a pair breaking photon. This is when a photon, with energy greater than twice the superconducting gap of the sensor strip is absorbed, providing sufficient energy to break a Cooper pair, generating two quasiparticles. First proposed in 2006, coupling to pair-breaking radiation can by improved by integrating an antenna into the pair breaking detector [27]. More recently, noise equivalent powers as low as 3×10^{-20} W/$\sqrt{\rm Hz}$ have been demonstrated with antenna-coupled kinetic inductance detectors, designed to absorb radiation with a frequency around 850 GHz [28]. In this Section, we discuss how a Josephson junction may be used to improve coupling to incident radiation in an antenna-coupled kinetic inductance detector.

As demonstrated in [30, 31], typical superconducting qubit structures are antennas, which resonate at mm-wave frequencies. Further, the authors show that the Josephson junction, for parameters typical of superconducting qubit devices, provides a reasonable conjugate match to the radiation impedance, $Z_{\rm rad}$, which satisfies the condition for maximal power absorption [30]

$$\Gamma = \frac{Z_{\rm rad} - Z_J^*}{Z_{\rm rad} + Z_J^*} \tag{2.61}$$

where Z_J is the impedance of the Josephson junction. Since we are interested in coupling to pair-breaking radiation, $f_{\rm rad} > 2\Delta/h = 91.8$ GHz for Al, we can accurately model the Josephson junction as a capacitor, C_J in parallel with a resistor, R_n (Fig. 2.7 (b)). C_J is the capacitance of the Josephson junction, set by the area of the junction and the thickness of the oxide barrier[5]. R_n is the normal state resistance of the junction. The junction impedance is then

$$Z_J = \left(\frac{1}{R_n} + j\omega C_J\right)^{-1}. \tag{2.62}$$

The efficiency[6] with which the antenna couples to radiation is then defined as

$$\eta_{\rm opt} = 1 - |\Gamma|^2. \tag{2.63}$$

So, by simply tuning the junction's normal state resistance and capacitance, determined in fabrication, one can match the junction impedance to the conjugate radiation impedance. While resonant absorption of pair-breaking radiation [31] is detrimental to superconducting qubits, the question that prompts the work in the remainder of the first part of this thesis is: can we leverage the resonant absorption of pair-breaking radiation at a Josephson junction to develop a new type of quantum sensor?

For this project, we chose to work with a slot antenna (Fig. 2.7 (a)), a long narrow cavity carved out of a conducting sheet, which will resonantly absorb radiation with wavelengths corresponding to the length of the slot. The addition of the Josephson junction, in the center of the slot, provides a mechanism via which to drive the antenna. Simulating the radiation impedance in CST Microwave Studio [29], we can calculate from Eq. 2.63 the expected efficiency for typical junction parameters, shown in Fig. 2.7 (c). On resonance, the expected efficiency is near unity. In the Chapter 3 we describe design and fabrication of the detector, as well as the cryogenic measurement apparatus and room temperature electronics. In Chapter 4 we look at detector response to a thermal quasiparticle distribu-

[5] Al-AlOx-Al junctions, for the parameters typically used in superconducting qubits have capacitance per unit area $50 - 100$ fF/μm^2 [32].

[6] Sometimes referred to as coupling efficiency or optical efficiency within this thesis

tion, before looking at response to radiation emitted by a blackbody source in Chapter 5. Finally, we look at the spectral response due to radiation emitted by a Josephson emitter in Chapter 6.

Chapter 3

Experimental methods

We begin this chapter by discussing the layout and design of the Josephson mm-wave detector, before going through the fabrication details of such a device. We then move on to discuss the cryogenic measurement apparatus as well as the room temperature electronics used for measurement. Finally, we conclude with a note discussing measures taken to eradicate ground loops, specifically for the measurements of the detector noise.

3.1 Layout and fabrication

The detector consists of a quarter-wave coplanar waveguide resonator capacitively coupled to a transmission line. These devices have a hybrid design: the ground plane, the center conductor of the resonator, and transmission line are all made of Nb, while the majority of the kinetic inductance is due to two Al nanowires[1]. The Al volume is located at the shorted end of the CPW resonator, where the current is the largest, in order to maximize the response due to a change in the kinetic inductance.

The slot antenna, designed to improve coupling to pair-breaking radiation, is embedded at the current anti-node (shown in Fig. 3.1). Half of the slot antenna exists in the space between the two Al nanowires, the other half is carved out of the ground plane. A Josephson junction, located in the center of the slot antenna, is used to match the

[1]sometimes referred to as the sensor strip, the high kinetic inductance volume, or the Al volume

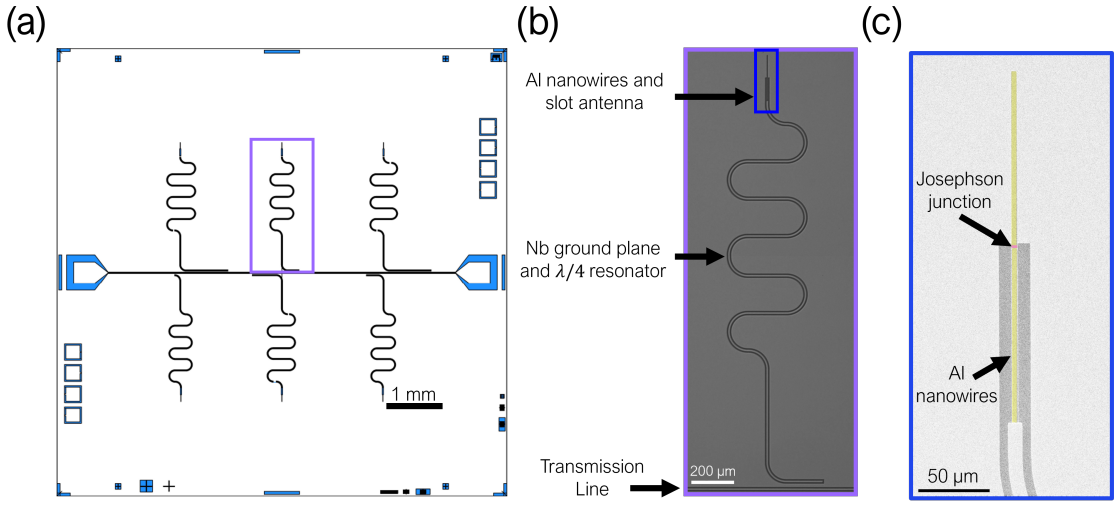

Figure 3.1: Sample layout. (a) Screen capture of the device GDS, showing six resonators capacitively coupled to the central feedline. White indicates areas where the superconducting film, in this case Nb, remains. Blue indicates areas where the superconductor was etched away, exposing the silicon substrate. (b) Optical image of a single resonator. (c) Scanning electron micrograph showing the Al sensor strip and slot antenna (false-color yellow) at the current anti-node of the CPW resonator. The Josephson junction, located at the center of the slot antenna, is shown, false-color, in magenta.

conjugate radiation impedance (the condition for maximal power absorption), allowing for the resonant transduction of photons to quasiparticles. Quasiparticles generated by the absorption of pair-breaking radiation at the Josephson junction will be confined to the Al sensor strip due to gap engineering. A lower gap material, in this case Al, is chosen to create a quasiparticle moat. Quasiparticles at the Josephson junction will quickly scatter down to the Al gap edge where they will have insufficient energy to diffuse into the higher gap Nb ground plane and center trace.

Each sample consisted of six $\lambda/4$ coplanar waveguide resonators capacitively coupled to a central feedline (Fig. 3.1). Resonators had a central conductor width, $w_r = 10\,\mu$m and gap width $g_r = 6\,\mu$m, and were designed to have a $50\,\Omega$ impedance and to resonate between 4 - 6 GHz. Samples were fabricated on 3 inch prime-grade intrinsic FZ Si (100) wafers with resistivity greater than 10 kΩ-cm. A 40 nm thick Nb base layer was deposited via magnetron sputtering immediately following exposure to dilute (2%) hydrofluoric acid for 1 minute to remove the native silicon oxide.

Features with critical size greater than 2 μm, which includes the coplanar waveguide resonators, transmission line, bond pads, test structures and portions of the slot antenna, were patterned via optical lithography using a Heidelberg DWL 66+ direct-write laser lithography tool. Prior to exposure with the direct-write lithography system, samples were spin-coated with AZ MiR 703 photoresist. Post-exposure, samples were developed in MF CD-26 for 1 minute then immediately quenched in deionized water for 1 minute and blow-dried with N_2.

To transfer the pattern from the photoresist mask to the sample, samples were then dry-etched using a Plasma-Therm 770 inductively-coupled plasma (ICP) reactive-ion etcher (RIE). The etch chemistry was chlorine-based, consisting of the following gases (flow rates): BCl_3 (18 sccm), Cl_2 (9 sccm) and Ar (18 sccm) with a total pressure of 40 mTorr. An ICP power of 300 W and a RIE power of 50 W were used. An etch rate of 50 nm per minute for Nb was determined by par-etching a 90 nm Nb film, then profiling the step height using a KLA-Tencor P7 profilometer. Subsequent to etch calibration, samples were etched for 2 minutes and 15 seconds. Immediately prior to etching, the etch chamber was conditioned by performing a 5 minute O_2-based clean, followed by a 5 minute pre-seed utilizing the same etch chemistry as the Nb etch. Post-etch, AZ MiR 703 photoresist was removed from the sample via a solvent-clean consisting of submersion in Microposit Remover 1165 (NMP) at 80 C for 15 min, followed by sonication in Microposit Remover 1165 for 3 min, sonication in IPA for 3 min, and sonication in deionized water for 3 min. Finally, samples were blow-dried with N_2.

Fabrication of the high-kinetic inductance Al nanowire and Josephson junction required patterning via electron-beam lithography (EBL). A resist bilayer consisting of MMA (8.5) EL 11 (with an approximate thickness of 680 nm) underneath 950 PMMA A3 (approximate thickness of 170 nm) was exposed using an Elionix ELS-G100 100 keV EBL system. Post-exposure, samples were developed in a mixture of DI:IPA (100 mL:300 mL) maintained at a temperature of 2 C using an ice bath. Samples were immediately dried with N_2 following development.

The high-kinetic inductance nanowires, 100 nm wide and 125 μm long, and the Josephson junctions were deposited in the same step via double-angle evaporation in an electron-beam evaporator. Prior to deposition but subsequent to loading in the vacuum chamber, samples were subject to 12 seconds of ion milling to remove any native oxide on the Nb base layers, allowing for galvanic contact between the to-be deposited Al layer and the existing Nb film. The bottom electrode of the Josephson junction was formed by a 29.0 nm-thick Al film deposited at an angle of -35° with an approximate deposition rate of 2 Å per second. This was followed by an *in situ* oxidation at 130 mT for 2 minutes to form the insulating barrier. Finally, the top-electrode of the Josephson junction was formed by a 41.9 nm Al film deposited normal to the surface of the sample, again with an approximate deposition rate of 2 Å per second. Subsequent to evaporation the films were lifted off in Microposit Remover 1165 at 80 C. Once the metal film had cleared the sample surface, samples were transferred to a clean volume of Microposit Remover 1165 and sonicated for 3 minutes, before sonication in IPA for 3 minutes. Finally, samples were blow-dried with N_2.

Prior to being cooled for characterization, samples were diced using a Disco DAD3221 automatic dicing saw. Samples were encapsulated in a protective coating of SPR 955 photoresist prior to dicing. This coating was removed after dicing by rinsing with acetone followed by IPA and dried using a nitrogen gun. Dies were packaged in an Al or Au-coated Cu sample enclosure. Al wirebonds placed using a West Bond 7476E-79 Al wedge wire bonder were used to make contact between the on-chip bond pads and the copper traces of the Al sample enclosure.

3.2 Cryogenic measurement

Samples were mounted to the mixing chamber plate of a Leiden cryogen-free dilution refrigerator and cooled to a temperature of approximately 18 mK. Samples discussed in this thesis were either mounted in a Al sample enclosure, inside a light-tight Cryoperm[2] can,

[2]Sometimes referred to as mu-metal

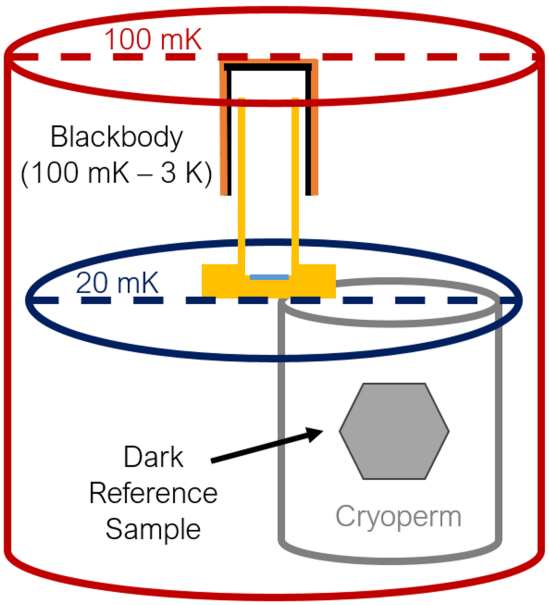

Figure 3.2: Cartoon of the cryostat showing the locations of the sample subject to illumination by the blackbody and the dark reference sample.

or in the case of the blackbody experiment, they were mounted in a Au-coated Cu sample box thermalized to the top of the mixing plate, directly underneath the blackbody emitter. To absorb stray photons from higher temperature stages, the exchange plate shield was coated with Stycast 1266 (parts A and B), mixed with silica powder and carbon black. Silicon carbide crystals were used to make the interior surface of the can non-uniform. A second coat of the Stycast mixture was then applied to hold the silicon carbide crystals in place. This is the same mixture used to coat the inside of the light-tight μ-metal can. The mu-metal can is designed to have a light-tight lid. SubMiniature A (SMA) bulkhead feedthroughs are used to transfer signals into the light-tight can. Indium is used on each of the mating surfaces to minimize light leakage around the SMAs. Inside the can, EZ form, hand-formable non-magnetic SMA cables are used to transfer measurement signals to the sample box.

Two room temperature electronics setups were used for data acquisition. The response of the resonator, from which we extracted Q_i and f_0, was measured in transmission using an Agilent N5230A vector network analyzer (VNA). Noise measurements were done

via heterodyne detection. The measurement signal was generated using single-sideband mixing (Fig. 3.3 (a)). Arbitrary waveform generation and demodulation were done using a Quantum Machines[3] OPX+. For measurement tones synthesized using sideband mixing, base-band pulses generated from the AWG were mixed with a microwave carrier frequency[4] to produce a tone at the resonator frequency[5]. Upon returning from the cryostat the signal was mixed back to base-band using a copy of the LO. Further demodulation was done in software.

In either case the measurement chain was the same after pulse synthesis (Fig. 3.3 (b)). The measurement tone first passed through variable room temperature attenuation, 20 dB of attenuation at the 3 K stage, then 40 dB of attenuation at the 20 mK stage of the cryostat. Low-pass filters and high-frequency eccosorb filters were used at the device to reduce light leakage from higher temperature stages. At the output side of the device the signal passes through three cryogenic isolators before leaving the millikelvin stage. A high-electron mobility transistor (HEMT) at 3 K amplified the signal prior to leaving the fridge. Additional amplification was used at room temperature before the signal either returned to the VNA or was demodulated to base-band in the case of the heterodyne setup. Radiall microwave switches, modified for use in a cryogenic environment, were used to increase measurement throughput.

To be discussed in the following Chapters, measurements of the amplitude and phase noise of the detector as a function of either ambient temperature or incident radiation from a blackbody emitter were used to probe the detector response. Measurement of these quantities required reduction spurious noise sources (for instance, 60 Hz noise), primarily achieved through the elimination of ground loops in the experimental setup. Outer DC blocks were used on all lines connecting the cryostat to the fast-electronics rack. An isolation transformer was used to break the ground connection between the quantum machines OPX+ and the power strip in the rack. Care was taken to eliminate all other ground connections from the top of the fridge. Conductive KF clamps and o-rings,

[3]Sometimes called the AWG (arbitrary waveform generator)
[4]Also referred to as the local oscillator or LO
[5]A mathematical description of digital mixing is given in Appendix A.3.

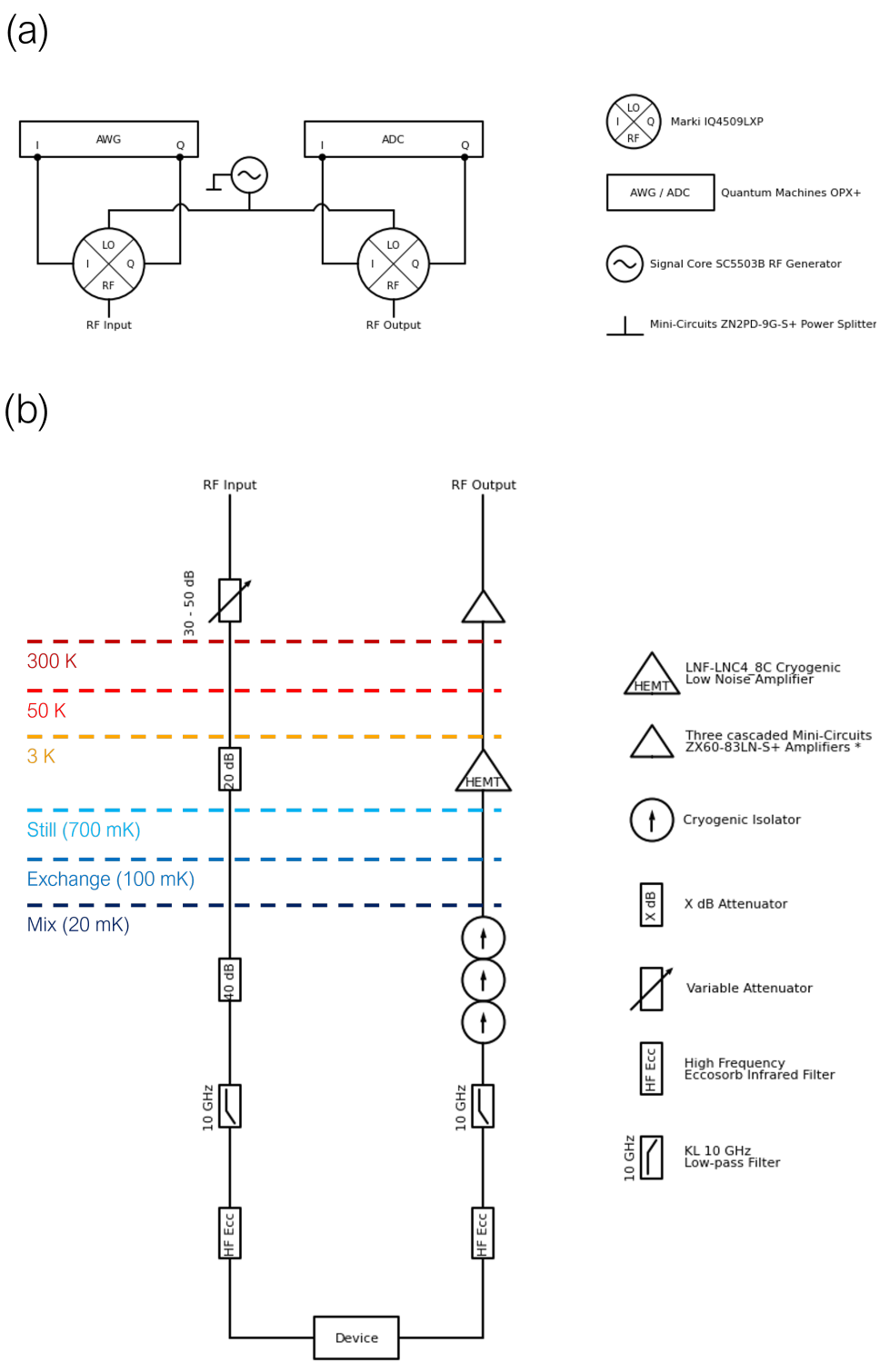

Figure 3.3: Experimental measurement setup. Circuit symbols are defined on the right. (a) Heterodyne setup. (b) Wiring diagram. Colored dashed lines indicate to which temperature stage components are thermalized.

connecting the top of the cryostat to the gas handling unit were replaced with insulating ones. Cabling connecting the in-built heaters and fridge thermometry resulted in an ohmic connection between the cryostat and the gas handling system, resulting in myriad ground loops. Thus, after setting up each scan, the fridge thermometry was disconnected from the cryostat for the duration of the scan. Further, a 'battery box', consisting of a 9 V battery, a voltage regulator, and a potentiometer were used to provide current to the blackbody heater, further eliminating an ohmic connection to the gas handling unit.

Described in the following chapters, data taken with this apparatus and measurement scheme was used to measure the noise equivalent power of the detector, from which the detector efficiency is estimated.

Chapter 4

Response to a thermal quasiparticle distribution

We've discussed the operating principle of our detector, design considerations, and the experimental apparatus. What remains is to demonstrate that we understand the response of the detector and to quantify the detector performance. We begin by looking at the detector response to a thermal quasiparticle population. In this case, there are essentially no free parameters. As such, we can use this as an opportunity to measure the kinetic inductance fraction. In this Chapter, we use the Mattis Bardeen integrals for a thermal distribution to calculate the expected detector response using Eq. 2.22 and Eq. 2.35. We then compare these expressions to the measured $\delta(1/Q)$ and $\delta f/f_0$ of our device for bath temperatures ranging from 18 mK to 300 mK. From the measured quality factor and resonant frequency as a function of temperature, we extract the quasiparticle density and compare with the analytical expression. We measure the spectrum of quasiparticle number fluctuations as an independent measurement of the number of quasiparticles.

4.1 A thermal quasiparticle distribution

As shown in Chapter 2, the detector response to a change in the quasiparticle distribution is described by a change in the complex conductivity, the real and imaginary parts of

which are given by the Mattis Bardeen integrals (Eq. 2.9 and Eq. 2.10). With these analytical expressions in hand, we can measure the internal quality factor and resonant frequency as we vary the temperature and compare the results of evaluating Eq. 2.22 and Eq. 2.35 using Eq. 2.9 and Eq. 2.10.

4.1.1 The spectrum of quasiparticle number fluctuations

The number of quasiparticles in a superconductor at thermal equilibrium will fluctuate about the mean value, N_{qp}. This generation-recombination noise is a limiting source of noise for the pair-breaking detector [10, 11]. Wilson and Prober developed a model describing the dynamics of these quasiparticle fluctuations, using a master equation approach [16], and in doing so derived expressions for the autocorrelation function and the variance of these fluctuations. With these results we can compute the power spectral density of quasiparticle number fluctuations using the Wiener-Khinchin theorem [10, 33]. The Wiener-Khinchin theorem relates the autocorrelation to the power spectral density via the Fourier transform:

$$S_x(\omega) = 2\int_{-\infty}^{\infty} r_{xx}(t)e^{-i\omega t}dt \tag{4.1}$$

where $r_{xx}(t)$ is the autocorrelation function and $S_x(\omega)$ is the power spectral density ($\omega = 2\pi f$). Using the result from Wilson and Prober,

$$r_{xx}(t) = \sigma^2 e^{-|t|/\tau_{qp}} \tag{4.2}$$

where τ_{qp} is the limiting timescale, in this case the quasiparticle recombination time and $\sigma^2 = N_{qp}$ is the variance [16].

$$\begin{aligned} S_N(\omega) &= 2N_{qp}\int_{-\infty}^{\infty} e^{-|t|/\tau_{qp}} e^{-i\omega t} dt \\ &= 2N_{qp}\left[\int_{-\infty}^{0} e^{t(1/\tau_{qp}-i\omega)} dt + \int_{0}^{\infty} e^{-t(1/\tau_{qp}+i\omega)} dt\right] \\ &= 2N_{qp}\left[\frac{1}{1/\tau_{qp}-i\omega} e^{1/\tau_{qp}-i\omega}\Big|_{-\infty}^{0} + \frac{1}{1/\tau_{qp}+i\omega} e^{1/\tau_{qp}+i\omega}\Big|_{0}^{\infty}\right] \\ &= 2N_{qp}\left[\frac{1}{1/\tau_{qp}-i\omega} + \frac{1}{1/\tau_{qp}+i\omega}\right] \\ &= \frac{4N_{qp}\tau_{qp}}{1+(\omega\tau_{qp})^2} \end{aligned} \tag{4.3}$$

$$S_N(f) = \frac{N_{qp}\tau_{qp}}{1+(2\pi f\tau_{qp})^2}. \tag{4.4}$$

Looking at Eq. 4.4 we can see that the power spectral density will have a Lorentzian lineshape with the knee frequency set by the quasiparticle lifetime. The spectrum of quasiparticle number fluctuations can be related to the experimental observables, amplitude and phase in the following way [34]:

$$S_A(f) = \frac{S_N(f)}{1+(2\pi f\tau_r)^2}\left(\frac{dA}{dN_{qp}}\right)^2 \tag{4.5}$$

$$S_\theta(f) = \frac{S_N(f)}{1+(2\pi f\tau_r)^2}\left(\frac{d\theta}{dN_{qp}}\right)^2. \tag{4.6}$$

Also of interest is the cross-spectral density, $S_{\theta,A}(f)$, which can similarly be related to $S_N(f)$:

$$S_{\theta,A}(f) = \frac{S_N(f)}{1+(2\pi f\tau_r)^2}\left(\frac{d\theta}{dN_{qp}}\frac{dA}{dN_{qp}}\right). \tag{4.7}$$

The cross-spectrum looks at correlations between two signals, effectively averaging away uncorrelated noise in the signal, for instance due to the measurement apparatus. As result the signal may be clearer in the cross-spectrum than in the amplitude or phase spectrum alone. Because of this, we fit to the cross-spectrum to extract the quasiparticle lifetime. Later in this Chapter we will use Eq. 4.5 - 4.7 to extract the quasiparticle lifetime and

number of quasiparticles for a thermal quasiparticle distribution.

4.2 Detector response to elevated temperature

To look at the response of our detector to a thermal quasiparticle distribution we heat the cryostat stage to which our sample is mounted. The data shown in this Chapter is for a nominally dark sample mounted inside a light tight Cryoperm canister, thermalized to the mixing chamber plate of a Leiden cryogen-free dilution refrigerator. During normal operation this stage sits at a base temperature of about 18 mK, but can be heated to more than 300 mK while continuing to circulate the He3/He4 mixture. Transmission across the resonator is measured with a vector network analyzer. The wiring diagram is equivalent to that shown in Fig. 3.3. Monitoring the internal quality factor of the resonator as a function of microwave readout power, we see that the quality factor saturates at low and high powers, characteristic of a device limited by two level system (TLS) losses [35]. At very high readout powers, we start to see bifurcation due to the nonlinear inductance of the nanowire. As such, we use highest readout power prior to bifurcation.

Fitting a circle to real and imaginary parts of S_{21} in the complex plane we extract the coupling quality factor, the internal quality factor, and the resonant frequency [24, 36]. The data and resulting fits are shown in Fig. 4.1. Fig. 4.2 shows Q_i, $\delta f/f_0$, and $\delta(1/Q_i)$ extracted from fits. The dotted black line in Fig. 4.2 (a) is the predicted value for Q_i, given by Eq. 2.20, evaluated using Eq. 2.9 and Eq. 2.10. We see that the data agrees with the Mattis Bardeen prediction for high temperatures, but saturates at low temperature. In actuality, there are numerous loss channels that may limit the measured internal quality factor, including TLS losses and radiation from higher temperature stages. These quality factors add in parallel

$$\frac{1}{Q_{i,\mathrm{meas}}} = \frac{1}{Q_i} + \frac{1}{Q_{\mathrm{TLS}}} + \frac{1}{Q_{\mathrm{rad}}} + ... \tag{4.8}$$

Hence, the quality factor, at which our measured Q saturates, will be the parallel combi-

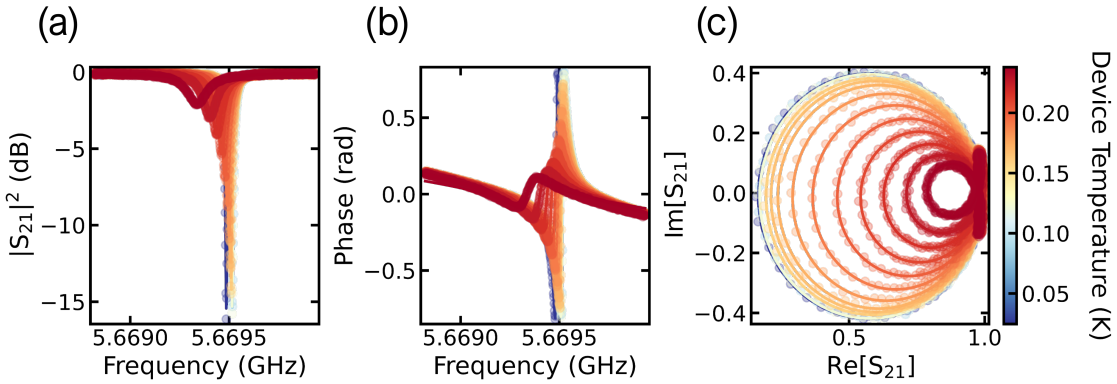

Figure 4.1: Detector response to elevated bath temperatures. Data, taken with a vector network analyzer, is shown along with the fits from which Q_i and f_0 are extracted. The density of data points is reduced to show the quality of the fit. (a) Amplitude response to elevated temperature. The change in frequency is evident as a shift down in the Lorentzian dip. The decrease in the depth of the Lorentzian indicates a decrease in the internal quality factor. (b) Phase, the angle between the real and imaginary parts of S_{21}. (c) The real and imaginary parts of S_{21} plotted in the complex plane. The decrease in the internal quality factor with elevated temperature is apparent as a reduction in the diameter of the circle in the complex plane.

nation of these additional loss channels

$$\frac{1}{Q_{i,\mathrm{sat}}} = \frac{1}{Q_{\mathrm{TLS}}} + \frac{1}{Q_{\mathrm{rad}}} + \ldots \tag{4.9}$$

Our measured internal quality factor will then be the sum of $Q_{i,\mathrm{sat}}$ and the Q_i derived from the Mattis Bardeen expressions [10]

$$\frac{1}{Q_{i,\mathrm{meas}}} = \frac{1}{Q_i} + \frac{1}{Q_{i,\mathrm{sat}}}. \tag{4.10}$$

Adding the maximum measured internal quality factor, $Q_{i,\mathrm{max}}$ in parallel with the expected quasiparticle-limited Q_i we achieve good agreement with the data. We similarly compute the expected change in loss (Eq. 2.22) and the fractional frequency shift (Eq. 2.35), Fig. 4.2 (b) and (c), finding reasonable agreement with measured data.

Noting the dependence on $e^{-\Delta/k_BT}$ we can relate Eq. 2.20 to the reduced quasiparticle

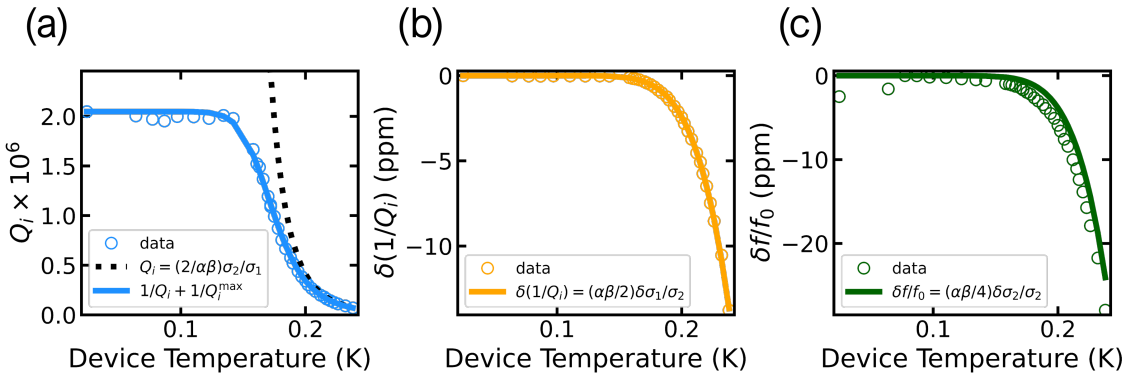

Figure 4.2: Change in the internal quality factor and fractional frequency shift extracted from fits as a function of temperature. (a) Internal quality factor as a function of temperature. The black dotted line shows the expected value from the circuit model of the detector (Eq. 2.20). The blue solid line is the result of adding the maximum internal quality factor in parallel. The data diverges from the Mattis Bardeen prediction as other loss channels begin to dominate at lower temperatures. (b) Measured change in the resonator loss. The solid yellow line shows the predicted value (Eq. 2.22) (c) Measured fractional frequency shift. The solid green line is the predicted response to elevated temperature (Eq. 2.35).

density, $x_{qp} = n_{qp}/n_{cp} \propto e^{-\Delta/k_BT}$. Following the notation of [9] we define $\xi = hf/2k_BT$.

$$\begin{aligned} Q_i &= \frac{2}{\alpha\beta}\frac{\sigma_2}{\sigma_1} \\ &= \frac{2}{\alpha\beta}\frac{\sigma_2(T)/\sigma_n}{\sigma_1(T)/\sigma_n} \\ &= \frac{2}{\alpha\beta}\frac{\frac{\pi\Delta}{hf}\left(1-\sqrt{\frac{2\pi k_BT}{\Delta}}e^{-\Delta/k_BT-2e^{-\Delta/k_BT}e^{-\xi}I_0(\xi)}\right)}{\frac{4\Delta}{hf}e^{-\Delta/k_BT}\sinh(\xi)K_0(\xi)}. \end{aligned} \tag{4.11}$$

Solving for $x = e^{-\Delta/k_BT}$,

$$Q\frac{2\alpha\beta}{\pi}(x\sinh(\xi)K_0(\xi)) = 1 - \sqrt{\frac{2\pi k_BT}{\Delta}}x - 2xe^{-\xi}I_0(\xi)$$

$$x = \left[\frac{2\alpha\beta}{\pi}Q_i\sinh(\xi)K_0(\xi) + \sqrt{\frac{2\pi k_BT}{\Delta}} + 2e^{-\xi}I_o(\xi)\right]^{-1}$$

$$x_{qp}(Q_i,T) = \frac{2N_0}{n_{cp}}\sqrt{2\pi k_BT\Delta}\left[\frac{2\alpha\beta}{\pi}Q_i\sinh(\xi)K_0(\xi) + \sqrt{\frac{2\pi k_BT}{\Delta}} + 2e^{-\xi}I_o(\xi)\right]^{-1}. \tag{4.12}$$

Recall that $N_0 = 1.72 \times 10^{10}$ eV^{-1} μm^{-3} is the single spin density of states at the Fermi

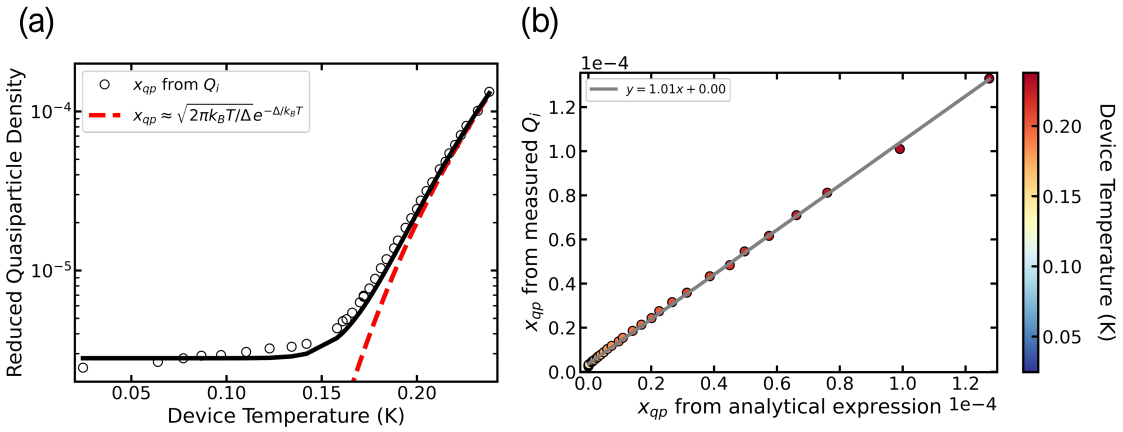

Figure 4.3: Reduced quasiparticle density, x_{qp}, extracted from the internal quality factor. (a) x_{qp} extracted from the internal quality factor as a function of device temperature. The red dashed line is the value expected from theory. We find reasonable agreement for higher temperatures. For lower temperatures, the reduced quasiparticle density saturates, a result of the saturation in Q_i observed in Fig. 4.2 (a). If we account for this saturation (the black trace), we find reasonable agreement for all temperatures.(b) x_{qp} extracted from Q_i plotted versus the expected value (Eq. 2.3).

level [18] and $n_{cp} = 4 \times 10^6\ \mu\text{m}^{-3}$ is the density of Cooper pairs [37]. The values of N_0 and n_{cp} given here are for aluminum. Assuming that we trust the fridge thermometry, this allows us to estimate the reduced quasiparticle density from the measured internal quality factor (shown in Fig. 4.3). We can independently measure the spectrum of quasiparticle fluctuations, from which we can extract the quasiparticle number, N_{qp}.

4.2.1 Amplitude and phase responsivity

The amplitude responsivity, dA/dN_{qp}, and phase responsivity, $d\theta/dN_{qp}$ describe the change in the amplitude or phase signal due to a change in the number of quasiparticles. Starting from Eq. 2.59 and Eq. 2.60 we have

$$\frac{dA}{dN_{qp}} = -2Q_l \frac{d(1/Q_i)}{dN_{qp}} \tag{4.13}$$

$$\frac{d\theta}{dN_{qp}} = -4Q_l \frac{df/f_0}{dN_{qp}} \tag{4.14}$$

Using Eq. 2.22 and Eq. 2.35 along with $N_{qp} = n_{qp}V$ and recalling that we had previously made the approximation $|\sigma| \approx \sigma_2$

$$\frac{dA}{dN_{qp}} = -2Q_l \frac{d(1/Q_i)}{dN_{qp}} = -2Q_l \frac{\alpha\beta}{2} \frac{d\sigma_1/\sigma_2}{dN_{qp}} = -\frac{\alpha\beta Q_l}{|\sigma|V} \frac{d\sigma_1}{dn_{qp}} \tag{4.15}$$

$$\frac{d\theta}{dN_{qp}} = -4Q_l \frac{\alpha\beta}{4} \frac{d\sigma_2/\sigma_2}{dN_{qp}} = -\frac{\alpha\beta Q_l}{|\sigma|V} \frac{d\sigma_2}{dn_{qp}} \tag{4.16}$$

we relate the amplitude and phase responsivity to the complex conductivity. These derivatives can be evaluated for a thermal quasiparticle distribution [9]

$$\frac{1}{\sigma_n} \frac{d\sigma_1}{dn_{qp}} = \frac{1}{N_0 hf} \sqrt{\frac{2\Delta}{\pi k_B T}} \sinh\left(\frac{hf}{2k_B T}\right) K_0\left(\frac{hf}{2k_B T}\right) \tag{4.17}$$

$$\frac{1}{\sigma_n} \frac{d\sigma_2}{dn_{qp}} = -\frac{\pi}{2N_0 hf}\left(1 + \sqrt{\frac{2\Delta}{\pi k_B T}} e^{-hf/2k_B T} I_0\left(\frac{hf}{2k_B T}\right)\right) \tag{4.18}$$

allowing us to evaluate Eq. 4.15 and Eq. 4.16. Converting the measured temperature to number of quasiparticles using Eq. 2.2 and plotting our measured $\delta(1/Q_i)$ and $\delta f/f_0$, we see that the data falls onto a line. Using the slope extracted from a linear fit along with Eq. 4.13 and Eq. 4.14 we compute the amplitude and phase responsivity (Fig. 4.4) [10]. The amplitude and phase responsivity will allow us to convert the measured amplitude and phase noise spectra to the spectrum of quasiparticle number fluctuations in the next section.

4.3 Measurement of detector noise under dark conditions

4.3.1 Measurement of the quasiparticle lifetime and density

To measure the spectrum of quasiparticle number fluctuations we first require either the amplitude power spectral density (PSD), the phase power spectral density, or the cross-spectral density (CSD). These can be computed from a time series of amplitude and phase fluctuations via the Fourier transform. Time series data was acquired using the heterodyne setup described in Chapter 3. For each temperature, a frequency sweep of

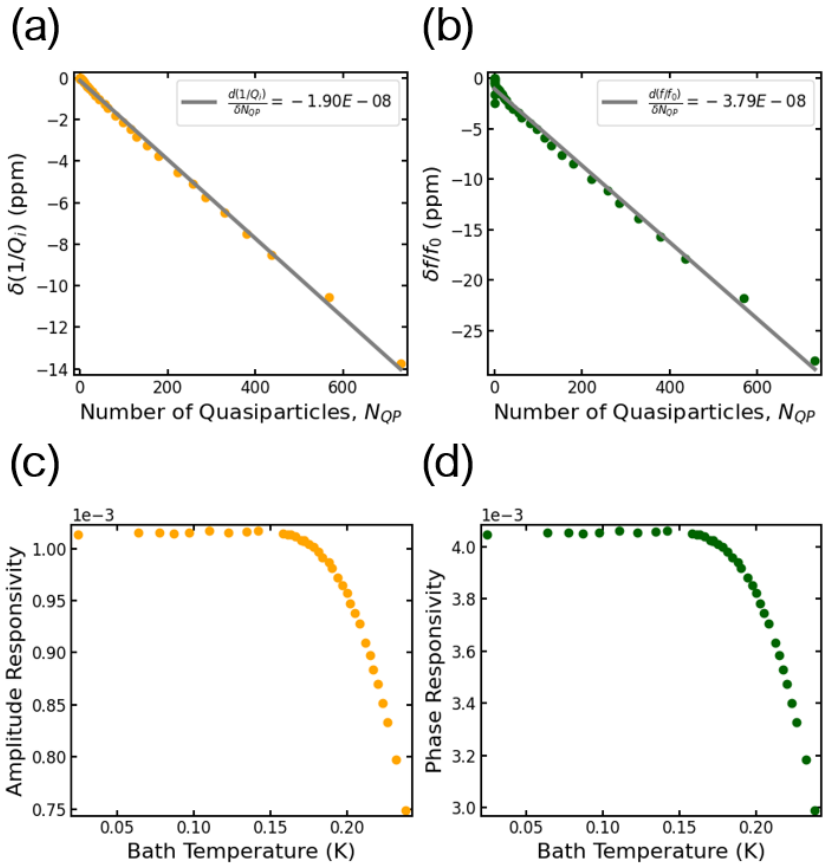

Figure 4.4: Amplitude and phase responsivity. (a) The change in resonator loss, $\delta(1/Q_i)$, as a function of the number of quasiparticles, N_{qp}. The linear fit gives the change in loss due to a change in the number of quasiparticles, from which the amplitude responsivity can be computed. (b) The change in the fractional frequency shift as a function of the number of quasiparticles. The phase responsivity can be calculated from the slope of the linear fit. (c) The amplitude responsivity computed using Eq. 4.13. (d) The phase responsivity computed using Eq. 4.14.

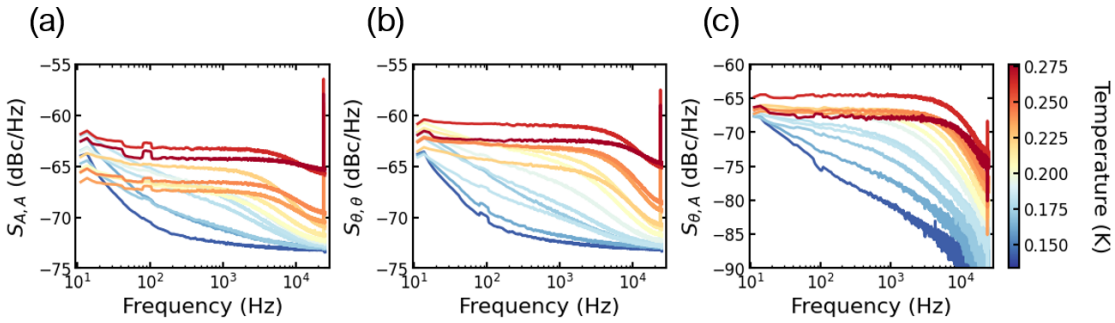

Figure 4.5: Power spectral densities for varying device temperature (indicated by the line color, referenced to the colorbar). (a) Amplitude power spectral density. (b) Phase power spectral density. (c) Amplitude-phase cross spectral density.

the resonance was performed, in order to extract the temperature-dependent resonant frequency. The amplitude of the measurement signal was chosen to match the readout power used when acquiring the vector network analyzer data in Section 4.2. Then the timeseries was acquired by repeatedly reading out on resonance, integrating the signal for 10 μs, with no delay between measurement. Off-resonant measurements (also 10 μs) were interleaved with the on-resonant measurements. This was repeated 10,000 times to form a single 0.2 s time series. This was repeated to acquire 1,000 time series. The amplitude PSD, phase PSD, and CSD were computed separately for each of the 1,000 time series. The resulting 1,000 amplitude PSDs were then averaged together. The same was done for the phase PSD and CSD. Finally, a boxcar average was applied to the data [38]. The resulting amplitude PSD, phase PSD and CSD are shown in Fig. 4.5.

At high temperatures, a clear Lorentzian line-shape is present, with the knee frequency moving to higher frequencies as temperature increases, which is what we expect for a spectrum where the dominant timescale is the quasiparticle lifetime. The low temperature spectra show a $1/f$-like dependence at low frequencies. We convert the amplitude and phase PSDs and the cross spectrum to the spectrum of quasiparticle number fluctuations using Eq. 4.5 - Eq. 4.7 along with the amplitude and phase responsivities measured in Section 4.2 and the resonator ring time, $\tau_r = Q_l/\pi f_0$, computed from the data in Section 4.2 (Fig. 4.6).

Recall from Chapter 2, Eq. 2.5, that we expect the product of the quasiparticle lifetime

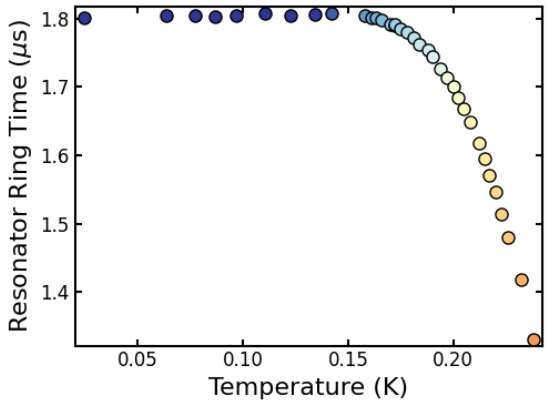

Figure 4.6: Resonator ring down time.

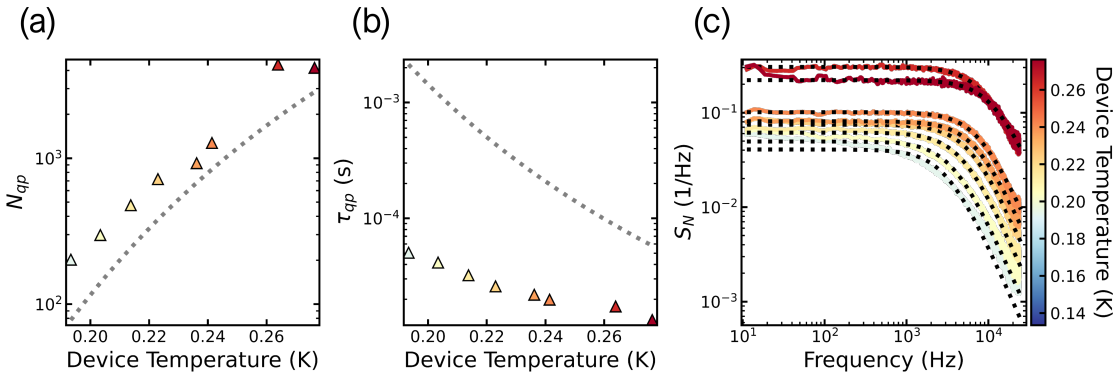

Figure 4.7: Spectrum of quasiparticle fluctuations, calculated from the cross-spectral density using Eq. 4.7. (a) The number of quasiparticles, N_{qp} derived from the amplitude of a Lorentzian fit to the spectrum of quasiparticle fluctuations, $S_N(f)$. The grey dashed line is the analytical expression, Eq. 2.2. (b) The quasiparticle lifetime extracted from a fit to $S_N(f)$. The grey dashed line is the analytical expression given by Eq. 2.4. We find a significantly lower quasiparticle lifetime than expected, due to trapping. (c) The spectrum of quasiparticle number fluctuations, derived from the cross spectral density from Eq. 4.7, for various device temperatures. While data was taken for lower temperatures, significant $1/f$ noise at lower temperatures made it difficult to reliably fit to a Lorentzian. As a result, lower temperatures are excluded here.

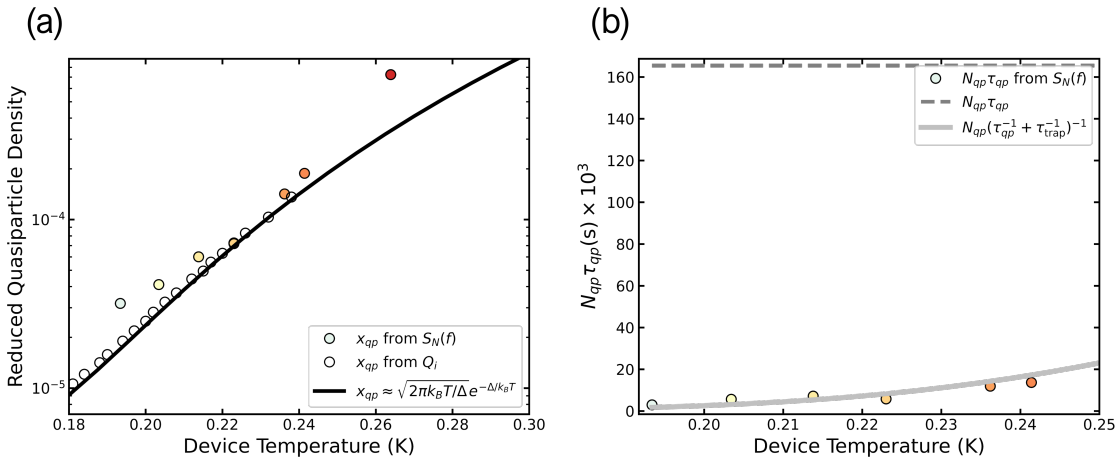

Figure 4.8: (a) Reduced quasiparticle density, x_{qp} as a function of device temperature. The open circles are x_{qp} extracted from fits to the internal quality factor (see Fig. 4.3). The colored circles are $x_{qp} = N_{qp}V/n_{cp}$, extracted by converting the phase power spectral density to the spectrum of quasiparticle fluctuations, $S_N(f)$ (Eq. 4.4), and fitting to a Lorentzian. The black line is the approximate analytical expression [37] for the reduced quasiparticle density. (b) The product, $N_{qp}\tau_{qp}$ should be independent of temperature (grey dashed line). However, using N_{qp} and τ_{qp} extracted from the spectrum of quasiparticle fluctuations, we find a significantly lower value. The addition of a 20 μs trapping time (consistent with [39, 40]), gives reasonable agreement with data.

and the number of quasiparticles to be constant for a thermal quasiparticle distribution. We can check this, using N_{qp} and τ_{qp} extracted from Lorentzian fits to the spectrum of quasiparticle fluctuations. For our device geometry, we expect $N_{qp}\tau_{qp} \approx 0.165$, however, we find something significantly lower (Fig. 4.8). This is due to the fact that the quasiparticle lifetime saturates at a much shorter timescale than expected. This is likely due to quasiparticle trapping. Trapping rates of $(17.6\,\mu\text{s})^{-1}$ have been measured for devices in our lab [39], comparable to those reported by other groups [40]. Adding the trapping time in parallel with the predicted quasiparticle recombination time, Eq. 2.4

$$\frac{1}{\tau_{qp}^{\text{eff}}} = \frac{1}{\tau_{qp}} + \frac{1}{\tau_{\text{trap}}} \tag{4.19}$$

we define an effective quasiparticle recombination time that describes the characteristic timescale extracted from fits. The addition of trapping results in reasonable agreement with the data.

Having investigated the detector response to a thermal quasiparticle distribution, we move to calibrate the detector by looking at the response to a known photon flux emitted by a blackbody source in Chapter 5.

Chapter 5

Calibration with a blackbody source

We need to quantify the sensitivity of our detector to electromagnetic radiation in order to compare the performance with other detector designs. There are two quantities which can be used to describe detector performance:

- Noise equivalent power (NEP): the incident power which can be detected with a signal to noise ratio of one for a post-detection bandwidth of 1 Hz.
- Optical efficiency (η_{opt}): the efficiency with which the detector absorbs incident photons.

Both quantities can be measured by looking at the response of the detector to a source with a known radiation frequency and power. Blackbody radiators are commonly used for this type of calibration ([23, 28, 41–46]). We begin by discussing contributions to the noise equivalent power for our system, before giving details of the blackbody apparatus. We measure the experimental noise equivalent power, varying the incident radiation power. Taking the value of the NEP for a single frequency, $f < 1/2\pi\tau_{qp}$ and plotting as a function of incident power we compare with the predicted background-limited NEP. We then go on to calculate an NEP using noise spectra measured on the dark device (see Chapter

4), using the calculated frequency-dependent optical efficiency, averaged over a frequency band centered on the slot antenna resonance.

5.1 Background-limited Noise Equivalent Power

Discussing the contributions to the background-limited noise equivalent power of a pair-breaking detector we follow the work of [10, 23, 45]. To be careful about the distinguishing between power incident to the detector and power absorbed by the detector throughout this discussion, we define them explicitly here:

- Incident power[1]:

$$P_s = \int S(f,T)df \tag{5.1}$$

  where $S(f,T)$ is the blackbody spectral density. A derivation of $S(f,T) = \frac{hf}{e^{hf/k_BT}-1}$ for our experimental apparatus is given in the following Section.

- Power absorbed by the detector:

$$P_{\text{abs}} = P_s \int \eta_{\text{opt}}(f)df = \int \eta_{\text{opt}}(f)S(f,T)df \tag{5.2}$$

  where $\eta_{\text{opt}}(f)$ is the frequency dependent optical efficiency.

A derivation of each of these quantities, specific to our experimental setup is given in the following section.

A detector is considered background-limited if it is limited by the signal-to-noise ratio of the source [45]. In the case where the detector is subjected to radiation emitted by a blackbody, this corresponds to a detector sensitivity limited by fluctuations in the random arrival rate of photons at the detector, photon shot noise[2] (s.n.).

$$\text{NEP}^2_{\text{s.n.}} = \int 2\frac{S(f,T)hf}{\eta_{\text{opt}}}df \tag{5.3}$$

[1]This quantity is similar to the power emitted by the blackbody source, however, our expression for $S(f,T)$ takes into account the effective sensing area of the detector and the fact that the detector is only sensitive to a single polarization of radiation.

[2]Some sources refer to this term as $\text{NEP}_{\text{Poisson}}$ [23, 45]

There will be a correction to Eq. 5.3 to account for photon bunching[3] (b.c.).

$$\mathrm{NEP}^2_{\mathrm{b.c.}} = \int 2S(f,T)\frac{hf}{e^{hf/k_BT}-1}df \tag{5.4}$$

This term is negligible for the powers accessed in this work. Finally, a pair-breaking detector, which monitors changes in the quasiparticle distribution of a superconducting volume, will further be limited by quasiparticle number fluctuations or generation-recombination noise (g-r) [47].

$$\mathrm{NEP}^2_{\mathrm{g\text{-}r}} = \int 2\Delta\frac{S(f,T)}{\eta_{\mathrm{opt}}\eta_{\mathrm{pb}}}df \tag{5.5}$$

where $\eta_{\mathrm{pb}} \approx 0.69$ is the pair-breaking efficiency [48]. The total background limited noise equivalent power will be the sum of these contributions in quadrature.

$$\mathrm{NEP}^2_{\mathrm{blip}} = \int \underbrace{\frac{2S(f,T)hf}{\eta_{\mathrm{opt}}}}_{\text{photon shot noise}} df + \int \underbrace{\frac{2S(f,T)hf}{e^{hf/k_BT}-1}}_{\text{bunching corr.}} df + \int \underbrace{\frac{2\Delta S(f,T)}{\eta_{\mathrm{opt}}\eta_{\mathrm{pb}}}}_{\text{generation-recombination}} df \tag{5.6}$$

Our experimental setup does not include filters between the blackbody source and the detector to confine radiation to a narrow frequency band [23]. As a result, we leave each equation as an integral involving the frequency dependent optical efficiency and the emitted power per unit frequency.

5.2 Blackbody construction

When designing the blackbody apparatus, there are a number of practical considerations we must to take into account.

- We would like to heat the blackbody to high enough temperature such that the detector becomes photon-limited (i.e. photon shot noise is the dominant contribution to Eq. 5.6).

- We should be able to heat the blackbody to sufficiently high temperatures without

[3] Some sources refer to this term as $\mathrm{NEP}_{\mathrm{wave}}$

affecting the fridge operation. That is, we need to ensure that the detector response is due solely to incident radiation from the blackbody source, not spurious heating effects.

- We would like to limit the arrival of photons from higher temperature stages at the detector.
- Preferably, the time constant for the blackbody to settle at a temperature aught to be short, minutes, at most.

In this section, we address each of these design considerations before giving details of the experimental blackbody apparatus. In order to estimate expected contributions to the noise equivalent power, we must first estimate the power emitted by the blackbody source, P_s, and the power absorbed by the detector, P_{rad}.

5.2.1 Power emitted by the blackbody

To understand the response of our detector to incident power from the blackbody source, we must calculate the power emitted by the blackbody. We start from the Planck spectrum

$$B(f) = \frac{2hf^3}{c^2}\frac{1}{e^{hf/k_BT} - 1}. \tag{5.7}$$

We can calculate the power emitted by the blackbody, P_s, by integrating over the radiation frequency, effective sensing area of the detector, $A(f)$, and the solid angle, Ω

$$P_s = \frac{1}{2}\int\int B(f)A(f)d\Omega df. \tag{5.8}$$

Note the additional factor of one half to account for the fact that our detector will only absorb a single radiation polarization. If filters were used in the the blackbody apparatus, the frequency response of the filters would need to be included in the integrand as well

[45]. The effective sensing area of the detector is

$$A = \frac{\lambda^2}{4\pi} = \frac{c^2}{4\pi f^2}. \tag{5.9}$$

The blackbody apparatus was designed with a reflective sample enclosure and chimney, allowing us to assume immersion in a blackbody. Hence the solid angle will be that of a sphere. The integral in Eq. 5.8 is then

$$P_s = \frac{1}{2}\int\int_{\theta=0}^{\theta=\pi}\int_{\phi=0}^{\phi=2\pi} \frac{2hf^3}{c^2}\frac{1}{e^{hf/k_BT}-1}\frac{c^2}{4\pi f^2}\sin\theta df d\theta d\phi \tag{5.10}$$

$$P_s = \int \frac{hf}{e^{hf/k_BT}-1}df = \int S(f,T)df. \tag{5.11}$$

Note the temperature dependence as well as the frequency dependence. Evaluating Eq. 5.11 for our measured blackbody temperature and integrating from twice the Al gap edge, we calculate the power emitted by the blackbody source.

5.2.2 Power absorbed by the detector

We can extend this calculation to estimate the power absorbed by the detector, $P_{\rm abs}$. To do this, we must include the frequency-dependent efficiency, $\eta_{\rm opt}(f)$ [30]

$$P_{\rm abs} = P_s\int \eta_{\rm opt}(f)df = \int \frac{hf}{e^{hf/k_BT}-1}\eta_{\rm opt}(f)df. \tag{5.12}$$

Using the frequency-dependent radiation impedance simulated in CST Microwave Studio [29], we can calculate the coupling efficiency (see Chapter 2 for details). From this, we can estimate $P_{\rm abs}$. The emitted blackbody spectrum as a function of radiation frequency is shown in Fig. 5.1 (a), along with the simulated efficiency, $\eta_{\rm opt}(f)$. The absorbed spectral density is shown in Fig. 5.1 (b). We integrate the curve for each of temperature to calculate P_s and $P_{\rm abs}$ (shown in Fig. 5.2). As expected, the absorbed power is lower than the emitted power. To know the exact absorbed power we require a measurement of the optical efficiency. The normalized cumulative absorbed power is shown in Fig. 5.2

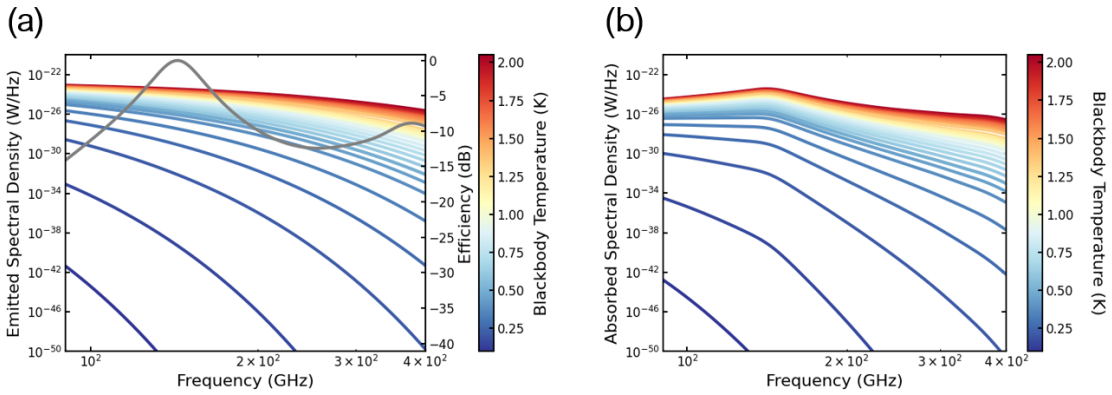

Figure 5.1: Blackbody spectrum. (a) The blackbody spectral density is shown as a function of radiation frequency for the range of temperatures accessed in this experiment. The simulated efficiency is plotted in gray (right y-axis). (b) The estimated absorbed spectral density as a function of radiation frequency, the result of multiplying the simulated efficiency with the blackbody spectrum for each temperature.

(b), calculated by varying the upper limit of the integrand in Eq. 5.12. We see that, as expected, most of the radiation is absorbed in a relatively narrow band centered around the antenna frequency ($f_{\text{ant}} \approx 140$ GHz). These results will be used in the calculation of the detector responsivity in the following sections.

5.2.3 Expected contributions to NEP

Having calculated the power emitted by the blackbody source, we can estimate contributions to the noise equivalent power. This will inform what range of operation temperatures to target when designing the blackbody emitter. Fig. 5.3 (a) shows the contributions to NEP due to radiation from the blackbody source for blackbody temperatures ranging between 100 mK and 5 K. We see that at low temperatures generation-recombination noise, due to quasiparticles generated by the absorption of radiation from the blackbody, will dominate. However, starting around 1 K, the photon shot noise becomes the dominant source of noise (Fig. 5.3 (b) shows the calculated contributions to NEP for blackbody temperatures ranging between 1 K and 5 K). In order to access the photon-limited regime, we would like to be able to heat the blackbody to a few Kelvin without disrupting normal operation of the cryostat. For our design, we mount the blackbody to the exchange plate

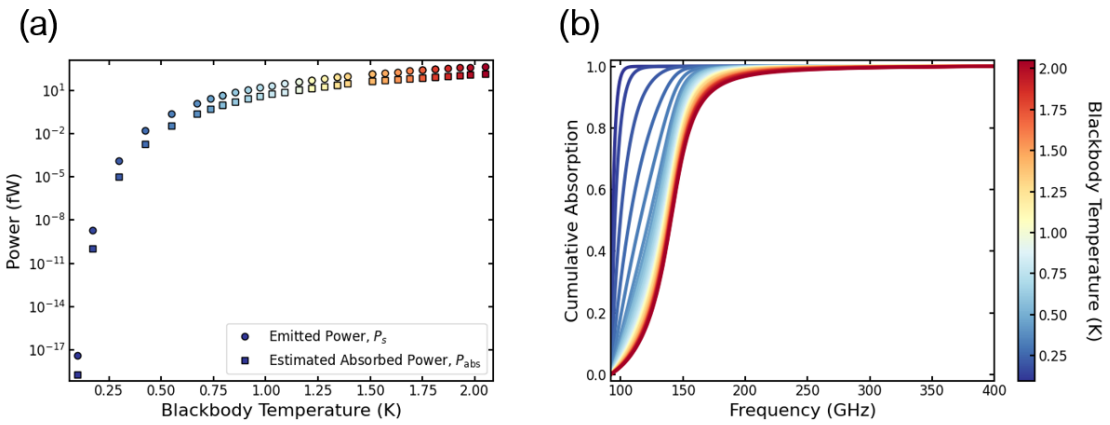

Figure 5.2: Calculated blackbody power. (a) Calculated emitted (circles) and absorbed (squares) power. The result of integrating the curves shown in Fig. 5.1 (a) and (b), respectively. (b) The cumulative absorbed power, plotted for the range of simulated radiation frequencies. Each curve is normalized by the absorbed power calculated when integrating over the whole frequency range. From this plot we see that most of the radiation is absorbed at the antenna frequency, in the lower half of the simulated frequency range.

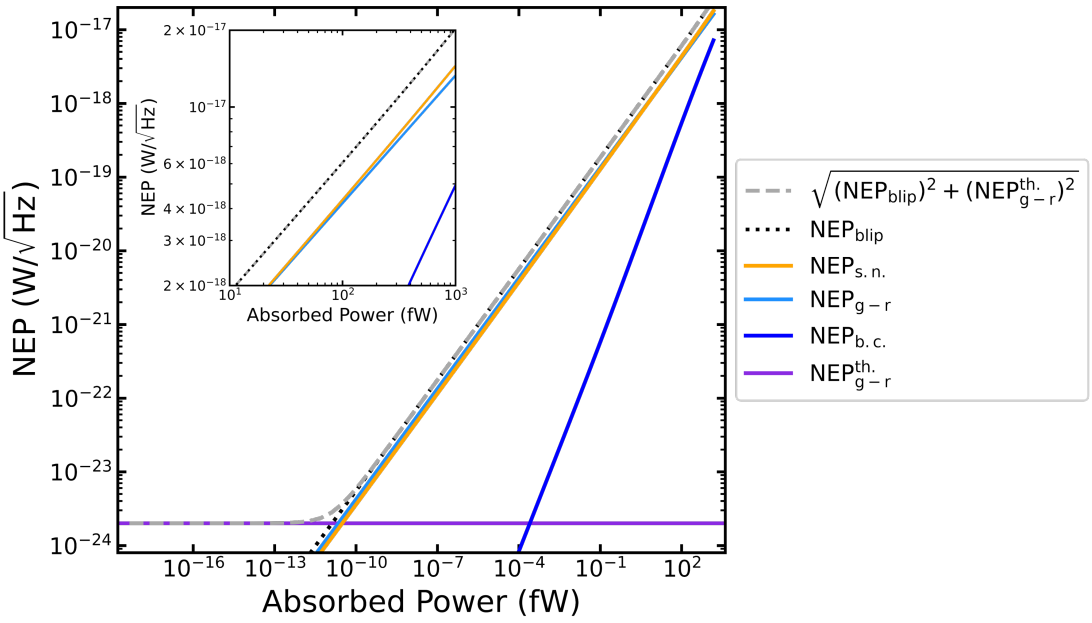

Figure 5.3: Contributions to the noise equivalent power (Eq. 5.3 - Eq. 5.6) for blackbody temperatures ranging between 100 mK and 5 K. $NEP^{th.}_{g\text{-}r}$ is the contribution to NEP due to generation-recombination noise of a thermal quasiparticle distribution [23], evaluated for a device temperature of 20 mK. For blackbody temperatures above 200 mK we will not be limited generation-recombination noise due to the ambient device temperature. The inset shows the same contributions to NEP, for blackbody temperatures above 1 K where the background-limited NEP is dominated by the contribution due to photon shot noise.

(with base temperature around 100 mK), while the sample is mounted to the top of the mixing plate (which typically sits around 20 mK). In order to successfully measure quasiparticle fluctuations due to absorption of radiation from the blackbody, we must reduce sources of excess quasiparticles, for instance due to light leakage from higher temperature stages. To do this, we use a sample box with an integrated chimney (Fig. 5.4 (a)), which is inserted into blackbody. The blackbody, extending around the chimney is coated with an absorptive mixture. Incident light from higher temperature stages would be absorbed by this coating, instead of reaching the sample. Further, by mounting the sample to a lower temperature stage, we reduce the expected contribution to noise equivalent power due to generation recombination noise of a thermal quasiparticle distribution at the device temperature. Evaluating Eq. 2.2 and Eq. 2.4 for a device temperature of 20 mK, we calculate the contribution due to generation and recombination of this thermal distribution [23]

$$\mathrm{NEP}^{\mathrm{th.}}_{\mathrm{g\text{-}r}} = \frac{2\Delta}{\eta_{\mathrm{pb}}\eta_{\mathrm{opt}}}\sqrt{\frac{N_{qp}}{\tau_{qp}}} \tag{5.13}$$

using the simulated optical efficiency. This gives $\mathrm{NEP}^{\mathrm{th.}}_{\mathrm{g\text{-}r}} \approx 2 \times 10^{-24}$ W Hz$^{-1/2}$, which for blackbody temperatures above 1 K, is six orders of magnitude less than the contribution from photon shot noise. In normal circulation, this contribution should not be a concern. The blackbody apparatus is designed to ensure that operation of the blackbody does not interrupt normal fridge operation. Details of the blackbody design can be found in the subsequent Section.

5.2.4 Description of the blackbody apparatus

The blackbody used in these experiments consisted of $1\frac{1}{4}$ inch to 1 inch Cu reducer, which was capped at the 1 inch diameter end to create a cup. This cup was then coated with Eccosorb CR110 to create the blackbody. A resistive heater, attached to the capped end of the blackbody, was used to vary the blackbody from 90 mK to 3 K. Additionally, a RuOx thermometer was anchored to the top of the blackbody to allow for accurate temperature readout. Calibration of these devices took place in a Leiden cryogen-free

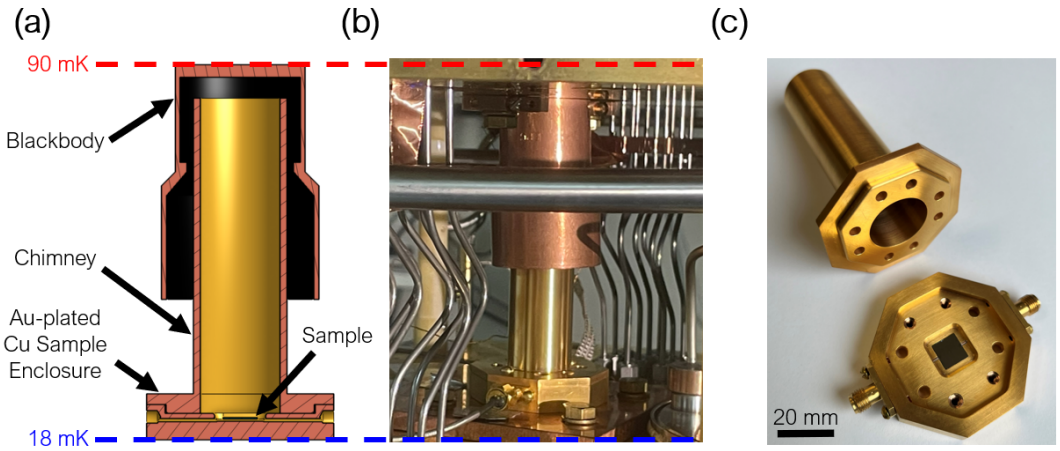

Figure 5.4: Blackbody apparatus. (a) CAD assembly showing a cross-section of the Au-plated Cu sample box with integrated chimney and the blackbody. (b) The sample box and blackbody mounted in the dilution refrigerator. The sample box is mounted to the refrigerator's mixing plate, which has a base temperature of 18 mK. The blackbody is weakly thermally coupled to the exchange plate, which typically resides at 90 mK while the fridge is in normal circulation. (c) The Au-plated sample box and the sample box lid, with integrated chimney. The sample sits in a 8 mm by 8 mm pocket. SMA connectors are soldered to Cu trace on Rogers board launchers, from which wirebonds can be placed in order to connect the on-chip feedline with the microwave lines in the fridge.

dilution refrigerator. Samples under test were mounted to the mixing chamber plate with a base temperature of approximately 18 mK. The blackbody emitter was weakly thermally anchored to the exchange plate of the dilution refrigerator using 1 inch long stainless steel 4-40 screws.

5.3 NEP due to incident power

Having calculated the incident power, P_s, we can now calculate the experimental noise equivalent power, $\mathrm{NEP}_{\mathrm{exp}}(P_s, f)$. This can be done for either amplitude or phase with expressions given by [23, 28].

$$\mathrm{NEP}_{\mathrm{exp}}(P_s, f) = \sqrt{S_{A,A}(f)}\left(\frac{dA}{dP_s}\right)^{-1}\sqrt{1+(2\pi f\tau_{qp})^2} \tag{5.14}$$

$$\mathrm{NEP}_{\mathrm{exp}}(P_s, f) = \sqrt{S_{\theta,\theta}(f)}\left(\frac{d\theta}{dP_s}\right)^{-1}\sqrt{1+(2\pi f\tau_{qp})^2} \tag{5.15}$$

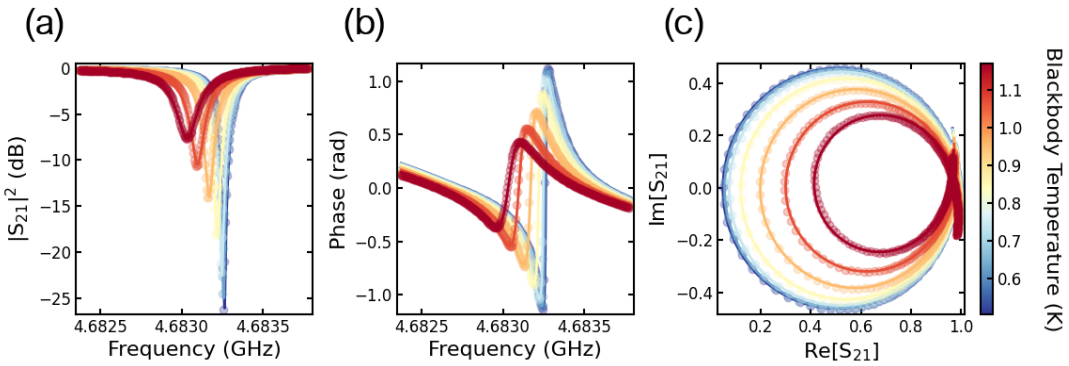

Figure 5.5: Resonator response to elevated blackbody temperature. Data and fits for a subset of blackbody temperatures. (a) Transmission across the resonator as a function of readout frequency. A shift down in resonant frequency and a decrease in quality factor are both apparent with increasing blackbody temperature. (b) Phase as a function of readout frequency. (c) The real and imaginary parts of transmission plotted in the complex plane. Q_i and f_0 are extracted by fitting a circle to the data. The color bar indicates blackbody temperature, T_{bb}, for a given dataset.

$S_{A,A}(f)$ and $S_{\theta,\theta}(f)$ denote the measured power spectral density of amplitude or phase fluctuations, respectively. dA/dP_s and $d\theta/dP_s$ are the amplitude and phase responsivity, that is the change in amplitude or phase due to a change in the incident power. τ_{qp} is the experimentally observed quasiparticle lifetime. In the following two sections, we step through how each of these quantities is measured experimentally.

5.3.1 Detector responsivity

In Chapter 4 we extracted the amplitude and phase responsivity due to a thermal quasiparticle distribution from the measured internal quality factor and resonant frequency as a function of bath temperature. We take a similar approach to measuring the amplitude and phase responsivity due to illumination with a blackbody emitter. Note that another method for measuring the responsivity of the detector involves monitoring the change in amplitude or phase while the blackbody temperature is varied in time [23]. The longer (order of 10 min) time constant of our blackbody made this infeasible. Hence, we start from measurements of the resonator taken for each blackbody temperature with a vector network analyzer. The internal quality factor and resonant frequency is extracted by

fitting a circle to the real and imaginary parts of S_{21} [24, 36]. Data, along with fits, is shown in Fig. 5.5. The fractional frequency shift and change in the loss, determined from these fits is shown in Fig. 5.6 as a function of blackbody temperature, T_{bb}. Converting blackbody temperature to incident power as described in Section 5.2.1, we see that the data falls onto a line (Fig. 5.6 (c) and (d)). Fitting a line to the data, the slope gives the change in $\delta f/f_0$ or $\delta(1/Q_i)$ due to a change in P_s.

Converting from Q_i and f_0 to amplitude and phase using Eq. 2.59 and Eq. 2.60 we now have the amplitude responsivity and phase responsivity

$$\frac{dA}{dP_s} = -2Q\frac{d(1/Q_i)}{dP_s} \tag{5.16}$$

$$\frac{d\theta}{dP_s} = -4Q\frac{df/f_0}{dP_s}. \tag{5.17}$$

The responsivity depends on the total quality factor, shown in Fig. 5.7 (a), alongside the amplitude and phase responsivity as a function of incident power. The amplitude and phase responsivity will be used to compute the experimental NEP (Eq. 5.14 and Eq. 5.15). To calculate the experimental noise equivalent power from Eq. 5.14 and Eq. 5.15 we require the amplitude power spectral density and phase power spectral density, respectively. These are acquired in the same way as described in Chapter 4. For each blackbody temperature, we first determine the resonant frequency, f_0, and the angle required to orthogonalize the amplitude and phase signals in the IQ plane [25]. We repeatedly read out on resonance to generate a timeseries. The power spectral density is computed by taking the Fourier transform of each of the timeseries. This is repeated 1,000 times and the average is taken of the resulting 1,000 PSDs. The result is shown in Fig. 5.8. The last quantity required before we can compute the experimental NEP is the quasiparticle lifetime, τ_{qp}, which we extract by fitting a Lorentzian to the noise spectrum. For low temperatures, we find significant $1/f$ noise at low frequencies, and in this case a $1/f^{\alpha}$ component is added to the fit function. In spite of this, it is still not possible to fit to the lowest temperature datasets. The last temperature for which we can reliably extract

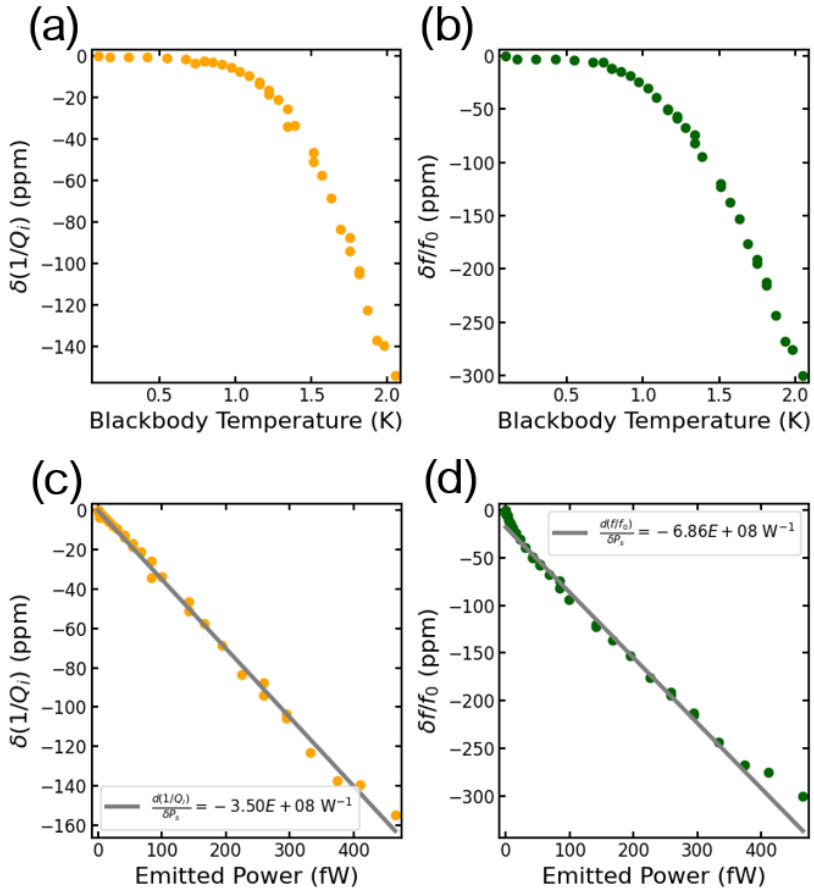

Figure 5.6: Change in internal quality factor and resonant frequency due to incident radiation from a blackbody emitter. (a) The change in the resonator loss, $\delta(1/Q_i)$. (b) The fractional frequency shift, $\delta f/f_0$. (c) The change in the resonator loss as a function of incident power. A linear fit to the data gives the change in $\delta(1/Q_i)$ due to a change in P_s. (d) The change in the fractional frequency as a function of the incident power, P_s, from which the amplitude responsivity can be computed. The linear fit gives the detector response in $\delta f/f_0$ due to a change in P_s, from which the phase responsivity may be computed.

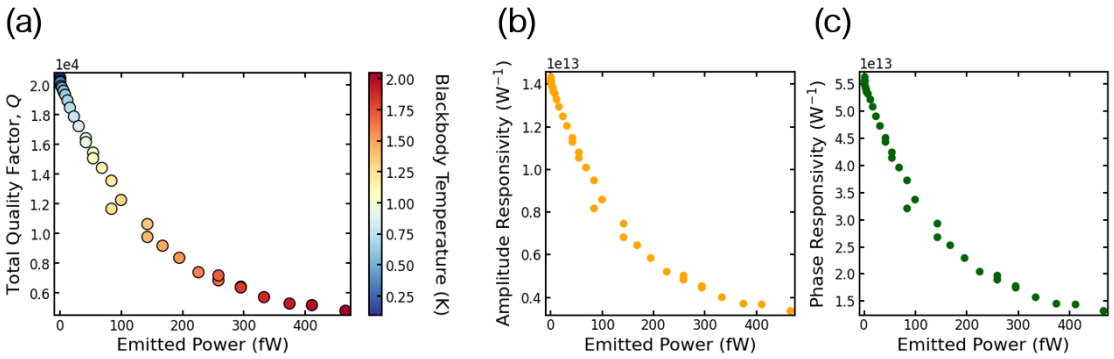

Figure 5.7: Detector responsivity to incident power. (a) The total quality factor, Q, plotted versus incident power. The color of the markers indicates the blackbody temperature. (b) Amplitude responsivity. (c) Phase responsivity.

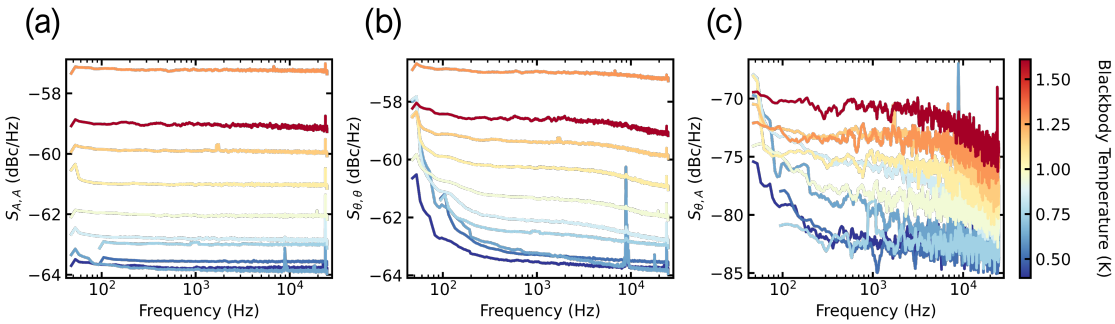

Figure 5.8: Detector noise for varying blackbody temperature. (a) Amplitude power spectral density. (b) Phase power spectral density. (c) Amplitude-phase cross-spectral density. The noise level is lowest in the cross spectrum, which looks at correlated noise sources of noise. As such, uncorrelated sources of noise (ex. due to the measurement setup) are not present in the cross spectrum [11].

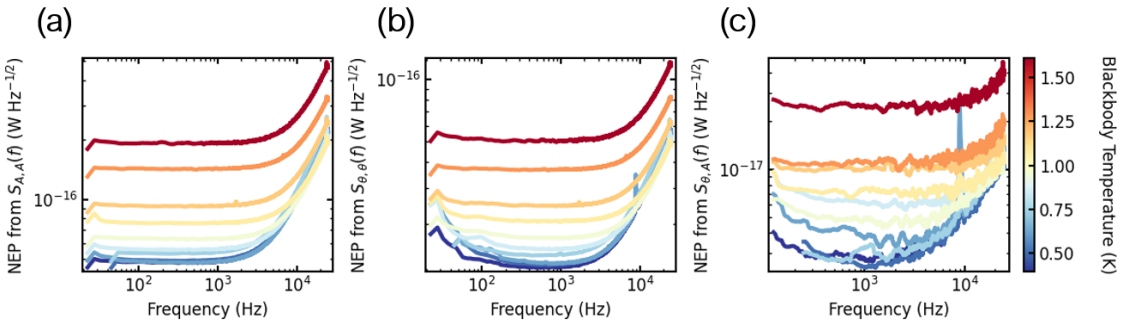

Figure 5.9: Experimental noise equivalent power, $\mathrm{NEP}_{\mathrm{exp}}(P_s)$. P_s is the power emitted by the blackbody source. (a) $\mathrm{NEP}_{\mathrm{exp}}(P_s)$ derived from the amplitude power spectral density, $S_{A,A}(f)$. (b) $\mathrm{NEP}_{\mathrm{exp}}(P_s)$ derived from the phase power spectral density, $S_{\theta,\theta}(f)$. $\mathrm{NEP}_{\mathrm{exp}}(P_s)$ computed from the cross spectral density, $S_{\theta,A}(f)$.

a quasiparticle lifetime is $T_{bb} = 740$ mK. We use the value of the quasiparticle lifetime extracted at this temperature for all lower temperature datasets. Finally, we can compute the experimental noise equivalent power, $\mathrm{NEP}_{\mathrm{exp}}(P_s)$, shown in Fig. 5.9. We calculate a noise equivalent power from the cross spectral density

$$\mathrm{NEP}_{\mathrm{exp}}(P_s, f) = \sqrt{S_{\theta,A}(f)}\left(\frac{d\theta}{dP_s}\frac{dA}{dP_s}\right)^{-1/2}\sqrt{1+(2\pi f\tau_{qp})^2} \tag{5.18}$$

This type of detector is typically read out by monitoring changes in *either* amplitude or *phase*, in which case one would quote the NEP calculated from amplitude or phase power spectral density, respectively. However, for the purpose of demonstrating an understanding of the detector response, the NEP calculated from the cross spectrum is useful as it does not include sources of uncorrelated noise due to the experimental apparatus, such as amplifier noise.

For each of the panels in Fig. 5.9, we plot the measured $\mathrm{NEP}_{\mathrm{exp}}(P_s)$ at a frequency $f < 1/2\pi\tau_{qp}$, in this case 500 Hz versus the incident radiation power, P_s (shown in Fig. 5.10. $f = 500$ Hz was chosen to be below the upturn in NEP corresponding to the quasiparticle lifetime, and sufficiently above the $1/f$ noise at low frequencies. For a photon-limited detector, we expect the noise equivalent power to scale as the square root of the incident power [23]. To check this, we fit the high power points to a power law, finding

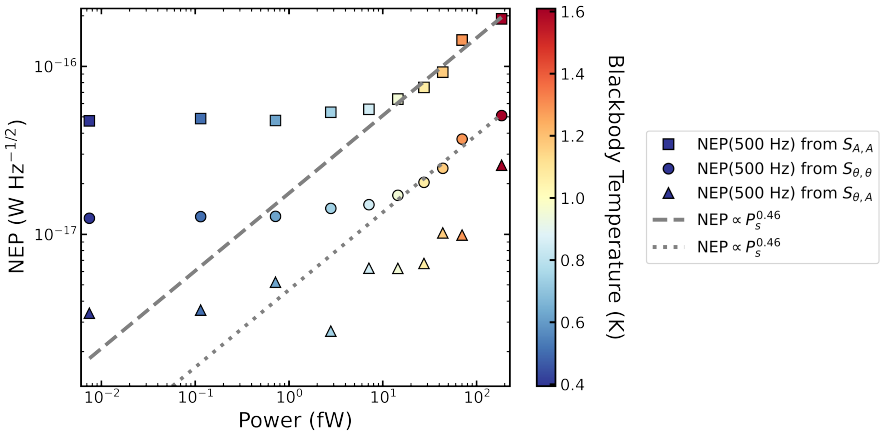

Figure 5.10: Power law fit to $\mathrm{NEP}_{\mathrm{exp}}(P_s)$. In the case of a photon-limited noise equivalent power, we expect NEP $\propto \sqrt{P}$. We find that the NEP calculated from both the amplitude PSD and the phase PSD are proportional to $\sqrt{P_s}$, as expected.

that our measured $\mathrm{NEP}_{\mathrm{exp}} \propto P_s^{0.46}$. As a result we can compare the measured $\mathrm{NEP}_{\mathrm{exp}}$ with the calculated background limited $\mathrm{NEP}_{\mathrm{blip}}$ (Eq. 5.6). When evaluating Eq. 5.6 we use the optical efficiency calculated from Eq. 2.63 using the radiation impedance simulated in CST Microwave Studio [29]. For the junction normal state resistance we use the average room temperature resistance of on-chip witness junctions. The junction capacitance is estimated from measurements of the junction area taken using a scanning electron microscope, assuming a capacitance per unit area of 75 fF/μm^2. The result is shown in Fig. 5.11. We find good agreement with the noise equivalent power calculated from the cross spectrum for high powers. At low powers we observe a saturation of the NEP, similar to that observed by others [23, 43]. We account for this saturation in the same way as was done in [43], add a constant NEP in quadrature with $\mathrm{NEP}_{\mathrm{blip}}$. In our case, we cannot determine the source of this saturation. It could be due to the microwave readout tone, as was found in [23], or stray photons from higher temperature stages, among other possibilities. $\mathrm{NEP}_{\mathrm{exp}}(P_s)$ calculated from the amplitude PSD and phase PSD are both higher than that calculated from the cross spectrum, indicating excess sources of uncorrelated noise due to the experimental apparatus.

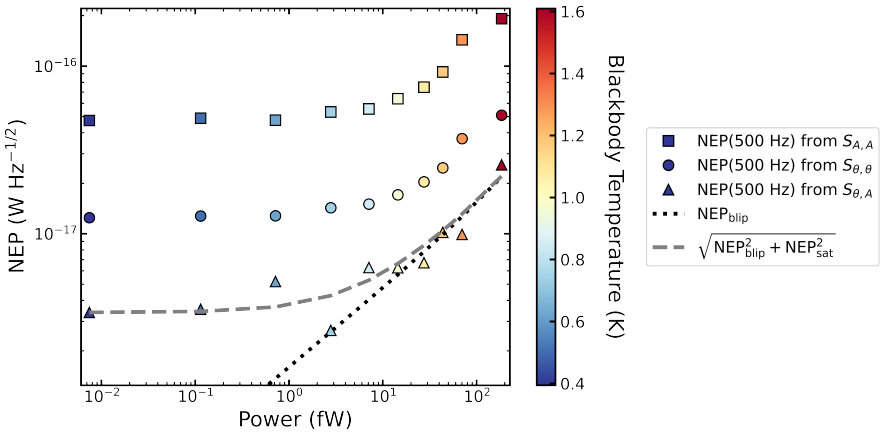

Figure 5.11: Noise equivalent power as a function of incident power, P_s. P_s is calculated using Eq. 5.11 from the measured blackbody temperature (indicated by the marker color). Square markers correspond to $\mathrm{NEP_{exp}}(P_s)$ derived from the amplitude PSD, at $f = 500$ Hz. Circular and triangular markers are the same quantity for the $\mathrm{NEP_{exp}}(P_s)$ derived from the phase PSD and CSD, respectively. The black dotted line is the background-limited NEP, $\mathrm{NEP_{blip}}$, calculated from Eq. 5.6 using the simulated, frequency-dependent optical efficiency. We observe a saturation in the NEP at low powers. The dashed grey line is the result of adding a constant term, $\mathrm{NEP_{sat}}$ in quadrature with $\mathrm{NEP_{blip}}$, as was done in [43]. We find good agreement between the theoretical background limited NEP and the experimental NEP derived from the cross spectrum. This suggests the presence of excess uncorrelated noise, such as amplifier noise or TLS noise.

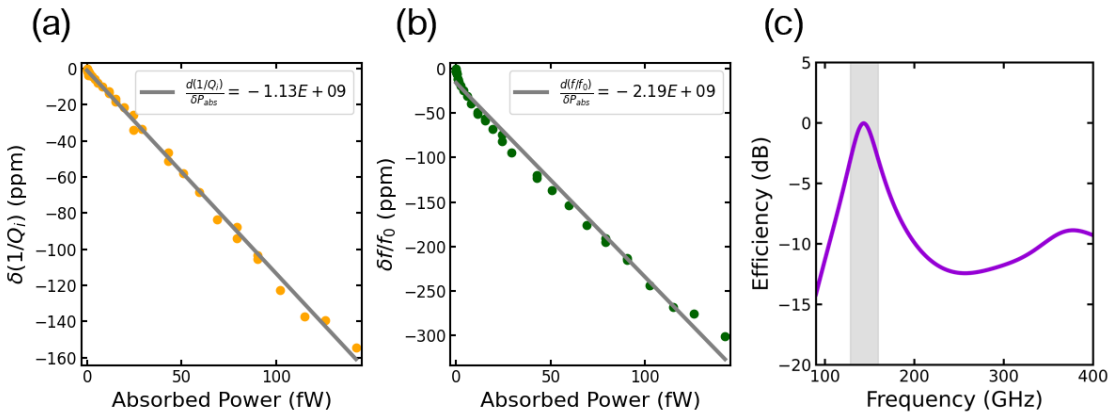

Figure 5.12: (a) Change in $\delta(1/Q_i)$ as a function of the power absorbed by the detector. (b) Change in the $\delta f/f_0$ as a function of the power absorbed by the detector. The amplitude and phase response to $P_{\rm abs}$ is calculated from a linear fit to the data. (c) The frequency dependent efficiency, calculated from Eq. 2.63. The grey region indicates the frequency band defined by a 3 dB decrease in efficiency on either side of the slot antenna resonance. The average optical efficiency, $\bar{\eta_{\rm opt}} = 0.78$, is calculated by integrating over this frequency band.

5.4 Estimation of the dark NEP

Having demonstrated reasonable agreement between the measured $\mathrm{NEP}_{\rm exp}(P_s)$ and the theoretical background-limited $\mathrm{NEP}_{\rm blip}$, we can now estimate an efficiency for the detector which will allow us to calculate a noise equivalent power under dark conditions, $\mathrm{NEP}_{\rm dark}$. We calculate the average optical efficiency by integrating the calculated frequency-dependent efficiency.

$$\bar{\eta_{\rm opt}} = \frac{\int_{f_1}^{f_2} \eta_{\rm opt}(f) df}{f_2 - f_1} \tag{5.19}$$

For the limits of integration we chose a frequency defined by a 3 dB decrease in efficiency on either side of the slot antenna resonance (shown in Fig. 5.12 (c)). Evaluating Eq. 5.19 we find $\bar{\eta_{\rm opt}} = 0.78$.

We calculate a noise equivalent power from the noise spectra measured on the dark device (Chapter 4). In order to do this, we must first relate the measured response due to a change in the number of quasiparticles, dA/dN_{qp} and $d\theta/dN_{qp}$, to a change in the power

at the detector. Following [23], these quantities are related by

$$\eta_{\rm pb}\eta_{\rm opt}P = \frac{\Delta N_{qp}}{\tau_{qp}} \tag{5.20}$$

Thus, the response due to a change in the number of quasiparticles can be related to the response due to power at the detector as

$$\frac{dA}{dP} = \frac{\eta_{\rm pb}\eta_{\rm opt}\tau_{qp}}{\Delta}\frac{dA}{dN_{qp}} \tag{5.21}$$

and

$$\frac{d\theta}{dP} = \frac{\eta_{\rm pb}\eta_{\rm opt}\tau_{qp}}{\Delta}\frac{d\theta}{dN_{qp}} \tag{5.22}$$

Using these equations we arrive at an expression for the noise equivalent power measured under dark conditions

$$\mathrm{NEP}_{\rm dark} = \sqrt{S_X}\left(\frac{\eta_{\rm pb}\eta_{\rm opt}\tau_{qp}}{\Delta}\frac{dX}{dN_{qp}}\right)^{-1}\sqrt{1+(2\pi f\tau_{qp})^2} \tag{5.23}$$

We calculate this using the amplitude and phase power spectral densities and detector response measured on the dark sample (Chapter 4), and the average optical efficiency, $\bar{\eta_{\rm opt}} = 0.78$. We estimate the pair-breaking efficiency at the slot antenna's resonant frequency to be $\eta_{\rm pb} \approx 0.69$ [48]. $\Delta = 190\,\mu$eV is the superconducting energy gap of aluminum. τ_{qp} is the quasiparticle lifetime extracted from Lorentzian fits to the power spectral density (Chapter 4). The resulting $\mathrm{NEP}_{\rm dark}$ is shown in Fig. 5.13. We find that that $\mathrm{NEP}_{\rm dark}$ calculated from the amplitude power spectral density is about a factor of 5 higher than that calculated from the phase spectrum. This is consistent with experimental noise equivalent power measured on the sample subjected to illumination by the blackbody. That we see the same discrepancy across both samples indicates excess amplitude noise due to the experimental apparatus. The noise equivalent power of the dark device, measured at the cryostat's base temperature of 18 mK, has a value of $\mathrm{NEP}_{\rm dark} = 3.6\times10^{-20}$ W/$\sqrt{\rm Hz}$ at $f = 500$ Hz. This value is comparable to results measured for antenna-coupled

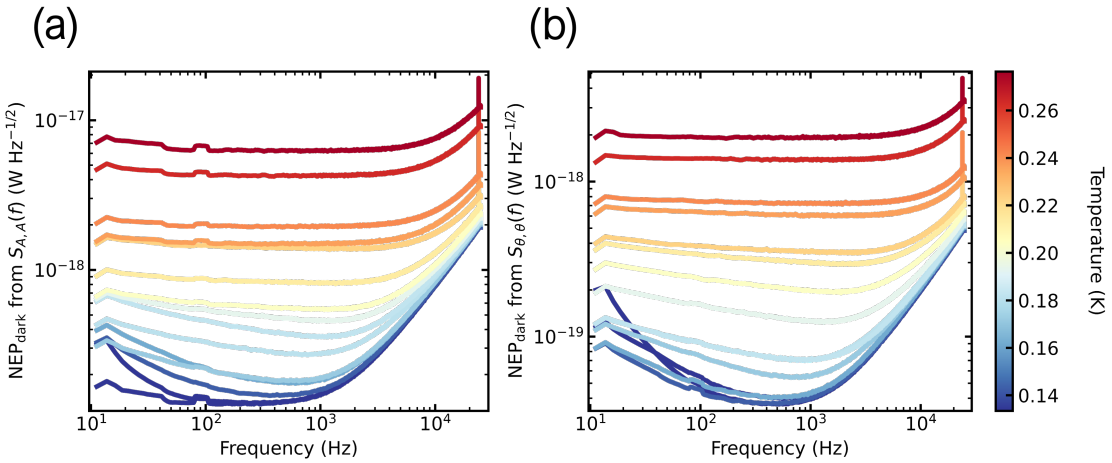

Figure 5.13: Noise equivalent power, $\mathrm{NEP_{dark}}$, calculated using noise spectra measured on the dark device (Fig. 4.5) from Eq. 5.23. When calculating $\mathrm{NEP_{dark}}$ we use the simulated optical efficiency averaged over a finite frequency band around the slot antenna frequency (shown in Fig. 5.12 (c).

microwave kinetic inductance detectors designed to operate around 1 THz [28].

Finally, using the average optical efficiency we can calculate the experimentally measured noise equivalent power, due to radiation absorbed by the device for the sample illuminated by the blackbody.

$$\mathrm{NEP_{exp}}(P_{\mathrm{abs}}, f) = \sqrt{S_{A,A}(f)}\left(\frac{dA}{dP_{\mathrm{abs}}}\right)^{-1}\sqrt{1+(2\pi f\tau_{qp})^2} \tag{5.24}$$

$$\mathrm{NEP_{exp}}(P_{\mathrm{abs}}, f) = \sqrt{S_{\theta,\theta}(f)}\left(\frac{d\theta}{dP_{\mathrm{abs}}}\right)^{-1}\sqrt{1+(2\pi f\tau_{qp})^2} \tag{5.25}$$

To do this, we recalculate the detector responsivity, using the absorbed power, P_{abs}, as defined in Eq. 5.12. This is done by plotting the change in the resonator loss and the fractional frequency shift as a function of P_{abs} (Fig. 5.12 (a) and (b)). The resulting $\mathrm{NEP_{exp}}(P_{\mathrm{abs}})$ is shown in Fig. 5.14.

Calibrating our detector with a blackbody source we found reasonable agreement between the noise equivalent power calculated using the cross spectral density. However, $\mathrm{NEP_{exp}}(P_s)$ derived from the amplitude and phase power spectral densities were higher, indicating a high level of background noise intrinsic to the experimental apparatus. Fu-

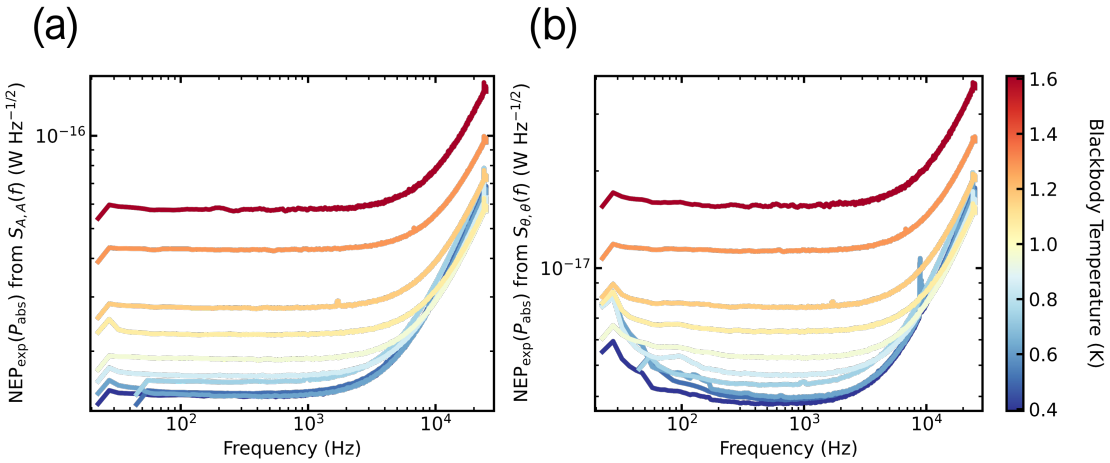

Figure 5.14: The experimental noise equivalent power, $\mathrm{NEP}_{\mathrm{exp}}(P_{\mathrm{abs}})$. P_{abs} is the power absorbed by the detector, calculated from Eq. 5.12 using the simulated optical efficiency, integrated over a frequency band defined by a 3 dB decrease in efficiency on either side of the antenna resonance (Fig. 5.12 (c)).

ture use of this particular blackbody apparatus for detector characterization will require improved shielding to reduce light leakage from higher temperature stages. In spite of this, we demonstrate reasonable agreement with the theoretical background limited noise equivalent power using the simulated frequency dependent optical efficiency. Improved shielding resulted in lower white noise levels for a dark reference sample, resulting in a competitive minimum noise equivalent power of $\mathrm{NEP}_{\mathrm{dark}} = 3.6 \times 10^{-20}\mathrm{W}/\sqrt{\mathrm{Hz}}$ at a frequency of 500 Hz.

Chapter 6

Spectroscopic characterization with a Josephson emitter

One of the shortcomings of our blackbody apparatus is that we're subjecting our detector to broadband radiation. Depending on the intended application for the detector, it may be more relevant to characterize detector performance over a small frequency band. In this case, it is common to use filters between the blackbody source and the sample to define a narrow frequency band around the detector resonance [23, 28, 45]. This however, requires separate characterization of the filter response [49]. An alternative would be to use a source that emits radiation over a narrow band of frequencies. A Josephson emitter [31], a patch antenna shunted by a DC-biased Josephson junction, provides such a source.

A DC biased Josephson junction will emit radiation at a well-defined frequency as a result of the AC Josephson effect. The frequency of the radiation emitted by this Josephson radiator can be easily swept by varying the DC voltage across the junction. By housing our detector in the same sample enclosure as a Josephson emitter, we can look at the spectral response of the detector due to radiation and a well-defined frequency. This type of transmit-receive experiment could provide another way to calibrate detectors. Further, this type of experiment would also provide a unique way to probe the non-equilibrium quasiparticle distribution since the Josephson emitter allows for injection at a

well defined frequency, and the detector will resonantly absorb pair-breaking radiation at a well-defined frequency. In this chapter we present preliminary results from a transmit receive experiment where we monitor the response of out detector to radiation emitted by Josephson emitter.

The Josephson emitter[1] consists of a voltage-biased Josephson junction to ground (Fig. 6.1 (a) and (b)). As discussed in Chapter 1, A DC voltage applied to the Junction will generate a time varying current (the AC Josephson effect)

$$I = I_0 \sin\left(\frac{2eV}{\hbar}t\right) \tag{6.1}$$

resulting in the emission of coherent radiation at the Josephson frequency

$$f_J = \frac{2eV}{h} = \left(\frac{484\,\mathrm{GHz}}{\mathrm{mV}} \times V\right) \tag{6.2}$$

As a result one can vary the frequency of the emitted radiation *in situ* by simply varying the DC voltage applied across the junction. The geometry of the Josephson emitter used in these experiments is shown in Fig. 6.1 (b). It consists of a superconducting patch, connected to the superconducting ground plane by a Josephson junction (the location of the Josephson junction is indicated in yellow). This superconducting island, is itself an antenna, in particular a patch antenna [30]. Thus, we expect the Josephson radiator to resonantly emit radiation at its antenna frequency. For a patch antenna, the wavelength of radiation corresponding to the antenna resonance will be approximately equal to one round trip around this patch, which for the geometry used in this experiment corresponds to frequency of approximately 250 GHz (Fig. 6.2). Josephson emitters, such as this, have previously been used to subject superconducting qubits to pair-breaking radiation in order to study quasiparticle poisoning of superconducting qubits [31]. Successful modeling of this transmit-receive experiment required an understanding of the radiation response of both Josephson emitter and the receiver antenna (in this case a superconducting qubit),

[1] Sometimes referred to as a Josephson radiator

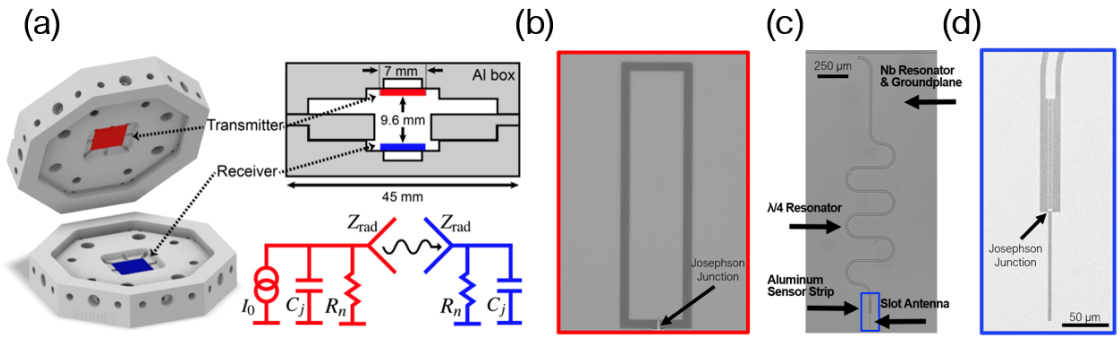

Figure 6.1: Transmit receive experiment. (a) Reproduced from Liu *et al*, 2024 [31]. Dual sample enclosure used for the transmit receive experiment. The Josephson emitter (red) was used to generate radiation at a well defined frequency while monitoring the response of the detector (blue). (b) Optical image of the Josephson emitter. (c) Optical image of the detector. The slot antenna is indicated in blue. (d) Scanning electron micrograph of the receiver antenna.

simulation of which was done in CST Microwave Studio [29].

In the experiment presented in this thesis, we used an almost identical dual-sample enclosure[2] and modeled the radiation response of the Josephson emitter and the detector in the same way using CST Microwave Studio. The sample configuration for the transmit-receive experiment is shown in Fig. 6.1 (a), reproduced from [31]. The emitter in this case is the Josephson radiator, introduced above (shown in Fig. 6.1 (b). The receiver is the slot-antenna embedded in our kinetic inductance detector (Fig. 6.1 (c) and (d)). A circuit diagram representation of the experiment is given in Fig. 6.1 (a).

Fabrication of the detector is described in Chapter 3. In the case of the Josephson emitter, the superconducting patch and ground plane are both made of Nb deposited via RF sputtering, and lithographically defined using optical lithography followed by a Cl-based etch (similar to the processing described in Chapter 3). The substrate is a high-resistivity Si(001) wafer. The Al-AlOx-Al Josephson junctions were defined in electron beam lithography and deposited via double-angle electron-beam evaporation with an *in situ* oxidation to create the oxide barrier. (Further details can be found in Chapter 3 and Appendix B.1). Al wirebonds are used to transfer the DC bias voltage from the sample

[2]The sample enclosure used in this work was a slightly modified version of that used in [31]. An Al spacer was added between the boxes to reduce losses due to the brass screws used to hold the boxes together in the cryostat.

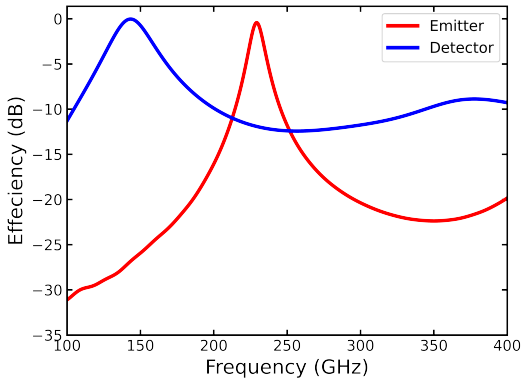

Figure 6.2: Calculated efficiencies relevant to the transmit-receive experiment. The calculated optical efficiency of the detector's slot antenna is shown in blue. The calculated efficiency of the Josephson emitter is shown in red. Both were calculated from Eq. 2.63 using the radiation impedance simulated with CST Microwave Studio and the measured room temperature resistance values of on-chip witness junctions. The slot antenna (receiver) is expected to resonate at 140 GHz. The patch antenna (emitter) is expected to resonate at 230 GHz.

enclosure's printed circuit board launchers to the patch. Samples were thermalized to the mixing plate of a Leiden cryogen-free dilution refrigerator and cooled to a temperature of 18 mK. The response of the detector was monitored by looking at transmission through the on-chip feedline using a vector network analyzer. The DC bias was applied to the Josephson emitter using an SRS SIM 928 voltage source.

We monitor the detector response in transmission while varying the DC voltage bias applied to the Josephson emitter (thus varying the frequency of the emitted radiation). The result is shown in Fig. 6.3 (a). The x-axis corresponds to the frequency of the radiation emitted by the voltage-biased Josephson junction (calculated using Eq. 6.2). Negative frequencies correspond to negative voltage biases, as a result, we expect the detector response to be approximately symmetric around zero voltage bias. We start with a qualitative discussion of features present in the dataset. We see a discontinuity just above $\pm$ 90 GHz, corresponding to twice the Al gap. There is a clear reduction in the internal quality factor of the resonator below 2Δ, suggesting that even for radiation frequencies below $2\Delta/h \approx 92$ GHz we are generating quasiparticles in the detector's Al

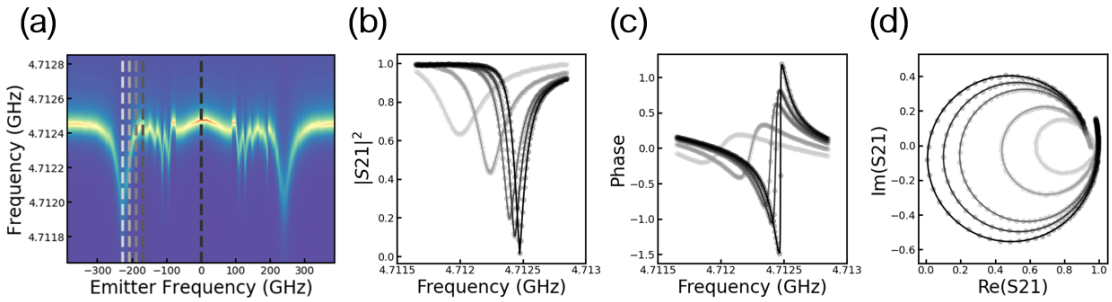

Figure 6.3: Detector spectral response. (a) Transmission across the detector as a function of incident frequency emitted by the Josephson radiator. Vertical dashed lines indicate at which emitter frequency the data and fits in the other three panels were taken. (b) Transmission as a function of frequency. (c) Phase as a function of frequency. (d) Real and imaginary parts of S_{21}. Q_i and f_0 were extracted by fitting to a circle in the complex plane.

sensor strip. Around ± 130 - 150 GHz, we see resonances corresponding to the resonant frequency of the detector's slot antenna. These peaks are spaced by $\sim$ 15 GHz, a multiple of the resonant frequency of the detector's CPW resonator. Simulations of the full detector geometry (including the CPW resonator) capture this beating, and similar fringes were observed in the work by C. H. Liu, *et al* [31]. Finally, around ± 230 - 250 GHz, there is a large resonance corresponding to the resonant frequency of the Josephson emitter. At these frequencies the Josephson emitter is resonantly emitting radiation, subjecting the detector to a larger incident radiation power. Following [30, 31], the radiation power emitted to free space can be calculated as

$$P_{\text{rad}} = \frac{\eta_c}{8} I_0^2 R_n \tag{6.3}$$

where η_c is the coupling efficiency of the Josephson emitter, and I_0 and R_n are the critical current and normal state resistance of the emitter Josephson junction, respectively. The Josephson emitter's efficiency is calculated from the radiation impedance simulated in CST Microwave Studio, in the same way as was done for the slot antenna (see Section 2.4). Above 8Δ the radiator will emit incoherent radiation due to shot noise, resulting in a gradual roll-off of the internal quality factor and resonant frequency of the detector [31].

For each vertical slice of the 2-dimensional dataset shown in Fig. 6.3, we fit a circle to the real and imaginary parts of S_{21} to extract the internal quality factor and resonant frequency of the detector [24, 36]. Data and fits for a few representative line cuts are shown in Fig. 6.3 (b) - (d). Repeating this for every emitter frequency, we extract the change in the resonator loss, $\delta(1/Q_i)$, and frequency shift, $\delta f/f_0$ as a function of the frequency of the incident radiation (Fig. 6.4 (c) - (d)). As was shown in Chapter 2, these quantities are related to the Mattis Bardeen expressions for the real and imaginary parts of the complex conductivity [15], and as such depend on the quasiparticle distribution in the detector's Al sensor strip. To verify that we understand the dynamics of this transmit-receive experiment, we simulate the quasiparticle dynamics using a modified Rothwarf-Taylor approach [17]. The model includes an injection rate (which depends on the modeled efficiencies of both the Josephson radiator and the detector's antenna), recombination, trapping, scattering, and thermal quasiparticle generation (negligible for the temperatures relevant to this work). The resulting quasiparticle energy distribution, $f(E)$, is used to compute the real and imaginary parts of the complex conductivity (Eq. 2.7 and Eq. 2.8), from which we compute the expected change in the internal quality factor and resonant frequency (Eq. 2.22 and Eq. 2.35, respectively).

The results of this modeling are plotted as solid lines on the data shown in Fig. 6.4 (c) - (d). We find that the model captures both the depth and bandwidth of features corresponding to the slot-antenna resonance (detector / receiver) and path antenna resonance (Josephson emitter). This particular model was calculated the radiation impedance simulated in CST Microwave Studio that did not include the detector's CPW resonator. As such the model does not capture the beating that is present in the data around the slot antenna resonance. However, the model does accurately capture these features when using the radiation impedance from simulations including the CPW resonator. Further, the Riedel anomaly [50, 51] is both present in the data (singularity just below $\pm$ 200 GHz), and is captured by the model when the singularity in the Josephson current is included [31]. This agreement between the model and data demonstrates a good understanding of

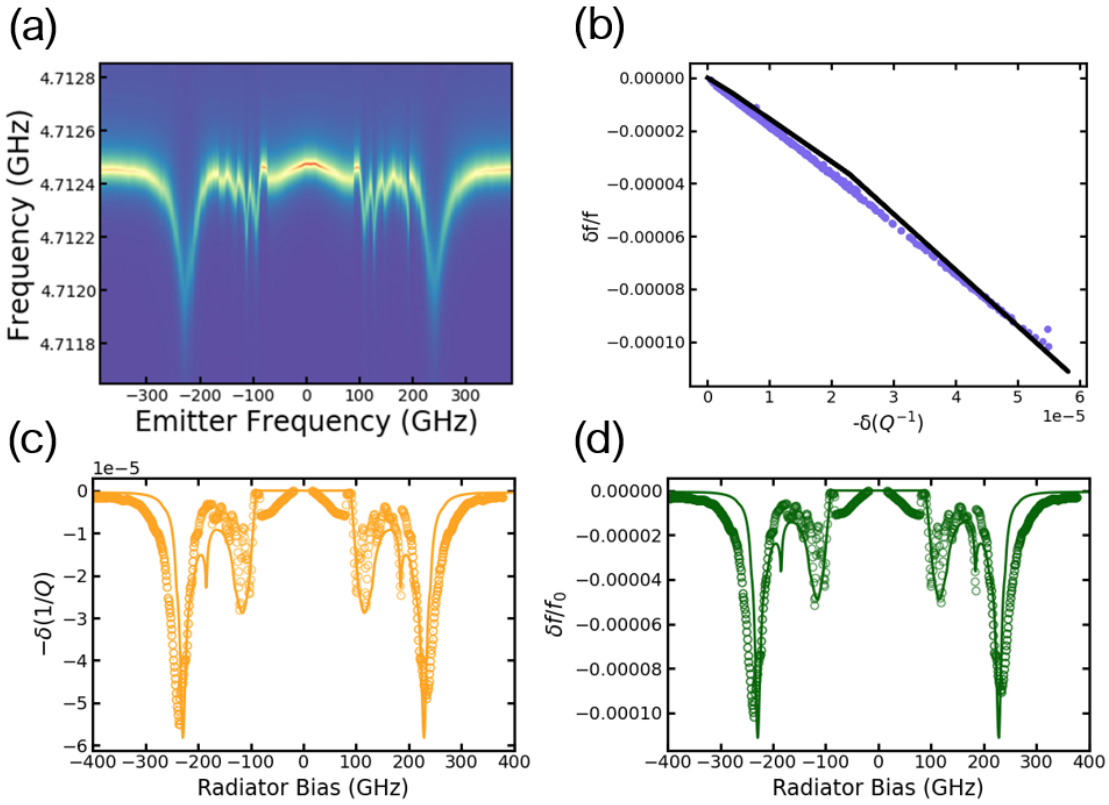

Figure 6.4: (a) Detector response as a function of Josephson emitter frequency. (b) Parametric plot of the fractional frequency shift versus resonator loss. The black line is the theoretical $\delta f/f_0$ (green circles in panel (d)) and change in $\delta(1/Q_i)$ (yellow circles in panel (c)), calculated from the Mattis Bardeen expressions using the quasiparticle energy distribution resulting from the modified Rothwarf-Taylor approach. Data is shown in purple. (c) The open circles are the resonator loss extracted from each vertical line cut of the dataset shown in panel (a). The solid yellow line is the calculated change in loss (Eq. 2.22) resulting from simulation of the quasiparticle dynamics in the transmit receive experiment. (d) The open circles are the fractional frequency shift extracted from the dataset shown in panel (a). The solid green line is the theoretical frequency shift resulting from modeling of the quasiparticle dynamics. Modeling of the quasiparticle dynamics in the detector's Al sensor strip relies on an understanding of the way in which both the Josephson emitter and the detector's slot antenna couple to radiation.

the way in which these structures emit and absorb radiation.

Finally, to demonstrate how this type of transmit receive experiment might be used to probe the distribution of quasiparticles in the detector's Al sensing volume, we parametrically plot the fractional frequency shift versus the change in loss, shown in Fig. 6.4 (b). The slope of this line will depend on the quasiparticle distribution [17, 20, 39]. Since, within this experiment we are injecting quasiparticles at a single, well-defined frequency, it should be possible to learn something about the quasiparticle dynamics in the device.

Chapter 7

Outlook on Josephson mm-wave detectors

The preceding five chapters report on the development of a novel mm-wave sensor that uses a Josephson junction for impedance matching to improve coupling to pair-breaking radiation. The detector is a variant of antenna-coupled microwave kinetic inductance detector, which gets the bulk of it's kinetic inductance from a small aluminum volume at the current anti-node of a quarter wave coplanar waveguide resonator. The antenna is implemented as a slot antenna designed to resonantly absorb radiation at 140 GHz, which is driven by a Josephson junction located at the center of the slot. Targeting a specific normal state resistance and capacitance of the junction provides a way to meet the condition of maximal power absorption, allowing for optimization of the optical efficiency, with simulated on-resonance efficiencies near unity.

To characterize the detector we evaluate detector response to a thermal quasiparticle distribution (Chapter 4), finding good agreement with theory. In Chapter 5 we expose the detector to radiation from a blackbody source, comparing the measured noise equivalent power with the theoretical expectation for a background-limited detector. We find reasonable agreement for the experimentally measured noise equivalent power derived from the cross-spectral density. However, higher observed noise levels in the amplitude and

phase spectrum indicate additional sources of noise intrinsic to the experimental apparatus. Future work with this particular apparatus will require improved shielding. Using the modeled average optical efficiency we compute the $\mathrm{NEP}_{\mathrm{dark}}$ using noise spectra measured on a nominally identical reference sample with improved shielding. This was done as a function of ambient device temperature. In doing so we found a minimum $\mathrm{NEP}_{\mathrm{dark}} = 3.6 \times 10^{-20}\mathrm{W}/\sqrt{\mathrm{Hz}}$, which is competitive for detectors designed to absorb radiation in the sub-THz range. Finally, we use a Josephson emitter to map out the frequency response of the detector in a transmit-receive experiment. We find that, using the simulated frequency-dependent efficiency, we can capture the frequency response of both the transmitter and receiver (Chapter 6).

This novel sensor retains many of the attractive features of microwave kinetic inductance detectors, including the ease of frequency multiplexing. The detector itself can be easily modified to target a range of radiation frequencies by varying the antenna design. The addition of the Josephson junction adds minimal fabrication overhead as it may be deposited in the same evaporation step as the aluminum sensing volume. Further, from simulations it is apparent that the detector efficiency is stable over a large range of junction resistances, making it a good candidate for use in large detector arrays. Hence, this novel sensor offers utility to radio astronomy. Further, the transmit-receive experiment discussed in Chapter 6 provides a unique way to probe the quasiparticle dynamics of the Josephson junction. Currently, non-equilibrium quasiparticles limit the sensitivity of pair-breaking detectors and the coherence of superconducting qubits, affecting a large range of superconductive and Josephson-based devices. New knowledge of quasiparticle dynamics could result in improvements in qubit coherence or improved sensitivity of detectors.

Part II

Toward implementation of a protected charge-parity qubit

Chapter 8

Protection at the hardware level

Superconducting qubits rely on fragile quantum states to store information and perform computations. In it's most general form, this state can be written as $|\psi\rangle = \alpha|0\rangle + \beta|1\rangle$, and can be conveniently visualized using the Bloch sphere (Fig. 8.1 (a)). The Bloch sphere is a unit sphere, with state $|0\rangle$ at the north pole and $|1\rangle$ at the south pole. A pure state ($|\alpha|^2 + |\beta|^2 = 1$) would then be a vector from the center of the sphere to any point on the surface. Rewriting this state in terms of the polar (θ) and azimuthal (ϕ) angles that describe this unit vector, we find $|\psi\rangle = \cos(\theta/2)|0\rangle + e^{i\phi}\sin(\theta/2)|1\rangle$. The fragility of this state is described by the coherence time (or two, rather). T_1 describes relaxation from the excited state, $|1\rangle$, to the ground state, $|0\rangle$, or alternately excitation out of the ground state. T_2 describes drift in the phase of the quantum state. In the most naive sense one could quantify the performance of a quantum computer in terms of the number of computations possible before coherence is lost. We see immediately that a functional quantum computer requires long coherence times (both T_1 and T_2), as well as comparatively short gate times.

Superconducting qubits, fortunately, offer both fast (nanosecond) gate times the promise that long coherence times may be engineered. Already, exponential progress has been made since the first demonstration of quantum coherence in a superconducting qubit by Nakamura *et al* in 1999 [52] with large-qubit count processors achieving coherence times

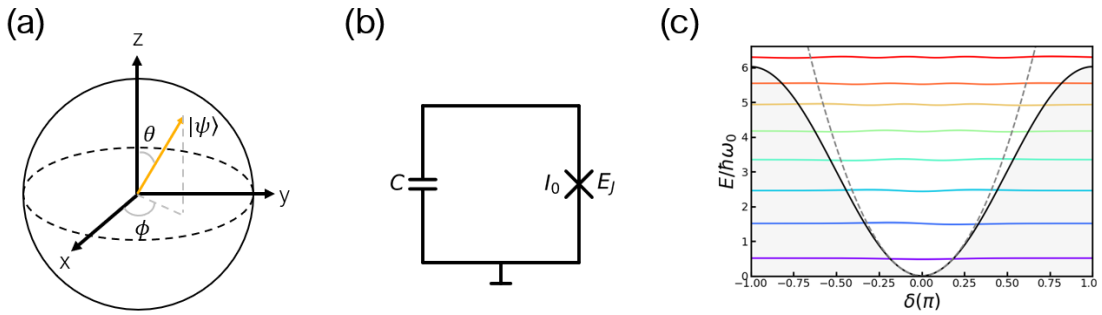

Figure 8.1: Superconducting circuits for quantum computation. (a) The Bloch sphere. (b) Circuit representation of a transmon qubit. (c) The transmon has a $\cos\delta$ potential, where δ is the phase across the Josephson junction. The energy eigenstates are plotted on top of the potential, offset vertically by the eigenenergies. The hyperbolic potential of an LC oscillator (where the inductance is the Josephson inductance) is indicated by the dotted grey line showing that when considering the lowest energy states, the transmon may be well approximated by the harmonic oscillator.

of order 100 μs [53, 54]. While such quick progress would not have been possible without advancements in fabrication , packaging, and an improved understanding of the dominant loss mechanisms affecting superconducting qubits, the success and ubiquity of the transmon is due, at least in part, to the fact that it offers protection against phase errors at the hardware level [5]. For the purposes of this thesis, we define '*protection*' as exponential insensitivity to both bit-flip and phase errors. The transmon consists of a Josephson junction or SQUID, with energy E_J, shunted by a capacitance (Fig. 8.1), with charging energy E_C. For the right choice of ratio between E_J and E_C, the transmon can be made to be exponentially insensitive to charge-noise [5]. It will be insensitive to phase errors, however this circuit will still be susceptible to other sources of local noise and decoherence such as TLS losses, flux noise, quasiparticle poisoning, among others. As such, we can think of the transmon as a half-protected qubit which will necessitate some form of quantum error correction. Popular error correcting protocols, such as the surface codes [55], rely on large arrays of data and ancilla qubits to uniquely identify and correct errors. It is estimated that for state of the art coherence times and gate fidelities one would need close to a million physical qubits to build a useful error-corrected quantum computer with such a protocol [55]. This presents a formidable engineering challenge. There would be a

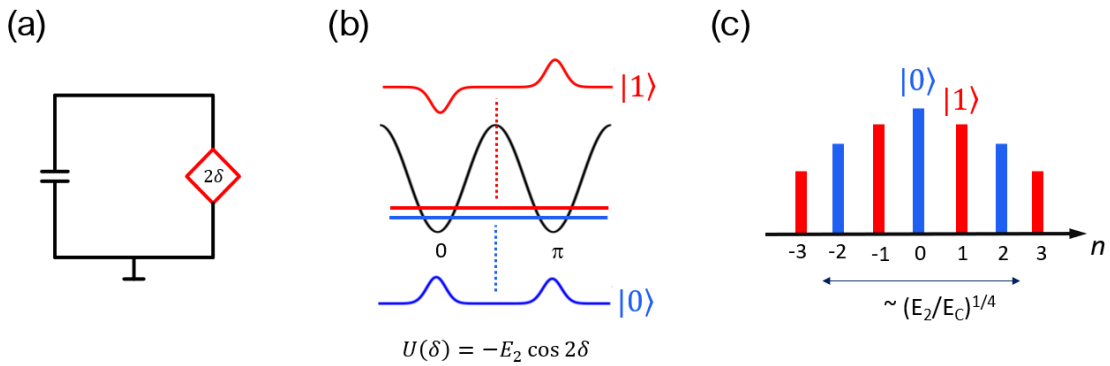

Figure 8.2: The $0-\pi$ qubit. (a) Circuit representation of the $0-\pi$ qubit, which consists of a π-periodic Josephson element shunted by a capacitor. (b) Phase basis representation of the $0-\pi$ qubit. In the phase basis, the potential is proportional to a double-well potential with local minima at 0 and π.

massive hardware overhead associated with biasing and reading out the qubits. Cooling and heat sinking of supporting microwave components presents a challenge as the space on the cold plate of a dilution refrigerator is limited. An alternate approach would be to engineer a new type of qubit which is protected from local noise and decoherence – both bit flip and phase errors.

The $0-\pi$ qubit[1] is one such implementation of a protected qubit consisting of a π-periodic Josephson element shunted by a capacitance (Fig. 8.2 (a)). It has been shown that a qubit made with such a π-periodic element would be a fully-protected qubit [56]. In the phase basis the potential is proportional to $\cos(2\delta)$, shown in Fig. 8.2 (b), so we have a double-well potential with local minima at 0 and π. The two lowest lying energy states are near degenerate representations of symmetric and anti symmetric wavefunctions localized in the 0 and π wells. This near degeneracy is critical for achieving protection. In the charge basis (Fig. 8.2 (c)) these states map to superpositions of even or odd numbers of Cooper pairs, and as such are highly de-localized and intertwined. Hence, any environmental fluctuations will affect these states in a similar way – this is critical for achieving protection.

Since it's proposal in 2001 there have been steady progress towards the development

[1]The implementation of the $0-\pi$ qubit pursed by our collaboration is formally called the charge-parity or C-parity qubit.

of a $0-\pi$ qubit, including a number of circuit implementations. The work in this thesis builds upon the Josephson rhombus chain work pursued by Ioffe and Gershenson [57]. An alternate implementation of the $0-\pi$ qubit has been pursed by Koch, Schuster and Houck [58, 59]. An alternate circuit implementation called the $\cos(2\phi)$ qubit[2] was proposed in 2020 [60]. Each implementation comes with its own unique challenges, be they difficult to implement circuit parameters, parasitic modes that provide unwanted coupling to the environment, or myriad control lines. The challenges associated with developing and controlling these exotic qubits lend merit to the relative simplicity of the transmon[3].

In the remainder of this Chapter we try to elucidate the origins of protection in such a device. In order to do so, we first need to discuss the construction of a composite π-periodic Josephson element.

8.1 Engineering a π-periodic Josephson element

The composite Josephson element studied in this thesis consists of two Josephson junctions and two inductances which form a loop through which an externally applied flux, Φ_{ext} may be threaded (Fig. 8.3 (a)) [63]. We can write down an expression for the two-dimensional potential of this element using flux-quantization [3]

$$U(\delta_1, \delta_2) = -\frac{I_0\Phi_0}{2\pi}(\cos\delta_1 + \cos\delta_2) + \frac{1}{4L}\left(\Phi_{\text{ext}} - \frac{\Phi_0}{2\pi}\delta_{\text{dm}}\right)^2 \tag{8.1}$$

where δ_1 and δ_2 are the phase across each of the two Josephson junctions. We assume zero asymmetry, that is, both inductors have inductance, L and both junctions have critical current, I_0. Rewriting this expression in terms of the common mode and differential-mode phases

$$\delta_{\text{cm}} = \frac{\delta_1 + \delta_2}{2} \quad \text{and} \quad \delta_{\text{dm}} = \frac{\delta_2 - \delta_1}{2} \tag{8.2}$$

[2] In this case, ϕ represents the phase across the junction, which we call δ.

[3] Although not strictly relevant to the scope of this thesis, I would be remiss not to mention the increasingly popular fluxonium qubit [7]. In recent years, long relaxation times have been demonstrated in capacitively shunted variant called the 'heavy fluxonium' [61], prompting the development of comparatively fast flux-based gates [62]. While the fluxonium exhibits surface-level similarities to the $0-\pi$ qubit (for instance, the double-well potential), it does not allow for topological protection.

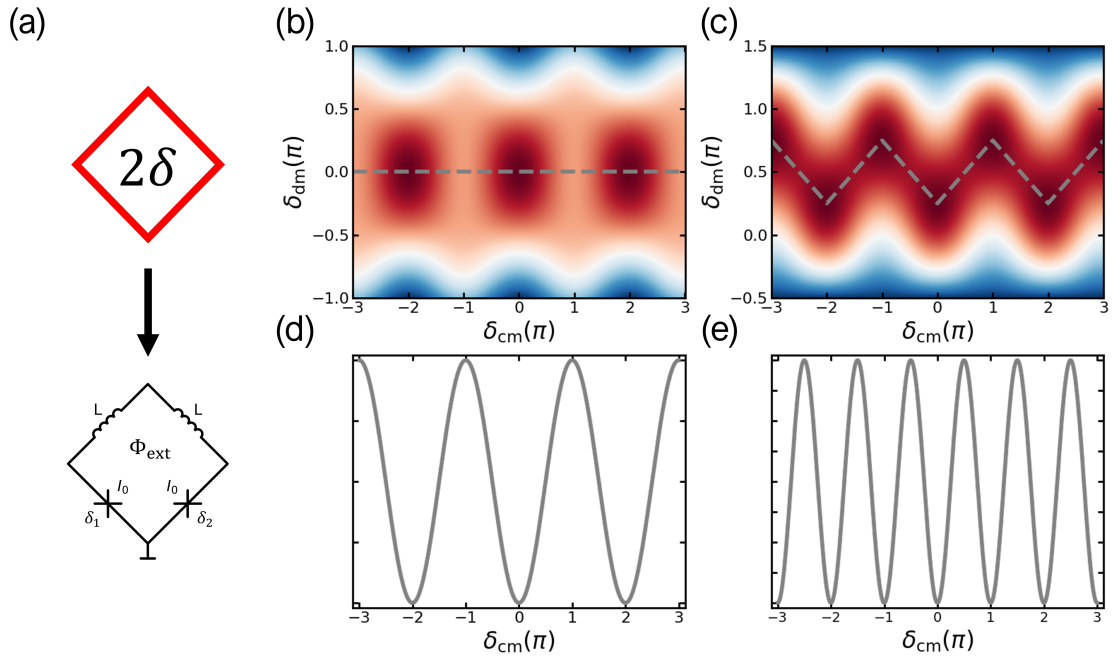

Figure 8.3: A composite Josephson element capable of tuning between 2π and π-periodic regimes. (a) Circuit representation of a π-periodic Josephson element called a plaquette. Each plaquette consists of two inductors and two Josephson junctions arranged in a superconducting loop, through which an externally applied flux, Φ_{ext}, may be threaded. (b) The potential, rewritten in terms of the common-mode, $\delta_{\text{cm}} = (\delta_1 + \delta_2)/2$, and differential-mode, $\delta_{\text{dm}} = (\delta_2 - \delta_1)/2$ phases. For zero externally applied flux, $\Phi_{\text{ext}} = 0$, there are three local minima, separated by $\delta_{\text{cm}} = 2\pi$. (c) When biased at half a flux quantum, $\Phi_{\text{ext}} - \Phi_0/2$, we find a doubling of the number of local minima. (d) Taking the trajectory connecting local minima in sub-figure (b), we see that the plaquette will be 2π-periodic for zero externally applied flux. (e) Again taking the trajectory connecting adjacent local minimal we see that for half-flux quantum bias points the composite Josephson element will be π-periodic.

we plot the resulting potential in Fig. 8.3(b) for zero externally applied flux, and in Fig. 8.3(c) for $\Phi_{\text{ext}} = \frac{\Phi_0}{2}$.

Immediately we see that for the case of zero externally applied flux, there are three local minima and that we have a doubling of the number of local minima when biased at half a flux quantum[4]. For each of these plots we may take the trajectory between adjacent local minima. Plotting the value of the two-dimensional potential as a function of the common-mode phase across the composite element (Fig. 8.3 (d)), we clearly see that the element is 2π-periodic when biased at integer flux quantum. In this case, where we are nulling any externally applied flux, the plaquette will behave as a normal Josephson junction. Moving through the same analysis for the case of $\Phi_{\text{ext}} = \frac{\Phi_2}{0}$, we see that the element will be π-periodic when biased at half-integer flux offsets. When biased at half a flux quantum, the first harmonic of the Josephson energy (which is proportional to $\cos\delta$) is suppressed, and the second harmonic (proportional to the $\cos(2\delta)$ remains. So we will have a π-periodic Josephson element when biased at half a flux quantum. Having demonstrated how one might engineer a π-periodic Josephson element, we may now discuss the origins of protection in a circuit constructed from these elements.

8.2 Protection against bit-flip errors

Recall that a circuit made with a π-periodic Josephson element aspires to protection from both bit-flip and phase-flip errors [56]. We begin by discussing protection against bit-flip errors as it is more intuitive and we may employ the same strategy that has seen success in fluxonium qubits [61]. Operation of this device as a protected qubit requires that we capactively shunt the plaquette. The Hamiltonian describing the full circuit (Fig. 8.2 (a)) is then

$$H = \frac{n_g^2}{2C} - E_2\cos(2\delta) = \frac{n_g^2}{2C} - U(\delta) \tag{8.3}$$

where n_g described the charge on the island, C is the shunt capacitance, and E_2 is the amplitude of the second harmonic of the Josephson energy, which sets the barrier height of

[4]Henceforth referred to interchangeably as half a flux quantum, $\Phi_0/2$, or frustration.

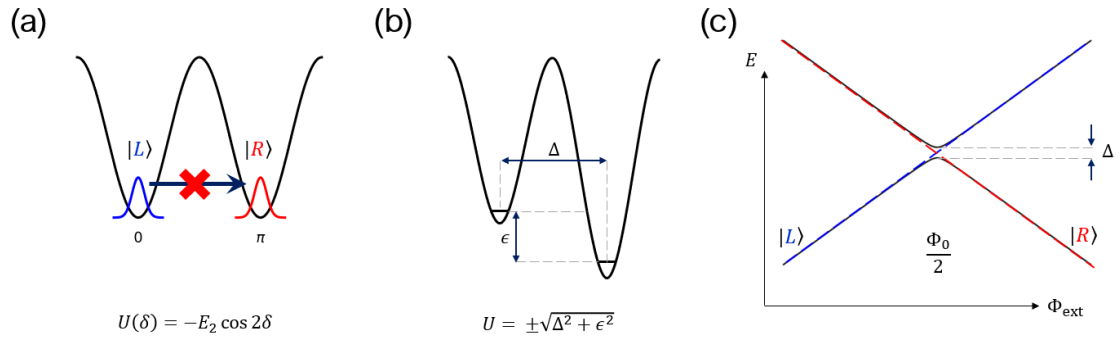

Figure 8.4: Protection against bit-flip and phase errors. (a) Protection against bit flip errors in the charge-parity qubit is achieved with the use of a capacitive shunt. The addition of a large capacitance forces computational ground states to be localized deep in the wells, exponentially suppressing tunneling between states localized in the left and right wells. (b) Phase errors in this qubit are due to imperfections in the π-element, and as such they are due to flux noise. De-tuning away from $\Phi_{\text{ext}} = \Phi_0/2$, a mechanism via which we can have evolution from one computational state to the other is introduced.(c) The computational states will be localized in the left and right wells. Tunneling between states in the left and right wells will be described by two hyperbolic bands separated by an energy gap, Δ

the double well potential[5]. Noting that the shunt capacitance is analogous to mass in this system, and applying the WKB approximation [64] we see that the capacitance will appear in the exponential and further that increasing the capacitance will exponentially suppress tunneling between the two wells. Hence protection against bit-flip errors is achieved via the exponential suppression of tunneling errors[6].

8.3 Protection against phase-flip errors

A qubit made from a capacitvely shunted π-periodic Josephson element to be insensitive to phase errors as well as bit-flip errors. Physically, phase errors in this system will be due to imperfections in the π-elements. For a perfectly symmetric plaquette biased at half a flux quantum, there will be no evolution between states localized in the two wells.

[5]Note that here we are using the one-dimensional $\cos(2\delta)$ potential for a π-periodic Josephson element, not the two-dimensional potential discussed in the previous Section. This argument extends beyond our particular implementation of the π-periodic element.

[6]Extending this argument we see that physically, bit-flip errors in this system can be attributed to charge noise.

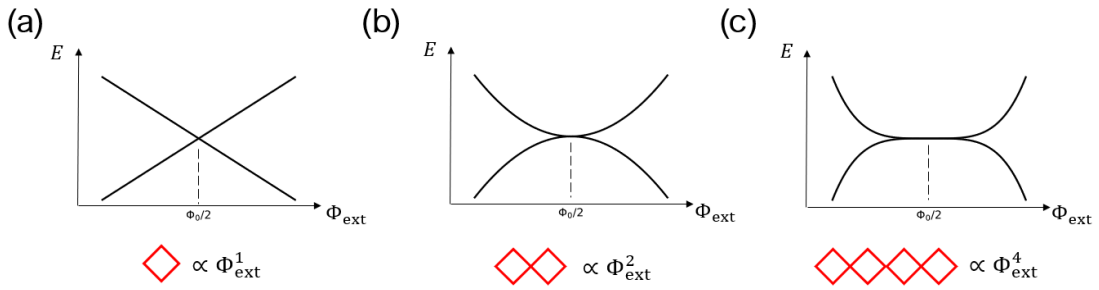

Figure 8.5: Exponential insensitivity to flux noise via concatenation. (a) For a device made with a single plaquette we expect to be very sensitive to flux noise because of the linear flux dispersion. (b) For a two-plaquette system we expect a quadratic flux dispersion when simultaneously biasing both plaquettes to half a flux quantum. (c) The flux dispersion is expected to continue to scale exponentially, with a four-plaquette system having a quartic flux dispersion around frustration. By concatenating we soften the flux dispersion around $\Phi_0/2$, becoming exponentially insensitive to flux noise, hence achieving protection against phase errors.

However, a mechanism for evolution between these states may be introduced if there is some asymmetry in the π-element or if the external flux is de-tuned from half a flux quantum, $\Phi_{\text{ext}} = \frac{\Phi_0}{2} + \delta\Phi$. Hence, due to the construction of our π-element, phase errors will be due to flux noise. Tunneling between the left and right wells will be described by two hyperbolic bands (Fig. 8.4 (c)) separated by an energy gap, Δ. Let us define an asymmetry energy, ϵ, adding in quadrature with Δ.

For a single plaquette system, the splitting between states localized in the left and right wells will be very small due to shunting with a large capacitance, however the flux dispersion will be linear (Fig. 8.5 (a)) making the device very sensitive to flux noise. As such, we expect to have essentially no protection against phase errors in a single plaquette device. However, exponential insensitivity to flux noise may be achieved through concatenation of multiple π elements. For a two plaquette system, when biasing the plaquettes simultaneously to half a flux quantum (double-frustration), we expect the flux dispersion along this trajectory through this two-dimensional flux space to be quadratic. Similarly, although harder to visualize, a device with four plaquettes brought simultaneously to frustration would have a flux dispersion that is quartic. By concatenating additional plaquettes we are able flatten the energy bands around the $\Phi_0/2$ operating point. Since this scales 'expo-

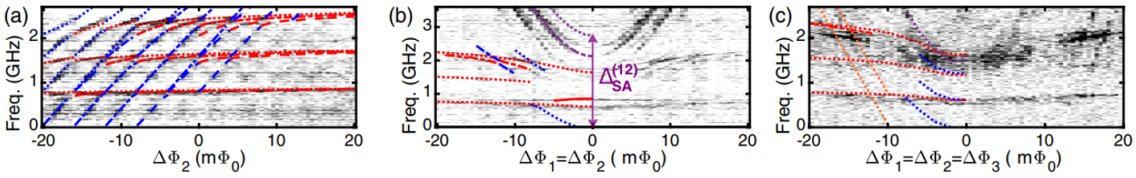

Figure 8.6: Qubit spectroscopy of a three-plaquette device. Reproduced from K. Dodge and Y. Liu *et al*, 2023 [63]. (a) Qubit spectroscopy of a three-plaquette device around single-frustration (biasing one plaquette through a small range of fluxes centered around $\Phi_0/2$). This is done while explicitly nulling the flux through the other two plaquettes. The authors identify intra-well transitions (plasmons) in red and inter-well transitions (fluxons) in blue. They extract device energy scales and asymmetry from fits to the qubit spectroscopy. (b) Qubit spectroscopy around double-frustration ($\Phi_1 = \Phi_2 = \Phi_0/2$), where Φ_1 is the externally applied flux in the first plaquette, and Φ_2 is the externally applied flux in the second. Again, fits to the spectroscopy are used to identify plasmons and fluxons. An unwanted transition out of the computational basis is also identified (shown in purple). (c) Spectroscopy around triple-frustration ($\Phi_1 = \Phi_2 = \Phi_3 = \Phi_0/2$). Comparing the spectroscopy through single, double, and triple-frustration we can see the flattening of the fluxon transitions (blue).

nentially' with the number of plaquettes, it is via concatenation that we achieve protection against phase errors.

This exponential softening of the energy bands was verified experimentally [63]; a detailed description of these experiments can be found in the theses of Kenneth Dodge [65] and Yebin Liu [66]. Details and shortcomings of this design will be discussed briefly here, however, the focus of this thesis is primarily on the subsequent generation of plaquette devices. Working with a three-plaquette device, similar to that described in this thesis, Dodge and Liu *et al* take extensive spectroscopy data around single, double, and triple-frustration ($\Phi_1 = \Phi_0/2$, $\Phi_1 = \Phi_2 = \Phi_0/2$, and $\Phi_1 = \Phi_2 = \Phi_3 = \Phi_0/2$, respectively). A partial figure from the paper is reproduced in Fig. 8.6. They measure the transition frequencies at each flux point, fitting to extract device parameters. From simulations using device parameters extracted from fits they show the exponential dependence of the flux dispersion on the number of plaquettes (Fig. 8.7).

This attempt at implementing a protected-charge parity qubit was limited by excitations out of the computational ground state, making time domaine characterization of the device difficult. This was thought to be in part due to enhanced radiative coupling to the

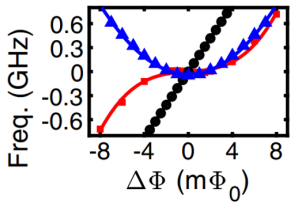

Figure 8.7: Exponential dependence of flux dispersion on the number of plaquettes. (Reproduced from [63].) Using parameters extracted from fits to spectroscopy, Dodge and Liu *et al* show the exponential dependence of the flux dispersion on the number of plaquettes, demonstrating decreased sensitivity to flux noise.

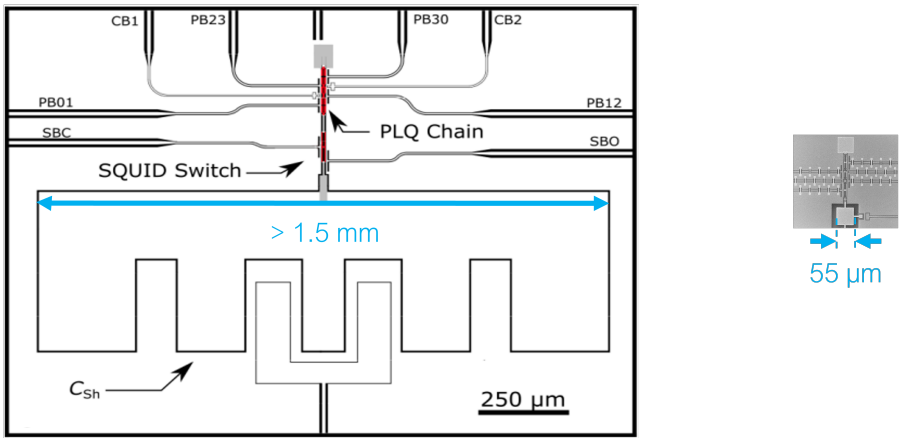

Figure 8.8: Comparison of physical device scale for devices studied in Dodge and Liu *et al* and those studied in this thesis. On the left is the design file for the device studied in [63]. The inter-digital planar capacitor is of mm-scale, aiding radiative coupling to the environment and making initialization into the computational ground state a challenge. Future design iterations, described in this thesis, aim to avoid this by moving to a planar capacitor for the capacitive shunt. A scanning electron micrograph of one of these devices is shown on the right. The overlap capacitor is 55 μm per side, an orders of magnitude reduction device in size. Devices shown in this figure are roughly to scale.

environment [63], a result of the massive planar capacitor used in this design (Fig. 8.8). It has been shown [30, 31] that superconducting qubits can be thought of as aperture antennas, where typical Josephson junction parameters provide a reasonable conjugate match to free space allowing for the resonant absorption of pair-breaking radiation. Future designs, investigated in this thesis attempt to mitigate these effects by replacing the mm-scale planar capacitor with a parallel plate capacitor. In the remaining chapters of this thesis we discuss development, design, control, and characterization of such devices.

Chapter 9

Plaquette: A composite Josephson π-periodic element

Having discussed the origins of protection in plaquette-based devices we move to the physical implementation and verifcation of such elements. We begin by discussing details of the fabrication of the π-elements, before moving on to a set of experiments integrating these π-elements into an RF SQUID, demonstrating the ability to tune between 2π-periodic and π-periodic regimes.

9.1 Engineering a composite π-periodic Josephson element

As introduced in Chapter 8, our implementation of a π-periodic Josephson element, the plaquette, consists of two inductors and two Josephson junctions, arranged in a superconducting loop through which an externally applied flux may be threaded (Fig. 8.3 (a)). To achieve suppression of the first harmonic of the Josephson energy when biased at half a flux quantum, we require that the Josephson energy,

$$E_J = \frac{I_0 \Phi_0}{2\pi} \tag{9.1}$$

and the inductive energy,

$$E_L = \left(\frac{\Phi_0}{2\pi}\frac{1}{L}\right)^2 \tag{9.2}$$

be approximately matched. In these experiments we target $E_J/k_B \approx E_L/k_B \approx 1-2$ K, which corresponds to a junction critical current of order 100 nA and a linear inductance of order 1-10 nH. Working with imperfect π-elements and aspiring to protection through concatenation we are able to target energy scales readily available with existing fabrication techniques[1].

Josephson junctions are fabricated using standard Al-AlOx-Al junction processing, and are deposited via double-angle evaporation. See Appendix B.1 for a detailed discussion of the geometry involved. Recall that asymmetry in the π-element will contribute to insufficient suppression of the first harmonic of the Josephson energy at frustration. The dominant source of asymmetry in the plaquette will be due to variations in the Josephson energy of these smaller Josephson junctions. Contributing factors to junction asymmetry include variations due to the size of Al granules comprising the junction and variations in the lithographically designed junction area. Numerous attempts were made to mitigate variation in E_J, including the use of proximity effect correction during electron-beam lithography and cold development of the resist post-exposure. Room temperature resistance spreads (reported in Fig. 9.1 (d) and (e)) can be used to quantify plaquette asymmetry prior to cooldown. It is expected that plaquette asymmetry of 2-5% will be required to successfully realize a qubit with these π-elements [63].

Inductors are implemented as arrays of large area Josephson junctions, as was first done in fluxonium qubits [7]. Working with large-area Josephson junctions, the nonlinearity of the inductance is suppressed making it possible to realize a linear inductor in a superconducting circuit. An alternate approach, which was investigated early on in this collaboration and has successfully been implemented in fluxonium circuits [67, 68] is to use a high-kinetic inductance material such as superconducting nitrides (NbN, TiN, NbTiN,

[1] Other implementations of the $0-\pi$ qubit require microHenry inductances as well as minimal stray capacitance to ground (of order 10 fF), making them incredibly challenging to realize with existing fabrication techniques [58, 59]

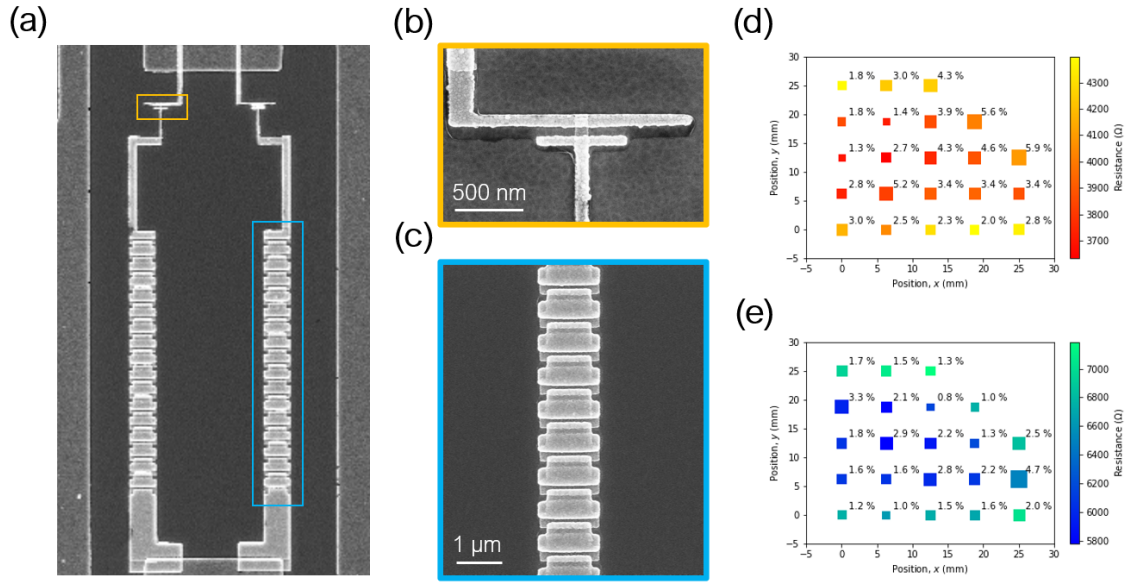

Figure 9.1: (a) Scanning electron micrograph of a plaquette. A small-area junction is indicated by the orange box, and an inductor is indicated in blue. (b) Small-area junction with designed area 100 nm × 100 nm. (b) Linear inductors in the plaquette were implemented as arrays of large-area Josephson junctions, such as this. Junction chains consisted of 17 Josephson junctions, with nominal area 1 μm × 180 nm. (d) Junction resistance spreads and mean resistances for small area junctions across a quarter of a three-inch wafer. The position of the die is indicated on the x and y axes. The percentage indicates one standard deviation in room temperature resistance of test junctions on that die, of which there are six. Marker size is also proportional to this value. The color, cross-reference to the colorbar indicates the mean junction resistance. (e) Junction resistance spreads and mean resistances for arrays of large-area junctions across the same quarter wafer. The leftmost dies in the top two rows were cooled for measurement, the data on which is reported in the remainder of this thesis.

etc.) or granular aluminum[2]. In particular, nanowires fabricated from titanium nitride via atomic layer deposition have demonstrated sheet inductances up to 234 pH/□ and have been used to make resonators with internal quality factors ranging between 1×10^5 and 1×10^6 at single-photon powers [69]. While highly uniform, high-quality films such as this may help to decrease asymmetry between plaquettes (for instance due to variations in yield in the junction arrays), we ultimately opted to pursue Josephson arrays for the inductors as they allowed for reduced fabrication complexity.

Finally, it is critical that we have local flux control of each plaquette. This is achieved with on-chip bias lines, which will be discussed further in the context of device layout and control in Chapter 11.

9.2 Demonstration of π-periodicity

To verify that we can sufficiently suppress the first harmonic of the Josephson energy we integrate the plaquette into an RF SQUID an demonstrate tuning between the 2π and π-periodic regimes. An RF SQUID is the parallel combination of a capacitor, inductor, and a Josephson junction[3] in parallel to ground. The circuit diagram is shown in Fig. 9.2 (a). In a conventional RF SQUID, the inductor and Josephson junction form a superconducting loop which may be biased by an externally applied flux, Φ_{ext}. In the plaquette resonator, the Josephson junction is replaced by plaquette (Fig. 9.2 (b)), giving us two flux knobs to turn. By fixing the flux through the plaquette loop, and looking at the plaquette resonator frequency as a function of the RF SQUID flux, Φ_{ext}, we can verify that we are able to access the π-periodic regime. The plaquette resonator response is shown in Fig. 9 (c) for $\Phi_{\text{plq}} = 0$ (bottom plot) and $\Phi_{\text{plq}} = \Phi_0/2$ (top plot).

[2]Sometimes called 'dirty' aluminum

[3]Possibly, a SQUID, two junctions in parallel to form a superconducting loop which similar to the plaquette may be biased by an externally applied flux.

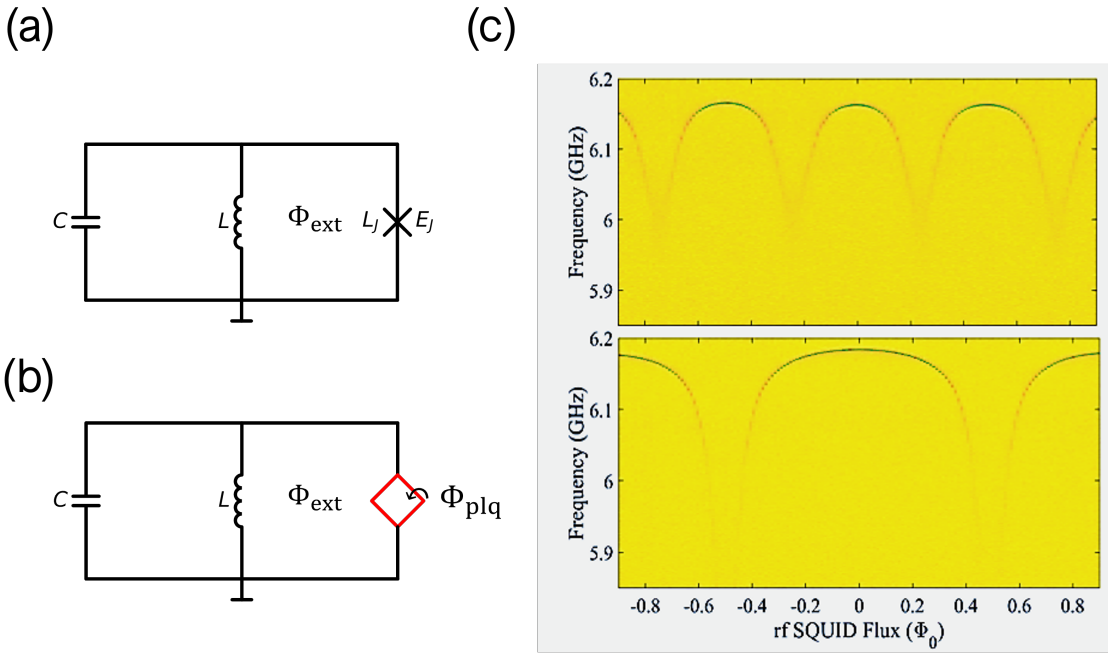

Figure 9.2: The performance of the π-element was verified by integrating the plaquette into an RF SQUID, a so called 'plaquette resonator'. (a) Circuit diagram for the conventional RF SQUID consisting of a capacitor, inductor, and Josephson junction in parallel. The inductor and junction form a loop which may be biased by an externally applied flux, Φ_{ext}. (b) Circuit representation of the plaquette resonator. The plaquette (c) replaces the Josephson junction in the conventional RF SQUID. In addition to the RF SQUID bias, Φ_{ext}, the plaquette may be locally flux biased by modulating Φ_{plq}. (c) Plaquette resonator data taken by K. Dodge and Y. Liu in the Plourde lab at Syracuse University [65]. Plaquette resonator frequency is shown as a function of the RF SQUID flux, Φ_{ext}. In the bottom plot $\Phi_{\text{plq}} = 0$, and for the top $\Phi_{\text{plq}} = \Phi_0/2$. There is a clear halving of the period in the top plot, clearly demonstrating the ability to tune between the π and 2π periodic regimes.

Chapter 10

Design and control of multi-plaquette devices

In this Chapter we discuss design and control of devices with up to three plaquettes, giving details of the most recent device layout and device fabrication. We then discuss control of multi-plaquette devices and, in particular, the extraction of mutual inductances from cavity spectroscopy data, allowing for compensation of unwanted flux crosstalk.

10.1 Design, layout and fabrication

Each chip (Fig. 10.1) consists of a multi-plaquette device, capacitvely coupled to a CPW resonator, a plaquette resonator (see previous Section for details), and a lumped element resonator all coupled to a shared transmission line. With this chip design we aim to independently verify the performance of each circuit element in the multi-plaquette device.

The lumped element resonator, consisting of a parallel plate capacitor and a spiral inductor allows for independent testing of the parallel plate capacitor used in the multi-plaquette device. The resonator is capacitvely coupled to the central feedline via a parallel plate capacitor. This resonator allows us to rule-out the possibility of pin-hole shorts through the dielectric. From the resonant frequency of this lumped element resonator we may extract a capacitance per square micron for the parallel plate capacitor, which we can

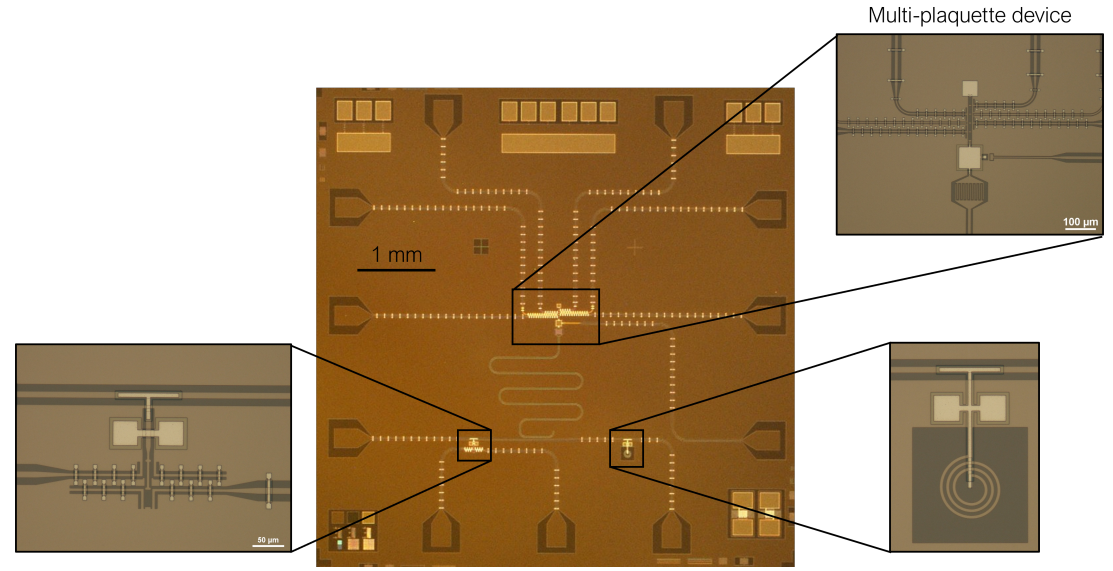

Figure 10.1: Optical micrograph showing the multi-plaquette chip. In the center of the chip is the multi-plaquette device, supporting up to three-plaquettes, shunted by a parallel plate capacitor, and capacitively coupled to a quarter-wave coplanar waveguide resonator for dispersive readout. On the shared transmission line there is a plaquette resonator (lower left) to verify the π-periodicity of the plaquettes *in situ*, and similarly, a linear, lumped element resonator to test the parallel plate capacitor. Crossovers are used to control ground currents around the device. Twelve junction test structures are located at the top of the chip, six to test the large-area junction arrays and six small-area witness junctions. Structures to test step coverage and integrity of the dielectric used in the crossovers are located in the bottom right corner of the chip. The ground plane, transmission line, and control lines are Nb on high resistivity silicon. Evaporated silicon dioxide is used for the dielectric in the crossovers and parallel plate capacitor, with an Al counter-electrode. Note that optical images were taken prior to electron beam lithography. As a result, the Josephson junctions had not yet been deposited at the time these photos were taken.

then use for modeling of the multi-plaquette device. Finally, fitting to a circle in IQ space, we may extract the internal quality factor of the resonator, which will be dominated by losses from the SiO_2 in the parallel plate capacitor. This is useful to know as this will also be the dominant source of loss in the multi-plaquette device.

The inclusion of the plaquette resonator on-chip allows us to verify that we can sufficiently suppress the first harmonic of the Josephson energy. This confirms that we do in fact have a π-periodic element. The RF SQUID inductors in this case are implemented as arrays of large-area Josephson junctions, identical to those used in the plaquettes. We opt for a gradiometric design, where the RF SQUID inductance is two inductors in parallel to ground. This allows for symmetric biasing and capacitance to ground. The parallel plate capacitor is identical to that used in the lumped element resonator. Local flux lines allow for independent modulation of the flux through the plaquette, and the RF SQUID loop.

The multi-plaquette device is located in the center of the chip, and is controlled using four flux bias lines and one global charge gate, and two local charge gates. Further details regarding biasing and control will be given in the subsequent Section. Scanning electron micrographs of the multi-plaquette device are provided in Fig. 10.2. The device supports up-to three plaquettes. The number of plaquettes is chosen in electron beam lithography. In addition, there are 'dummy' plaquettes at the bottom and top of the chain. This is to ensure symmetric capacitance to ground for each of the 'real' plaquettes in the chain. At the bottom of the scaning electron micrograph in Fig. 10.2 (a), the parallel plate capacitor, along with the global charge gate are visible. Just out of picture, but visible in the inset of Fig. 10.1, the shunt capacitor was capacitvely coupled to a quarter wave CPW resonator via an interdigital capacitor. This quarter wave resonator was then inductively coupled to the central feedline, and was used for dispersive measurement.

Devices were fabricated on high resistivity Si(001). Base layers could be either Nb or Al deposited via RF sputtering. An HF etch immediately prior to deposition was used for removal of the native oxide. The base layers were patterned via optical lithography using a Nikon i-Line stepper. In the case of Al base layers, the base layer was etched

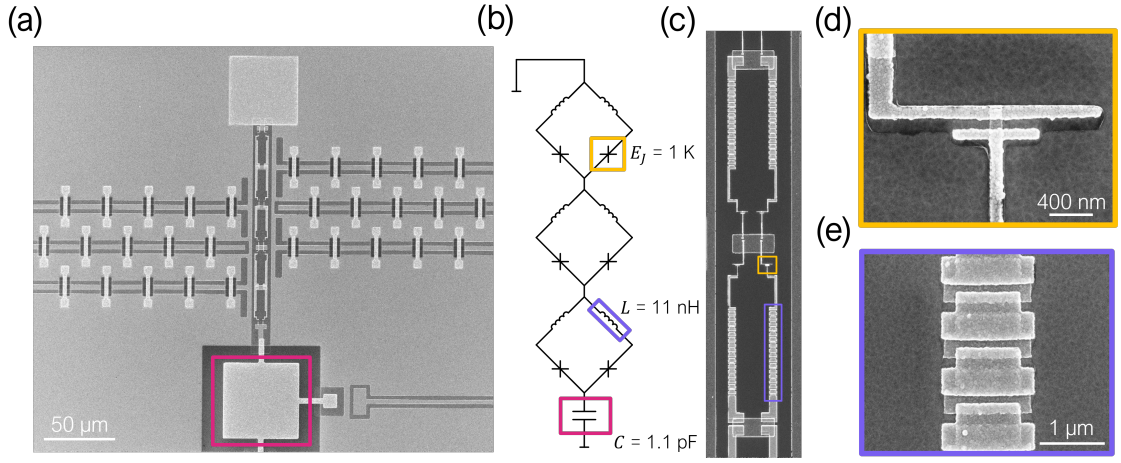

Figure 10.2: Details of the multi-plaquette structure. (a) Scanning electron micrograph showing the multi-plaquette structure, supporting up to three plaquettes, defined during electron beam lithography. Plaquettes are numbered from bottom to top, with the bottom-most and top-most plaquettes being 'dummy' plaquettes (with junctions shorted in lithography), included to ensure symmetric capacitance to ground. At the bottom of the image is the shunt capacitor to ground (magenta square) implemented as a parallel plate capacitor. At the top of the chain is an Al patch, used for gap engineering. SiO_2-Al crossovers ensure good microwave hygiene around the bias lines (further description of the bias lines may be found in Fig. 10.5. (b) Circuit representation of a three plaquette device ('dummy' plaquettes are not shown). (c) Scanning electron micrograph of two plaquettes, showing the locations of the small area junctions (yellow) and large-area junction arrays (purple). Micrographs of which are shown in sub-figures (d) and (e), respectively.

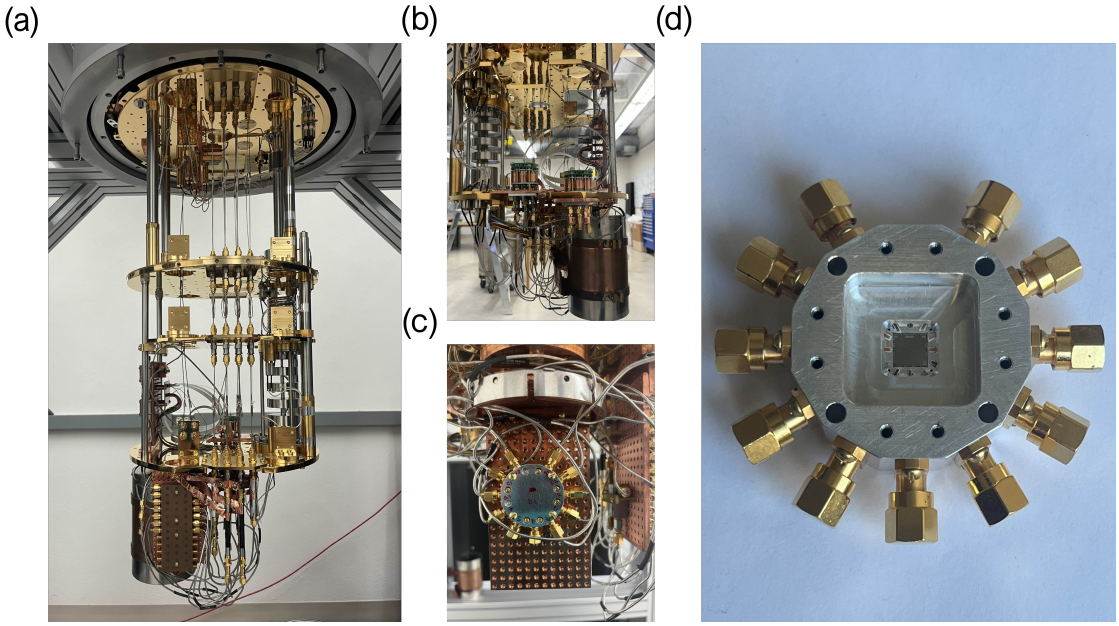

Figure 10.3: Cryogenic measurement apparatus. (a) Devices were cooled in a bluefors cryogen-free dilution refrigerator. (b) Microwave relays, thermalized to the cryostat's mixing plate were used to increase measurement throughput. Devices were shielded in a Cryoperm (μ-metal) can, coated on the inside with a mixture of SiC grains, carbon black, and Stycast. (c) Inside the Cryoperm can, samples, housed in an Al enclosure, were mounted to a copper drop-down plate. Non-magnectic SMA cables were used inside the can to transfer control pulses to the device. (d) The twelve-sided Al sample enclosure. surface-mount SMA connectors, soldered to copper on Rogers board launchers were used to transfer measurement and control signals into the sample enclosure. Al wirebonds were used to transfer signals from the printed circuit board launchers to on-chip transmission and control lines.

during development in the developer (1-3% aqueous TMAH solution). In the case of Nb base layers, features were defined via a Cl-based inductively coupled plasma etch. Subsequent to base layer definition, resist was removed in NMP before a second round of optical lithography to define areas where SiO_2 would be deposited for the crossovers and parallel plate capacitors. Since deposition of the dielectric is done via a liftoff process, an image reversal resist was used, requiring an additional flood exposure (done with a Karl Suss MA6 mask aligner) post exposure with the Nikon stepper. SiO_2 was deposited via electron beam evaporation, and lifted off in NMP heated to 80 C. A final layer of optical lithography was used to define the top electrode for the crossovers and parallel plate capacitor. This was again done with an image reversal resist. Post-lithography, Al was deposited via electron beam evaporation and again lifted off in hot NMP. Subsequent to optical lithography, electron beam lithography was used to define the Josephson junctions and inductors. Fabrication of the Josephson junctions relied on a resist bi-layer (PMMA 950 A3 atop MMA 8.5 EL11). Further details of the junction fabrication can be found in Appendix B.1. Josephson junctions were deposited via double angle evaporation and lifted off in hot NMP. After junction deposition, the resistance of on-chip witness junctions was measured to determine junction yield and normal state resistances for both the small-area and large-area junctions. The normal state resistance is related to the Josephson energy by the Ambegaokar-Baratoff relation [6], allowing for estimation of the device energy scales prior to cooldown. If the mean resistance values and resistance spreads were within tolerance, samples were diced and packaged.

Samples were packaged in a 12-sided Al sample enclosure (shown in Fig. 10.3 (d)), and cooled in a blue-fors cryogen-free dilution refrigerator (Fig. 10.3 (a)). Transmission through the central feedline was monitored via heterodyne detection. Measurement pulses were synthesized with a quantum machines OPX+ and mixed with a carrier tone around a few GHz to produce arbitrary pulses at microwave frequencies. Inside the cryostat, measurement signals were attenuated by 20 dB at the 3 K stage, and in the case of the transmission lines and charge lines again at the mixing plate. Low pass filters and

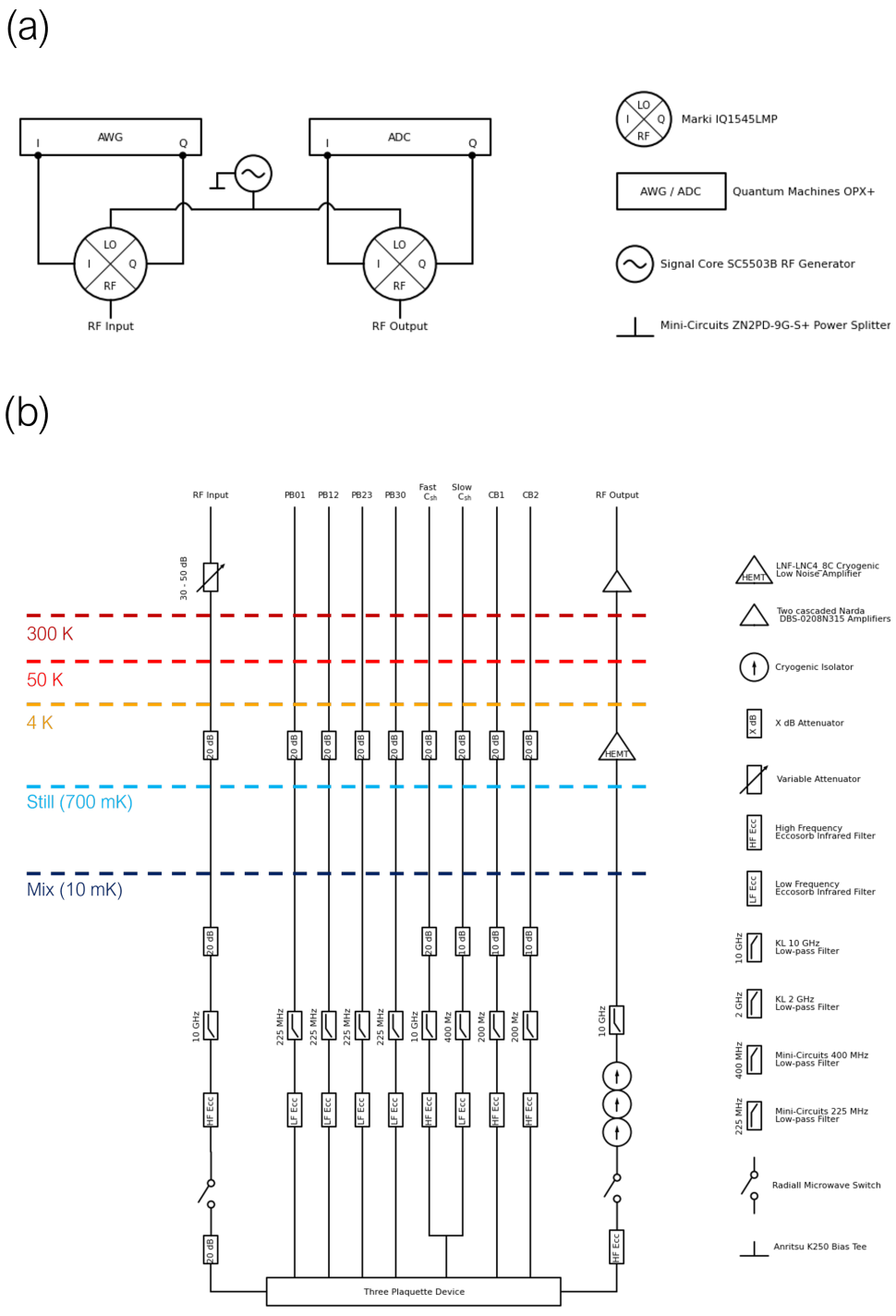

Figure 10.4: Microwave measurement setup. (a) Heterodyne setup used for synthesis measurement and drive pulses. (b) Wiring diagram for the three plaquette device.

eccosorb filters were used to further reduce light leakage from higher temperature stages and to filter out noise above the device frequency. Radiall microwave relays, modified for use in a cryogenic environment were used to increase measurement throughput.

Signals were subject to three stages of isolation at the mixing plate before amplification by a high-mobility electron transistor (HEMT) at the 3 K stage. Further amplification was done at room temperature. Upon returning to the electronics rack, waveforms sent through the on-chip transmission line were mixed to baseband using a copy of the microwave carrier tone. Further demodulation took place upon returning to the OPX+ for analog to digital conversion. Flux control pulses were synthesized directly with the OPX+. Microwave drive tones applied to the charge bias lines were mixed to microwave frequencies in the same way as was done for measurement tones sent through the device transmission line.

10.2 Traversing a multi-dimensional flux space

Upon cooling a device, the ability to tune each plaquette was verified. This was done by modulating the current applied to one or more of the bias lines located adjacent to that plaquette. The flux through each plaquette loop could be controlled via two on-chip bias lines, one coming up alongside the plaquette from each side. This was done to again ensure symmetric capacitance to ground of each plaquette in the chain. Fig. 10.5 shows the naming convention for the control lines of which there are four local flux bias lines, a global charge gate, and two local charge gates to control the offset charge on the intermediate island between plaquettes. Flux bias lines are labeled to indicate which two plaquettes in the chain they bias, counting up from the capacitor. 'Dummy' plaquettes (with shorted junctions) are labeled as 0. For instance, the flux bias line biasing plaquettes 1 and 2 would be called 'PB12'. The bias line biasing the third plaquette in the chain and the 'dummy' plaquette at the top of the chain would be labeled 'PB30'. Due to the close proximity of bias lines, it became critical to account for cross-talk between plaquettes.

To investigate how the device dynamics changed as we brought one plaquette, then two, then three to frustration, it was critical to be able to null the flux through plaquettes that

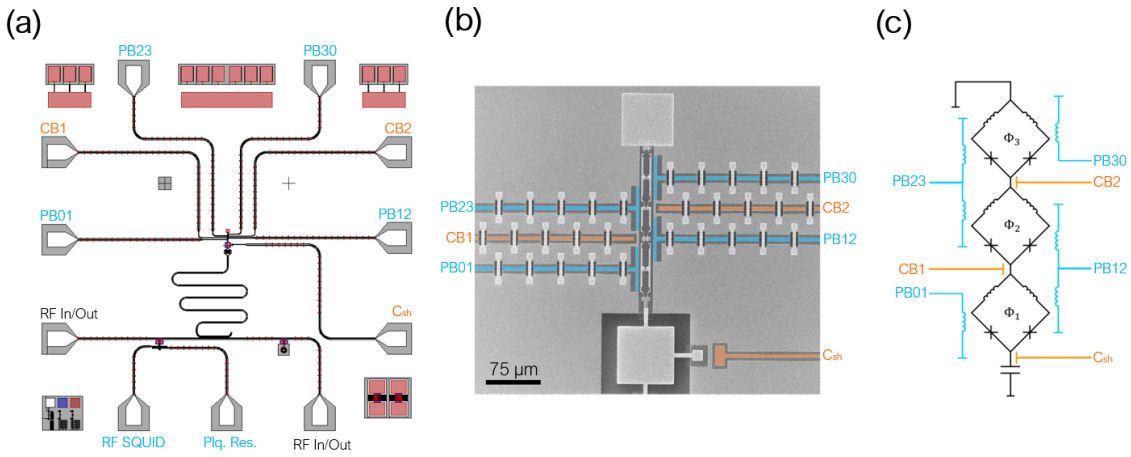

Figure 10.5: Control of multi-plaquette devices. (a) Screen capture of the design file for multi-plaquette devices. White is the Nb base layer, grey are areas where the Nb has been etched away exposing the silicon substrate. SiO_2 used in the parallel plate capacitor and crossovers is displayed in dark blue. Red is the Al counter-electrode. Flux bias lines are labeled in light blue, while charge gates are labeled in orange, the naming convention for which is described in the main text. (b) Scanning electron micrograph with flux and charge bias lines indicated in false-color. (c) Circuit representation with bias lines labeled and indicated in color.

weren't being actively investigated. The close proximity of bias lines around the multi-plaquette structure resulted in a non-negligible mutual between each of the plaquettes and all of the flux bias lines. As a result, it was critical to extract the mutual inductance matrix for the device in order to account for undesired biasing due to stray mutual inductances. The mutual inductance matrix

$$M = \begin{pmatrix} M_{11} & M_{12} & M_{13} \\ M_{21} & M_{22} & M_{23} \\ M_{31} & M_{32} & M_{33} \end{pmatrix} = \begin{pmatrix} 0.91 & 1.14 & 0.29 \\ 0.25 & 1.04 & 0.96 \\ 0.11 & 0.30 & 1.15 \end{pmatrix} \text{pH} \tag{10.1}$$

describes the mutual inductance between each superconducting loop and each on chip bias line. The vector of currents applied to the bias lines is related to the vector of fluxes through each superconducting loops by the following relation

$$\vec{I} = M\vec{\Phi}. \tag{10.2}$$

By inverting Eq. 10.2 it is possible for any point we would like to access in this three-dimensional flux space, to calculate what currents to apply simultaneously to the bias lines. We extract the mutual inductance matrix from a series of datasets where we monitor the cavity response while modulating the current applied to two of the bias lines simultaneously.

$$\begin{pmatrix} I_{\mathrm{PB01}} \\ I_{\mathrm{PB12}} \\ I_{\mathrm{PB23}} \end{pmatrix} = \begin{pmatrix} M_{11} & M_{12} & M_{13} \\ M_{21} & M_{22} & M_{23} \\ M_{31} & M_{32} & M_{33} \end{pmatrix}^{-1} \begin{pmatrix} \Phi_1 \\ \Phi_2 \\ \Phi_3 \end{pmatrix} \tag{10.3}$$

The eagle-eyed observer would note that we are in fact over-constrained since there are four bias lines and three plaquettes. The fourth bias line can be used as a global offset in this case, if the $\Phi_0/2$ operating place is near the extent of the output range of the fast electronics. It also provides critical redundancy in the event of a wiring error or damaged bias line.

In this series of datasets, shown in Fig. 10.6 (d)-(f) we can see two or three sets of transitions (parallel lines), depending on which lines are being biased. From the slopes and periods of these lines we extract the mutual inductance from each plaquette loop to each bias line, thus filling out the mutual inductance matrix. Once we have the full mutual inductance matrix we may inver it to calculate what currents to apply to each bais line to access any point in this multi-dimensional flux space. The result of this flux orthogonalization is shown in Fig. 10.6 (g)-(i). A horizintal or vertical line cut of one of these plots would correspond to biasing a single plaquette while nulling the flux through the other two loops. Points where two sets of lines intersect are where both plaquettes are brought to $\Phi_0/2$ simultaneously. Moving through this crossing diagonally would correspond to moving through double-frustration. Doing this same thing for the case where the third plaquette was held at $\Phi_{ext} = \Phi_0/2$ would be triple frustration.

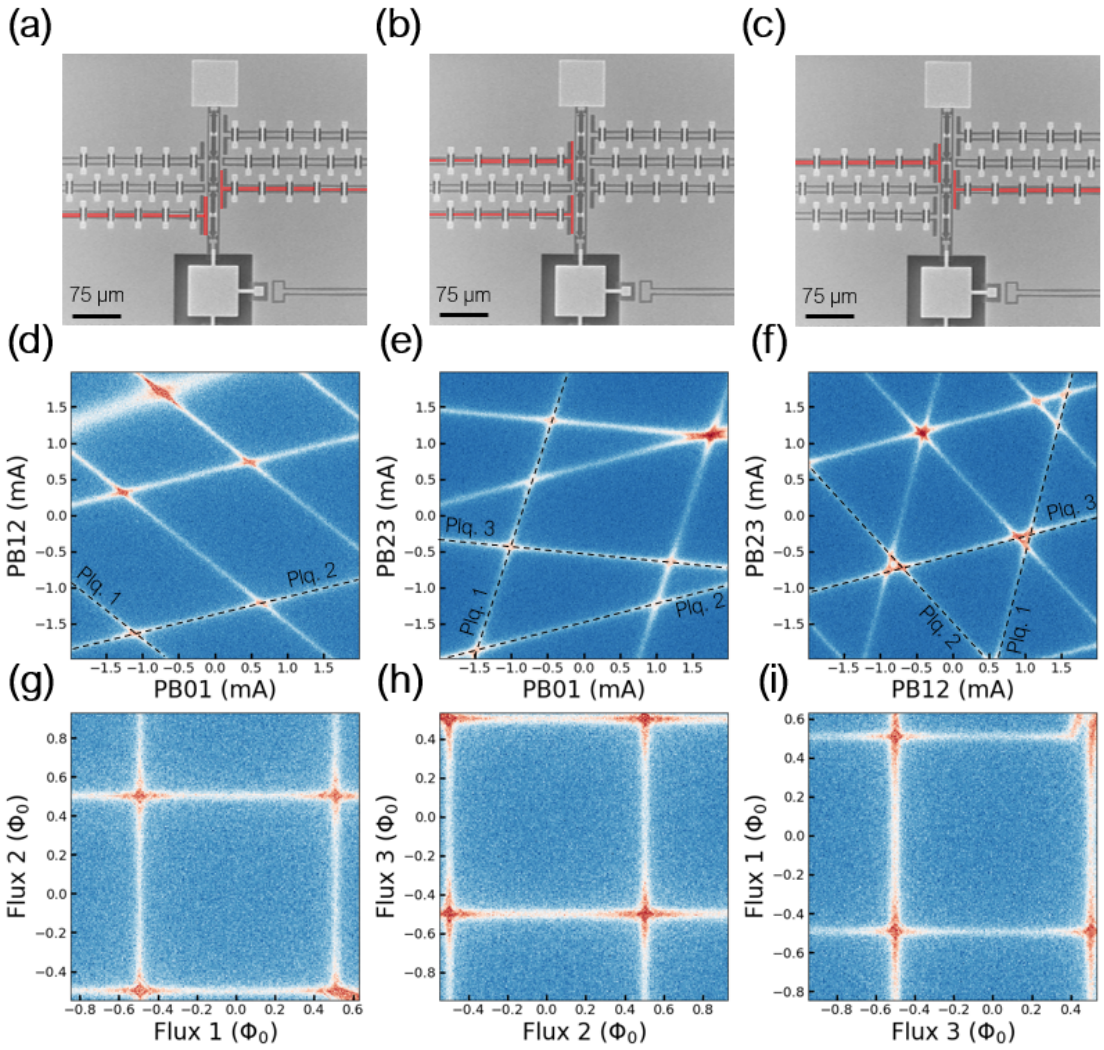

Figure 10.6: Flux orthogonalization. Upon cooldown the mutual inductances between each flux bias line and each plaquette are determined by monitoring the cavity response while sweeping two sets of bias lines simultaneously. The plaquettes are identified in each scan. From the slopes and periods of the transitions through this multidimensional flux space, we estimate the mutual inductances. (a)-(c) Scanning electron micrographs of the multi-plaquette structure. The bias lines for which the current is swept are shown false-color in red. (d)-(f) Cavity response as a function of the current applied to two flux bias lines. Each set of diagonal transitions corresponds to one plaquette in the chain. (g)-(i) Orthogonalized flux control. Cavity response due to sweeping the externally applied flux for two plaquettes while nulling the flux through the third.

Chapter 11

Measurement of multi-plaquette devices

In Chapter we discuss measurement of one and three-plaquette devices, with nominally identical parameters. These dies were located next to each other on the wafer during fabrication. We present initialization data and a measurement of relevant relaxation timescales for a single-plaquette device. We performs flux-based spectroscopy of a single-plaquette device, mapping out avoided level crossings between states in the two wells as a function of flux by monitoring the change ground-state in population as we move through the crossing. Finally, we present qubit spectroscopy data for one and three plaquette devices.

11.1 Measurement of single-plaquette devices

The single-plaquette device is a useful tool for learning how to initialize and operate these devices, however we do not expect this device to be protected. Hence, we move to multi-plaquette devices in subsequent sections.

11.1.1 Initialization in the fluxon basis

A critical ingredient for any qubit is the ability to initialize in the computational basis. One basis we may choose to work in is the fluxon basis, working with states localized in

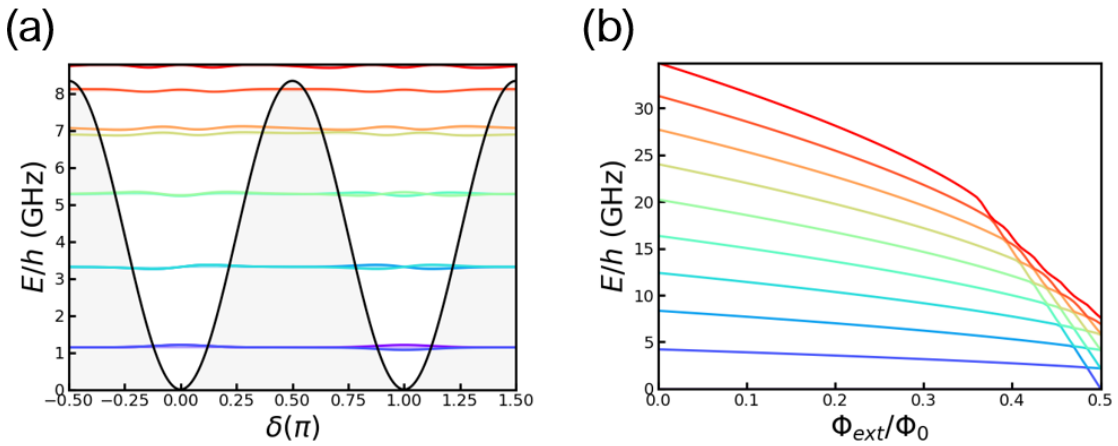

Figure 11.1: Energy level structure of a single-plaquette device. (a) Energy eigenstates of a capacitively shunted $\cos(2\delta)$ potential, offset by the eigenvalues, plotted on top of the potential, $E_2\cos(2\delta)$. This is what we expect for a perfect π-element (or equivalently, a plaquette biased at $\Phi_0/2$). The energy levels form doublets, with the lowest two localized deep within the wells. (b) Adding a $\cos(\delta)$ component to the potential, we calculate the energy eigenstates as a function of the externally applied flux, Φ_{ext}. At un-frustration ($\Phi_{\text{ext}} = 0\Phi_0$), there is a flattening of the energy bands as the $\cos(\delta)$ becomes dominant. Here we expect the response of the π-element to be like that of a traditional Josephson junction.

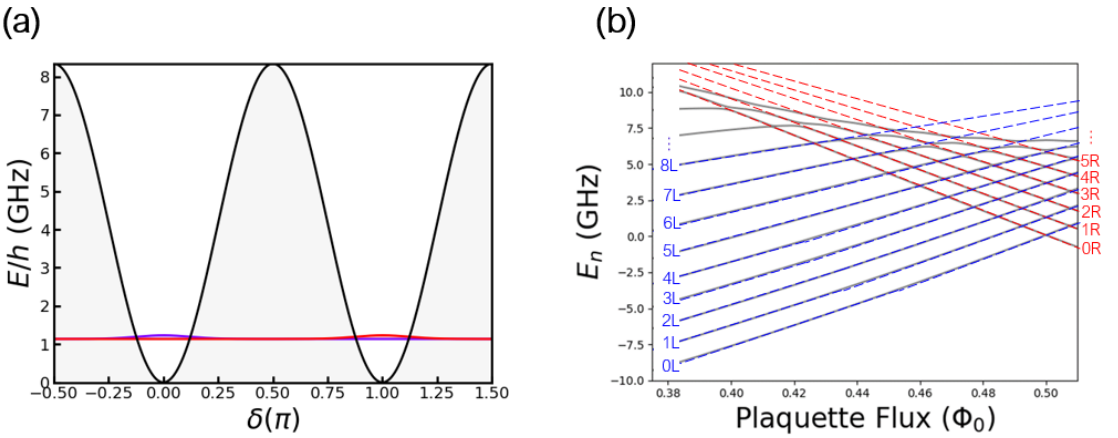

Figure 11.2: (a) The two lowest lying energy states in the fluxon (left-right) basis at $\Phi_{\text{ext}} = \Phi_0/2$. These states represent linear superpositions of the two lowest lying energy states in Fig. 11.1 (a). Explicitly relating the two lowest energy eigenstates to the left right basis, we have $|0\rangle = \frac{1}{\sqrt{2}}(|\text{left}\rangle + |\text{right}\rangle)$ and $|1\rangle = \frac{1}{\sqrt{2}}(|\text{left}\rangle - |\text{right}\rangle)$ [70]. (b) Energy structure of a single-plaquette device simulated using SuperQuantModel [71]. States originating in the left well are indicated with blue dashed lines while right well states are indicated with red dashed lines. Near $\Phi_0/2$, we expect myriad avoided level crossings between states in the left and right wells. States will often be referred to by these labels throughout the remainder of this thesis.

the left and right wells. For this type of device we can do a flux-based initialization to transfer population to the ground state of either the left or right well. To understand how this is possible, we must think about the energy level structure. Around half a flux quantum we have a double well potential. Away from half a flux quantum, we recover the $\cos(\delta)$ potential and the plaquette behaves similar to a normal Josephson junction. To initialize one well, for example, the left well, we need to bias far enough from half a flux quantum that we start to loose the right well, quickly dumping all of the population into the left well. It's via this maneuver that we may initialize population into either the left or right well.

Note that this initialization protocol does not require an drive on the internal state of the device. As such, for a sufficiently high barrier height (large capacitance), we can initialize and maintain population in one well or the other, and see this response in the cavity spectroscopy (Fig. 11.3 (a) and (b)). We first initialize one well or the other, then bias to wherever we would like to read out. Fixing the flux offset at which we readout, Φ_{ro}, and interleaving initializing in the left or right well, we can look at the signature of the two states in IQ space (Fig. 11.3 (c)). We can clearly distinguish between the two states. We observe that left right initialization in qubit spectroscopy as well, if we apply a drive tone at the frequency between the ground and first excited states. Shown in Fig. 11.3 (d) and (e), we again see that upon initialization in one state or the other, we maintain population in that state for about 100 $\mathrm{m}\Phi_0$.

The distance between the blobs is set in part by the location at which we choose to read out. Consider the coupled system shown in Fig. 11.4 (b). The frequency of the plaquette device (right side of the circuit diagram) will load the resonator frequency, further the plaquette device frequency will take different values depending on whether the device was initialized in the left well or the right well. The transition frequency to the first excited state, for a device initialized in the left well will be

$$\omega_{01,R} = \omega_{1L} - \omega_{0L} \tag{11.1}$$

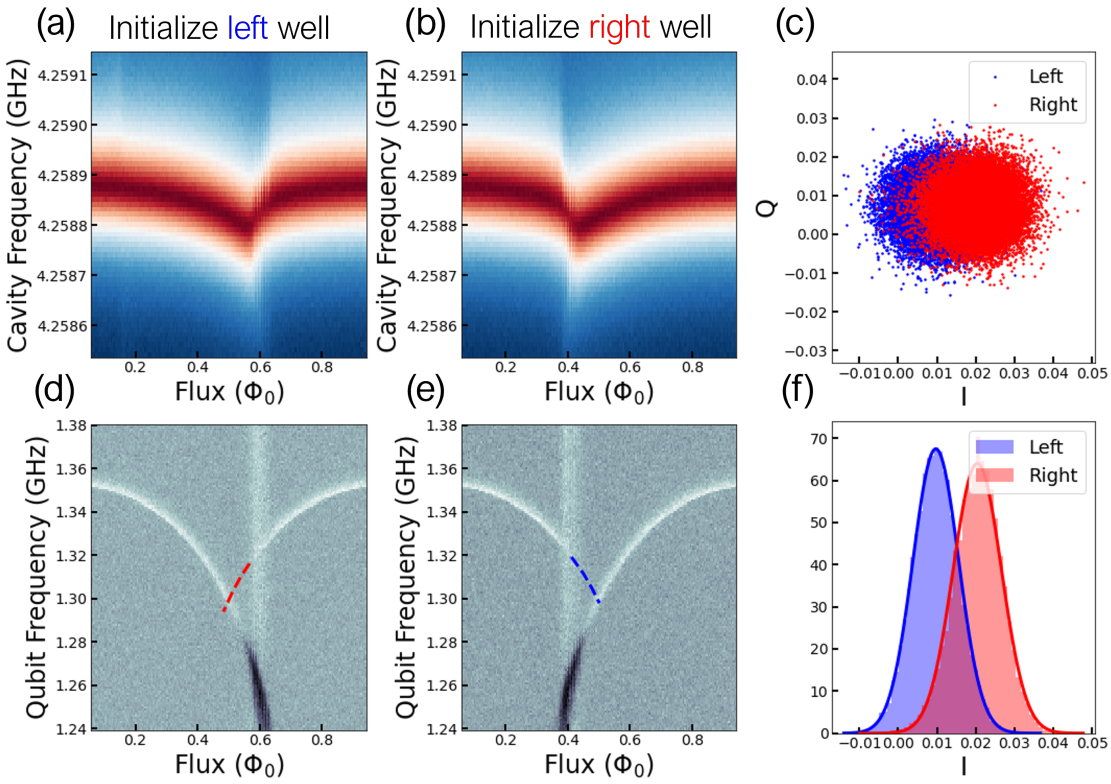

Figure 11.3: Initialization in the left-right basis. (a) Cavity response initializing the left well. Population is maintained in the left well for some ways past half a flux quantum. (b) Cavity response after initializing in the right well. Population is again maintained some ways past half a flux quantum. (c) IQ blobs for the left and right ground states when detuned from $\Phi_0/2$ by 70 mΦ_0. (d) Spectroscopy of the first excited state after initialization in the left well. And (e) Spectroscopy of the first excited state after initialization in the right well. (f) The distribution of points in IQ space in sub-figure (c), projected onto the line connecting the centers of the blobs (in this case the I axis), and plotted as histograms. This set of IQ data is later used for calibration of the population in either the left or right well. For mixed states, with population in both wells, we fit the histogram with a two-component Gaussian to extract the population in each well, using this dataset for calibration.

and similarly for the right well

$$\omega_{01,R} = \omega_{1R} - \omega_{0R} \tag{11.2}$$

From the simulated spectra, we can then define an effective inductance for the plaquette device,

$$L_{\text{eff},L} = \frac{1}{\omega_{01,L}^2 C_q} \quad \text{and} \quad L_{\text{eff},R} = \frac{1}{\omega_{01,R}^2 C_q} \tag{11.3}$$

which will again depend on in which state the device was initialized. We can solve for the loaded frequency using the method of load lines since we know that the imaginary part of the admittance at the node between the resonator and the plaquette circuit must be zero. Let the loaded frequency of the coupled system for a device initialized in the left well be ω_L and ω_R for a device initialized in the right well. From here, we can define an effective dispersive shift

$$2\chi_{\text{eff}} = \omega_L - \omega_R \tag{11.4}$$

As we near $\Phi_{\text{ro}} = \Phi_0/2$, we expect the blobs to be nearly indistinguishable, as separation between the two ground states in frequency decreases (equivalently, $\omega_L \approx \omega_R$). However, de-tuning from frustration χ_{eff} will increase, resulting in increased measurement visibility. To see this concretely, one would include the coupling circuit, write down an expression for the impedance of the combined circuit. From this one can get an expression for transmission across the cavity (as was done in Chapter 2) and finally, relate this quantity to the centers of the IQ blobs.

Ultimately we would like to probe the dynamics at $\Phi_{\text{ext}} = \Phi_0/2$. One challenge that accompanies this type of flux based initialization is that in order to bias to $\Phi_0/2$ we must pass through myriad avoided level crossings. As we tune in flux the depths of the wells shifts, bringing different levels in the two well near each other in frequency. When this happens, there will be an avoided level crossing, which provides a mechanism via which we can exchange population between the two states. Traversing these crossings too quickly can result leakage out of the computational subspace. This can be mitigated through the use of pulse shaping, for instance softening the rise edge of the pulse.

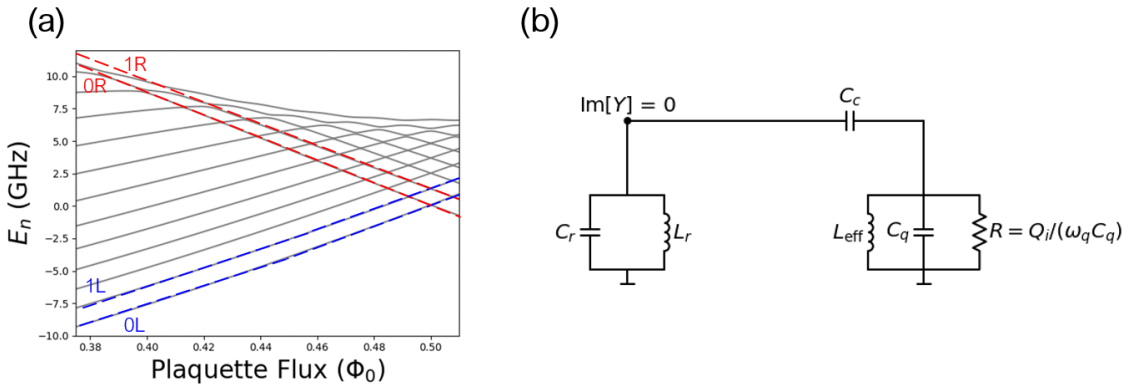

Figure 11.4: Effective dispersive shift χ_{eff}. (a) Simulated energy level spectra [71] with the first two states in each well indicated. The transition frequency of the plaquette device will be the difference in frequency between the 0L and 1L states, in the case of left well initialization or the difference between the 0R and 0L states in the case of right well initialization. Depending on which state the plaquette device is in, for a given flux offset, the resonator will have a different loaded frequency. The difference between these two resonator frequencies will directly impact the readout visibility (the separation between IQ blobs in Fig. 11.3 (c)). (b) Circuit representation of the coupled system. In the design stage, we can estimate the readout visibility from the simulated spectra, using the simulated transition frequencies to define an effective inductance, L_{eff}. We can calculate the loaded frequency for the plaquette device in the left or right state by setting the imaginary part of the admittance to zero at the node between the coupled resonators, and solving for the new resonant frequency.

11.1.2 Relevant relaxation times

Having demonstrated successful initialization in the left-right basis, we can now probe the relevant relaxation times of the device, of which there are two.

The *intra-well* relaxation time, or relaxation time between states within a single well is the timescale most comparable to the T_1 of a transmon qubit (Fig. 11.5 (a)). It is measured by applying a pulse at the frequency between the ground state and first excited state in order to excite population into the higher state. One then waits a variable amount of time before reading out the state, in order to measure the time it takes to relax back to the ground state. Data with an exponential fit to extract the time constant is shown in Fig. 11.5 (c). The measured intra-well relaxation time is 388 ns. For this iteration of plaquette devices we expect the intra-well relaxation time to be very short, on the order of a few hundred nanoseconds. This is due to the fact that a lossy dielectric has been used in the construction of the parallel plate capacitor. We expect the intra-well relaxation time to be limited by two-level fluctuators. Luckily, this is not the most relevant timescale for the operation of these devices.

Since protection from bit-flip errors stems from the suppression of tunneling between the two wells, the *inter-well* well relaxation time, that is the relaxation time between states in different wells (Fig. 11.5 (b)) is more relevant when characterizing the performance of these devices. The inter-well relaxation is measured by first idling to one side of frustration in order to initialize one of the wells, then biasing through half a flux quantum such that the initialized well is no longer the global minimum, idling for a variable wait time, then reading out the device state. This is repeated for a range of idle times. Data for this experiment is shown in Fig. 11.5 (d). Fitting an exponential to the data as a function of time allows us to extract the relaxation time, 1.2 ms. This dataset was taken 100 mΦ_0 from frustration. In general, we expect this relaxation time to increase as we approach frustration because the ground states become more deeply localized in the two wells. However, as one moves closer to frustration it becomes increasingly difficult to differentiate between the two states as they move towards near-degeneracy. A long inter-

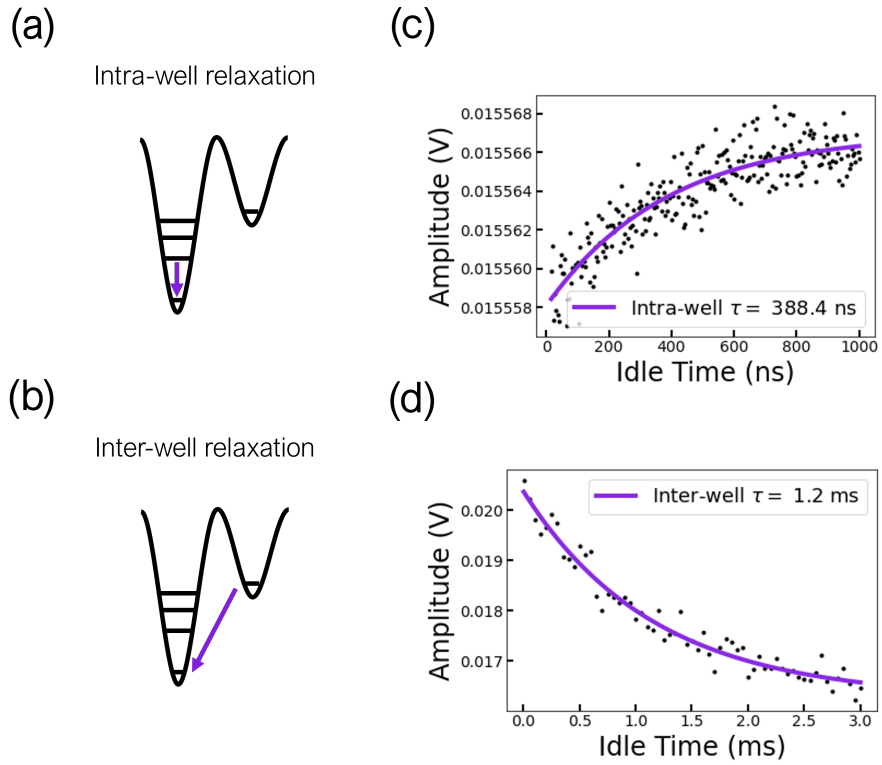

Figure 11.5: Measurement of relaxation times of plaquette devices. (a) The intra-well relaxation time is the relacation time between states within a single well. (b) The intra-well relaxation time is the relaxation time between states in adjacent wells. (c) Measured intra-well relaxation time for a single-plaquette device. The intra-well relaxation time is limited by TLS losses due to the parallel plate capacitor. (d) Measured inter-well relaxation time, when biased 100 mΦ_0 from half a flux quantum.

well relaxation time indicates the suppression of tunneling between states in adjacent wells, which as discussed in Chapter 8, is the source of protection from bit-flips in this device.

11.1.3 Flux-based spectroscopy of plaquette devices

Having measured the relevant timescales of the device we move towards probing the time domain dynamics near frustration with two goals: (1) to verify experimentally the device parameters and (2) to observe population transfer between states in the left and right wells. We revisit the energy level structure of the device around $\Phi_0/2$ (shown in Fig. 11.6). Ultimately, we would like to work towards observing coherent population transfer from the ground state in the left well (0L) to the ground state in the right well (0R), or vice versa. The lowest energy avoided crossing, located at $\Phi_0/2$ allows for interaction between the two ground states, however, due to the near degeneracy of the two states the energy splitting between the states will be very small (see Fig. 11.7, top inset) and difficult to resolve in spectroscopy. Further, due to the linear flux dispersion of the single plaquette device, the avoided crossing will be exist over a very small range of fluxes, of order 10 $\mu\Phi_0$, which is both at the resolution the fast electronics available for use in this experiment, and of order the expected flux noise for this system. As a result observing population transfer via the 0R-0L avoided crossing would be incredibly challenging.

In addition to the crossing between the two ground states, de-tuning from frustration there will be crossings between the ground state in one well (in this example, the right well), and higher excited states in the other well (Fig. 11.6). As the potential shifts, and these states are brought near to each other in frequency they are given the opportunity to interact. From the simulated spectra (Fig. 11.7, lower inset) we see that the avoided crossings between the ground states in one well and higher excited states in the other well increase in size as we move further from frustration. For example, from the spectra simulated using nominal device parameters we expect the 0R-8L to be much larger, with an energy splitting of order 10 MHz, and spanning mΦ_0 in flux rather than $\mu\Phi_0$.

Population transfer via these avoided level crossing will be governed by the Landau-

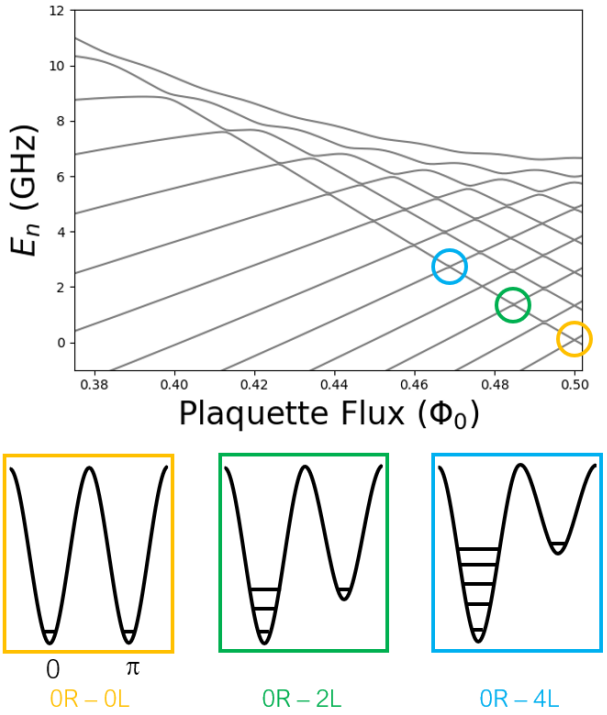

Figure 11.6: Single-plaquette device spectra calculated using SuperQuantPackage [71]. At half a flux quantum the lowest energy avoided crossing will be between the left-well ground state and the right-well ground state (yellow). De-tuning from $\Phi_0/2$, we expect to see avoided crossings between the ground state in the right well and higher excited states in the left well (green and blue).

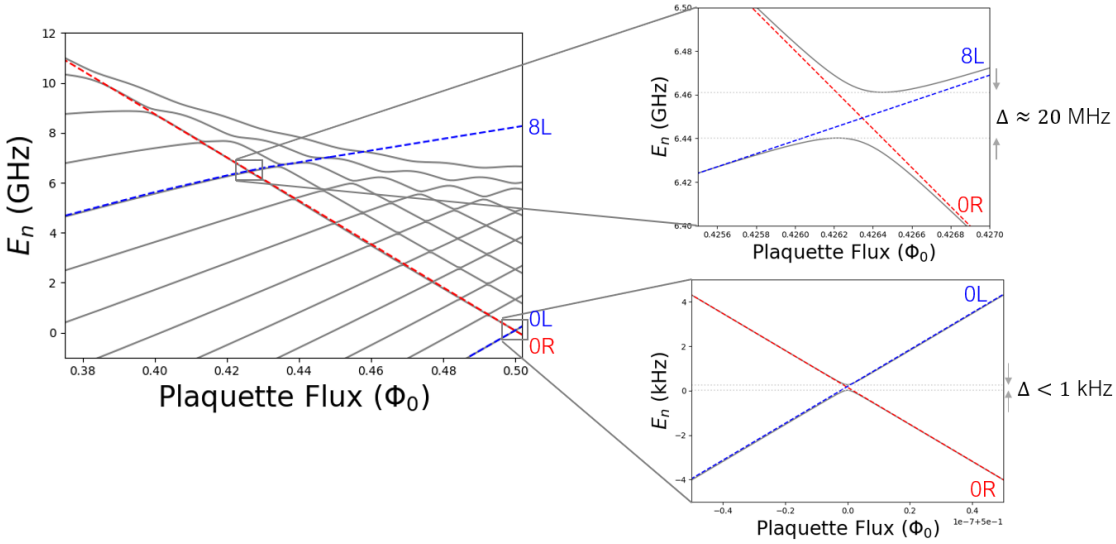

Figure 11.7: Calculated single-plaquette spectra [71]. The energy splitting between the ground state in the left well, 0L, and the ground state in the right well, 0R, at $\Phi_0/2$ is necessarily very small, due to the near degeneracy of the computational states. Further, for a single-plaquette device this splitting occurs over a small range of fluxes, comparable to the level of flux noise expected in this system. This is due to the linear flux dispersion of a device with a single π-element. However, de-tuning from $\Phi_0/2$, avoided crossings between the ground state in one well, in this case 0R, and higher excited states in the other well, for example 8L, increase in size. By navigating these crossings in a controlled way we can transfer population from the right well to the left well. This population transfer is described by the Landau-Zener formula [72, 73].

Zener formula [72, 73]. Hence the probability of remaining in the right well will be

$$P_R = e^{-\pi^2 \Delta^2/(df/dt)} \tag{11.5}$$

where Δ is the energy splitting in units of frequency and df/dt is that rate of change of frequency (the rate with which one navigates the avoided crossing). This is related to the flux pulse ramp rate via the flux dispersion

$$\frac{df}{dt} = \frac{d\Phi}{dt}\frac{df}{d\Phi} \tag{11.6}$$

such that the condition for adiabatic passage becomes

$$\Delta^2 \gg \frac{d\Phi}{dt}\frac{df}{d\Phi}. \tag{11.7}$$

Hence, ramping the flux more slowly we expect greater population transfer from one well to the other. By varying the ramp rate, and the flux that we idle at, it should be possible to map out the size and locations of the avoided crossings, which uniquely determine the device parameters. The measurement sequence (Fig. 11.8) is as follows: we first initialize in one well or the other, as was described in Section 11.1.1. We then modulate the flux, with a known rate to the bias offset (past frustration) where we would like to probe the dynamics, Φ_{probe}. We idle for a short time, allowing the system to quickly relax into the ground state of the other well. Finally, we quickly bias and read out. Fixing the readout location, Φ_{ro} allows us to calibrate the left-right well population by fitting a two component Gaussian to the IQ data (as described in Section 11.1.1). Repeating this measurement sequence, varying Φ_{probe}, allows us to map out the locations of the avoided crossings in flux space. Repeating this scan for a range of ramp rates, and using Eq. 11.5 along with the simulated flux dispersion it should be possible to extract the sizes of the avoided crossings.

Fig. 11.9 shows the result of this experiment for the single plaquette device. Here we are initializing population in the right well, then bias past frustration, transferring

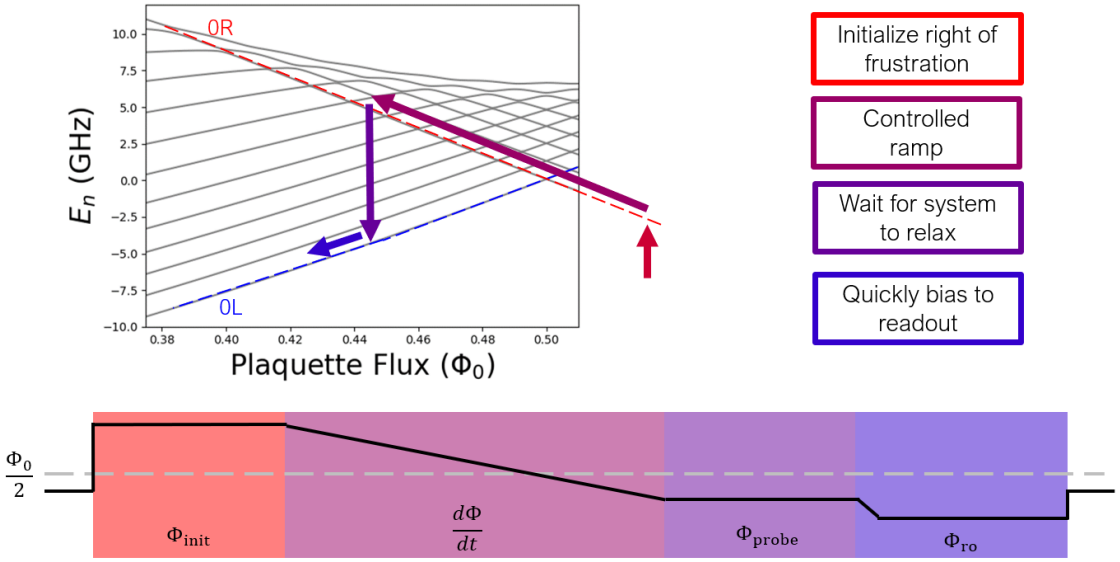

Figure 11.8: Measurement sequence for flux-based spectroscopy of plaquette devices. First, one well (right) is initialized as described in the previous Section. Then, the flux is modulated past $\Phi_0/2$ at a controlled rate, $d\Phi/dt$. Idling at the flux we wish to probe, Φ_{probe}, the system quickly relaxes to the ground state of the left well. We then bias and readout at a fixed flux offset, Φ_{ro}. Repeating this experiment, sweeping Φ_{probe} and varying the ramp rate, $d\Phi/dt$, we can map out the locations and sizes of avoided level crossings.

population to the left well. Starting about 100 mΦ_0 left of frustration we begin to see drops in population as we pass through avoided crossings. Sharp drops, are presumable where we are idling on an avoided crossing. As we increase the ramp time, we see that we are getting more population transfer. This is qualitatively consistent with what we expect.

While the single-plaquette device is a simpler system, allowing us to learn how to initialize and manipulate these devices, we do not expect protection against phase errors in such a device. We ultimately need to push towards multi-plaquette devices.

11.2 Measurement of three-plaquette devices

Pushing onward toward the three plaquette device, we have already shown that we can successfully navigate this multi-dimensional flux space. We begin to probe the energy level structure of these devices around $\Phi_0/2$.

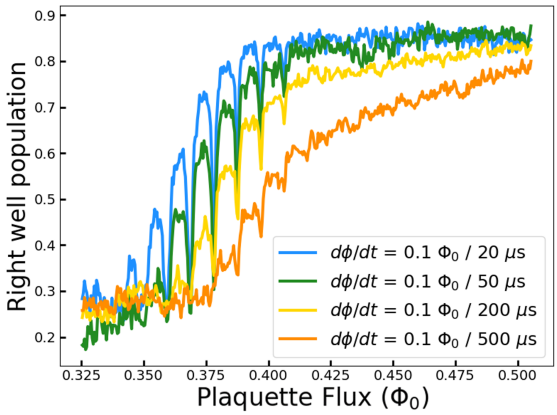

Figure 11.9: Initializing the right well, then biasing past frustration in a controlled way, drops in population, the result of navigating avoided level crossings adiabatically, are observed. As expected, slower ramp rates correspond to larger population transfer.

11.2.1 Spectroscopy of higher excited states

We perform spectroscopy of the device's excited states, in the same way that qubit spectroscopy is typically done for conventional superconducting qubits. We apply a drive tone, in this case to the charge line capacitvely coupled to the shunt capacitor, in order to excite the device out of the ground state. Due to the short intra-well relaxation time the drive pulse is often overlapped with the readout tone. Sweeping the frequency of the drive tone and the flux offset, we identify transitions between energy levels, mapping them out as a function of flux.

We begin by working around single frustration where one plaquette in the chain is biased at half a flux quantum and the other two are kept at zero flux offset. Fig. 11.10 (e)-(g) shows spectroscopy of the first excited state modulating the flux through ony one of the plaquettes. Each of the lower scans is taken along the flux trajectory indicated by the black dashed line in the plot above. In all cases we see that the spectra are relatively symmetric, dispersing strongly around $\pm\Phi_0/2$. Looking over a smaller range of fluxes around $\Phi_0/2$ (see Fig. 11.11 (c)) we see a number of transitions, both plasmons (intra-well transitions) and fluxons (inter-well transitions) [63]. We identify the plasmon corresponding to the first excited state around 700 MHz, in addition to a direct drive to the third excited state around 2.1 GHz. The fluxons are the strongly dispersing transitions

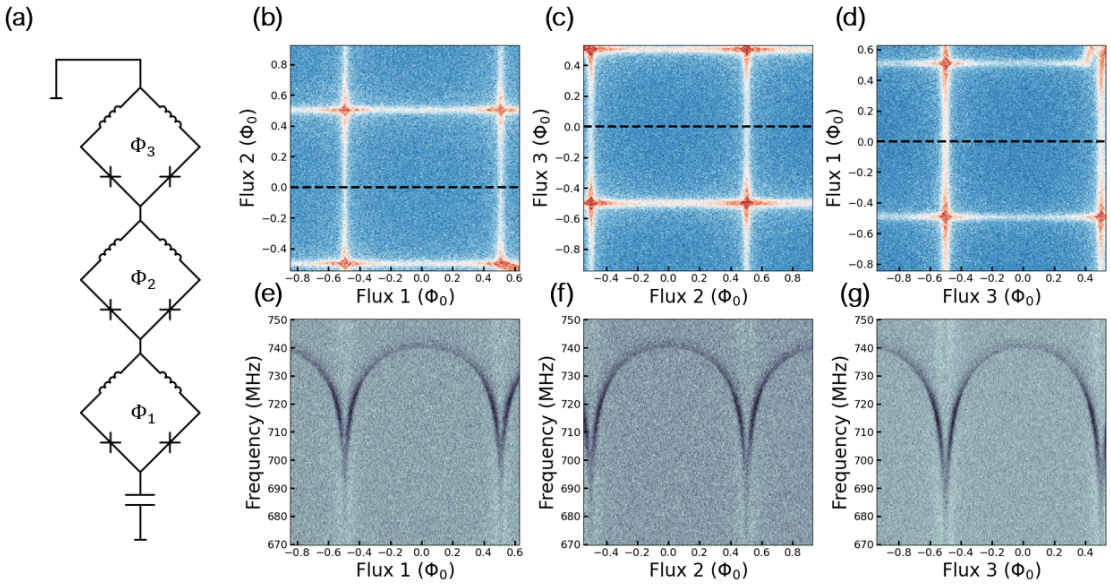

Figure 11.10: Spectroscopy of first excited state around single frustration ($\Phi_{1,2,3} = \Phi_0/2$). (a) Circuit representation of three-plaquette device. (b)-(d) Cavity response as a function of two flux offsets. The black dashed line indicates the flux trajectory along which spectroscopy measurements were taken (below). (e)-(g) Spectroscopy of the first excited state while biasing the flux through one plaquette only (nulling the flux through the other two). We see that the spectra are relatively symmetric and disperse strongly around $\pm\Phi_0/2$.

seen cutting across the plasmons.

Moving now toward plauqette 1-2 double frustration ($\Phi_1 = \Phi_2 = \Phi_0/2$), we repeat this type of measurement moving along the trajectory indicated by the black dashed line in Fig. 11.11 (d)[1]. We again see the first excited state around 650 MHz, along with the third excited state around 2 GHz. In addition to these transitions, a transition involving the cavity [63] is indicated with the orange dashed line. For these measurements a microwave generator gated with a microwave switch was used in order to sweep over a large range of frequencies without needing to worry about the spurious[2] tones from the mixer. Looking forward, the intention is to use one of the higher excited states identified in spectroscopy to perform initialization and coherent manipulation via a two-tone drive, as has been previously demonstrated in fluxonium circuits [61, 62].

11.3 The path toward coherent control

Due to the nature of protection in this device, the path towards coherent control is a challenging one. The near degeneracy of the ground state doublet at frustration provides protection in that any environmental fluctuations will affect the two states in a similar way. However, this near degeneracy also makes it challenging to initialize the device at half a flux quantum. And while one could imagine using the flux-based initialization described in Section 11.1.1 then biasing to half a flux quantum, traversing the myriad avoided crossings around frustration presents ample opportunity for leakage. Alternative approaches, borrowed from the fluxonium literature [61, 62], rely on multiple microwave drives.

Akin to the heavy fluxonium system, when de-tuned from half a flux quantum, the ground state in each well and a higher state form a lambda system. Following the protocol described in [61], one could coherently address the computation states by simultaneously applying two microwave tones (ν_{pump} and ν_{probe}) to pump population from one ground

[1] An aside on the cavity response shown in Fig. 11.11 (d): the intricate fine structure around frustration is due to higher excited states dispersing across the cavity [63]

[2] Image and local oscillator bleed-through

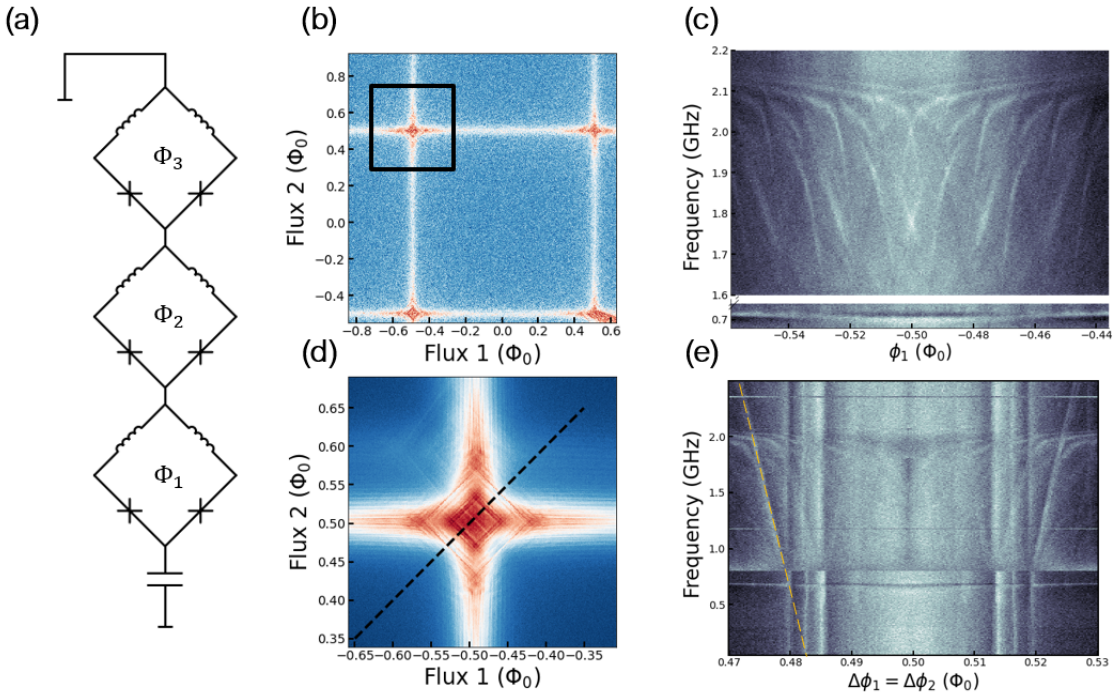

Figure 11.11: Spectroscopy of excited states around single ($\Phi_{1,2,3} = \Phi_0/2$) and double frustration ($\Phi_1 = \Phi_2 = \Phi_0/2$). (a) Circuit representation of three-plaquette device is reproduced here. (b) Cavity response as a function of plaquette 1 and plaquette 2 flux offsets. The black box indicates double frustration. (c) Spectroscopy of higher levels around plaquette 1 single frustration. We observe transitions to the first and third excited state plasmons around 0.7 GHz and 2.1 GHz, respectively. Strongly dispersing transitions are fluxons, transitions between states in different wells. (d) Cavity response over a smaller range of fluxes around double frustration. The black dashed line indicates the flux trajectory along which spectroscopy presented in sub-figure (e) was taken. (e) Spectroscopy of higher excited states around plaquette 1-2 double frustration. Again, the first and third excited state plasmons are visible around 0.65 GHz and 2.0 GHz. Fluxons are also visible, in addition to a transition involving the cavity (orange dotted line), identified by Dodge and Liu *et al* [63].

state to the other, in a technique closely related to optical pumping. However, to successfully implement this protocol, one must first identify a higher excited state with sufficient participation in both wells. This would likely need to be a much higher excited state due to the large shunt capacitor causing lower excited states to still be localized in a single well. Further, the intermediate state would need to have sufficiently long coherence time to support population transfer. Since the quality factor of each state is expected to be limited by the lossy dielectric used in the parallel plate capacitor, the intra-well relaxation time of the n^{th} excited state would scale as $T_{0n} \approx T_{01}/n = 388\text{ns}/n$, making this maneuver difficult.

An alternate approach, successfully demonstrated in the fluxonium literature [62], utilizes excited state doublets and along with states of the readout resonator to initialize, manipulate, and read out the computational states. The authors take advantage of parity selection rules to selectively pump population from the ground state of one well to the readout resonator, via an intermediate excited state. Population transferred to the readout resonator would quickly decay out of the system. This protocol presents a path toward initialization of the device at half a flux quantum. However, further modeling of the system would be needed to identify viable excited state doublets for use in the protocol.

Chapter 12

Outlook on protected qubits

The successful implementation of a fully protected qubit remains an exciting challenge for the superconducting qubit community. Proposals for which often require stringent control of device energy scales [58, 59], target parameters that are challenging to realize with existing fabrication procedures, and rely on complex control schemes to manipulate and read out the devices [63]. And while the technical requirements are daunting, full simulation and modeling of such devices can take days or even weeks on a lab computer [63]. The complexity of these devices compared to more traditional superconducting qubits, such as the transmon [5], make this a challenging prospect to achieve on the timescale of a single graduate education.

Because of this, the body of academic papers on protected qubits remains relatively small even as the field expands rapidly. Instead, much of the work that has been done on protected qubits lives in the theses of students who spent a portion of their graduate career working towards this goal [65, 66, 74–76]. In spite of this, there remains increased effort and interest, as demonstrated by changes in APS March Meeting offerings over the years. In 2018 the Superconducting Qubits: Novel Devices session at the APS March Meeting contained a single talk about a protected $0-\pi$ qubit [77]. An additional talk by A. Gyenis appeared in the session: Characterizing and Controlling Superconducting Circuits II [78]. Last year at the 2024 APS March Meeting in Minneapolis, six of the thirteen talks in the

Novel Superconducting Qubits session were dedicated to discussing $0-\pi$ qubits [79], with a further four talks on protected qubits in the Unconventional Superconducting Qubits session [80]. And this list is by no means exhaustive. I am hopeful that as the field continues to progress, pushing the boundaries of what is possible in fabrication, improving the speed and dynamic range of control electronics, and learning how to better model the dynamics of these circuits that we will soon see demonstration of a topologically protected superconducting qubit.

Ultimately, what drew me to this field was the diversity of quantum systems that one could engineer with three macroscopic circuit elements: the capacitor, the inductor, and the Josephson junction. And while protected qubit projects such as the one pursued in this thesis highlight the versatility of the superconducting circuit toolbox, they also demonstrate the engineering challenges associated with controlling and understanding the technology that we build.

Appendix A

Mathematical derivations

A.1 Parallel to series circuit mapping

Mapping a series combination of a resistor and inductor or capacitor to an equivalent parallel circuit is a useful trick for describing qubit drive terms [81] or capacitive coupling of superconducting resonators (see Appendix A.2), among other applications. We employ this trick in Chapter 2 to derive the resonator response due to a change in the quasiparticle distribution in the Al sensor strip of our detector. This derivation closely follows the work of [82].

Suppose that we have a parallel combination of a resistor, R_P, and capacitor or inductor (referred to here by the reactance, X_P), as shown in Fig. A.1 (a). We can write down the expression for the impedance of this circuit

$$Z_P = \frac{1}{1/R_P + 1/(iX_P)}. \tag{A.1}$$

Multiplying by the complex conjugate, we can rewrite this as

$$Z_P = \frac{iR_PX_P}{R_P + iX_P}\frac{R_P - iX_P}{R_P - iX_P} = \frac{R_PX_P^2 + iR_P^2X_P}{R_P^2 + X_P^2}.$$

The expression can be further simplified using the expression for the quality factor of a parallel circuit, $Q_P = R_P/X_P$:

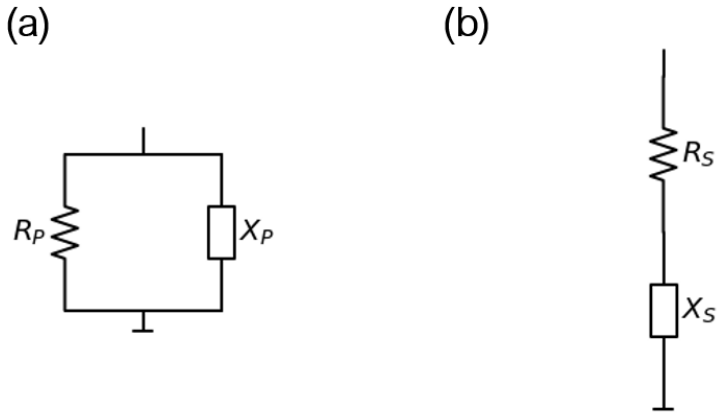

Figure A.1: Parallel and series combinations of a resistance and reactance. The reactance can describe either a capacitor, $X_C = -1/\omega C$, or inductor, $X_L = \omega L$.(a) The parallel combination has a combined impedance, $Z_P = (1/R_P + 1/(iX_P))^{-1}$. (b) Series combination, with combined impedance, $Z_S = R_S + iX_S$.

$$Z_P = \frac{R_P X_P^2 + iR_P^2 X_P}{X_P^2(Q_P^2+1)} = \frac{R_P + iQ_P^2 X_P}{(Q_P^2+1)}.$$

Having separated the real and imaginary parts of this expression, we now have something that looks like a series combination of a resistor and inductor or capacitor (Fig. A.1 (b)), $Z_S = R_S + iX_S$. We can define a series resistance and reactance from this expression:

$$Z_P = \underbrace{\frac{R_P}{(Q_P^2+1)}}_{R_S} + i\underbrace{\frac{Q_P^2 X_P}{(Q_P^2+1)}}_{X_S}. \tag{A.2}$$

To use this mapping in both directions, we need to rewrite R_S and X_S so that it's not dependent on Q_P, which may not be known if we're starting from the series combination and mapping to the parallel combination. This can be done using the fact that the quality factor of the series and parallel circuits must stay the same. We can show this mathematically, starting from the expression for the quality factor of the series circuit, $Q_S = X_S/R_S$. Using our expressions for R_S and X_S, we can rewrite this in terms of the parallel quality factor, Q_P.

$$Q_S = \frac{X_S}{R_S} = \frac{Q_P^2 X_P}{Q_P^2+1}\frac{Q_P^2+1}{R_P} = Q_P^2\frac{X_P}{R_P} = Q_P$$

Having shown that the quality factor of the series and parallel circuits must be the same, we can rename the quality factor $Q_P = Q_S = Q$. We summarize the transformation between the series and parallel circuits:

$$R_P = R_S(Q^2+1) \quad \text{and} \quad X_P = \frac{X_S(Q^2+1)}{Q^2} \tag{A.3}$$

Finally, one important case to discuss is the case where $Q \gg 1$. In this case, we find

$$R_P \approx R_S Q^2 \quad \text{and} \quad X_P \approx X_S \tag{A.4}$$

All applications of this mapping discussed in this thesis fall into the high-Q limit.

A.2 Q_c of a capacitively coupled $\lambda/4$ resonator

We can apply the series-to-parallel mapping derived in Appendix A.1 to derive the expression for the coupling Q of a $\lambda/4$ resonator capacitvely coupled to a feedline (Fig. A.2(a)), in terms of the coupling capacitance, C_c. From the standpoint of the coupling capacitor looking into the resonator, the CPW resonator looks like a short at the far end. As such, we can map the $\lambda/4$ resonator to a parallel LCR tank circuit [22]. The resulting circuit is shown in Fig. A.2(b), where the the input and output impedance (typically 50Ω has been combined and denoted as a single resistive element.

We can map the coupling circuit to an equivalent parallel circuit, as shown in Fig. A.2 (c). Applying Eq. A.4 and using the expression for the quality factor of a series circuit we find:

$$X_P = X_{C_c} = \frac{1}{\omega C_c} \quad \text{and} \quad R_P = \frac{Z_0}{2}Q_S^2 \quad \text{where} \quad Q_S = \frac{X_S}{R_S} = \frac{1}{\omega C_c Z_0/2}$$

We can now combine the capacitances and resistances in parallel, defining new effective

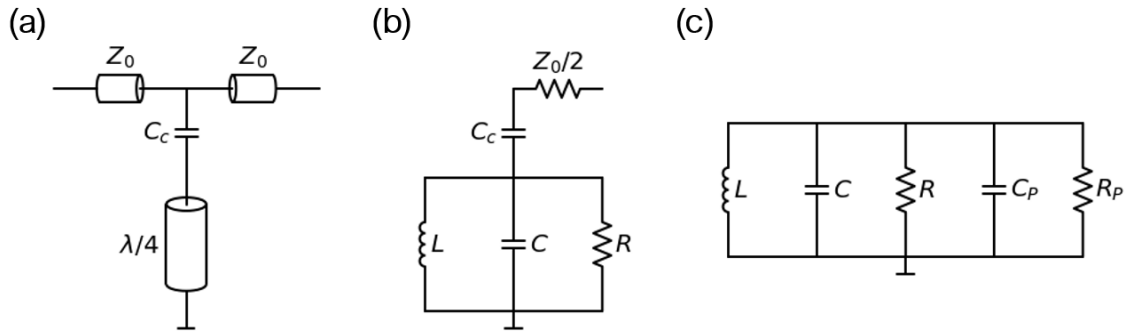

Figure A.2: Circuit representation of a capacitvely coupled quarter wave resonator. (a) (b) The quarter wave resonator can be mapped to an equivalent parallel LCR tank circuit. (c) Circuit, including coupling circuit, after application of the parallel-to-series mapping derived in Appendix A.1.

capacitance and resistance:

$$C_{\text{eff}} = C + C_c \quad \text{and} \quad R_{\text{eff}} = \left(\frac{1}{R} + \frac{1}{R_P}\right)^{-1}$$

We can now calculate the quality factor of the parallel circuit:

$$Q_P = \frac{R_{\text{eff}}}{Z_{LC}}, \quad \text{where} \quad Z_{LC} = \sqrt{\frac{L}{C}} \tag{A.5}$$

We know that quality factors will add in parallel. We can rewrite this total quality factor as the parallel combination of the internal quality factor of the LC circuit and the quality factor of the coupling circuit.

$$\frac{1}{Q} = \frac{Z_{LC}}{R} + \frac{Z_{LC}}{Q_S^2 Z_0/2} \equiv \frac{1}{Q_i} + \frac{1}{Q_c} \tag{A.6}$$

Finally, using the expression for the resonant frequency of the LC circuit, $\omega_0 = 1/\sqrt{LC}$, we can rewrite the expression for the coupling quality factor, Q_c

$$Q_c = \frac{Q_S^2 Z_0}{2Z_{LC}} = \frac{Z_{LC}}{Z_0/2}\left(\frac{C}{C_c}\right)^2 = \frac{2C}{\omega_0 Z_0 C_c^2} \tag{A.7}$$

The same analysis can be done for an inductively coupled $\lambda/4$ resonator, however, an additional step is required to map the coupling inductor to an inductive network. The

details of this analysis can be found in [81].

A.3 IQ Mixer math

In this Appendix we work through the math to see how base-band waveforms output from the AWG are mixed up to microwave frequencies with the help of an IQ mixer. This derivation follows closely the work of [83, 84]. For convenience, the relevant trigonometric identities are listed below:

$$\cos\alpha\cos\beta = \frac{1}{2}[\cos(\alpha+\beta)+\cos(\alpha-\beta)] \tag{A.8}$$

$$\sin\alpha\sin\beta = \frac{1}{2}[\cos(\alpha-\beta)-\cos(\alpha+\beta)] \tag{A.9}$$

For this analysis we'll be a little sloppy and disregard the amplitude of the signals. The point of this note is to gain intuition for how we're able to synthesize fast arbitrary waveforms at microwave frequencies. An IQ mixer is comprised of two mixers, a 90°phase-shifter, and two 3 dB splitters (Fig. A.3). Base-band pulses are input to the intermediate frequency (IF) ports of the mixers, labeled I and Q. We'll assume that both have frequency, ν_{IF}. These input signals then take the form

$$f_3(t) = f_{\mathrm{Q}}(t) = \cos(2\pi\nu_{\mathrm{IF}}t) \quad \text{and} \quad f_4(t) = f_{\mathrm{I}}(t) = \sin(2\pi\nu_{\mathrm{IF}}t) \tag{A.10}$$

A carrier tone, at microwave frequencies, is input to the local oscillator (LO) port of the mixer. We'll assume that this tone has the form

$$f_0(t) = f_{\mathrm{LO}}(t) = \sin(2\pi\nu_{\mathrm{LO}}t) \tag{A.11}$$

We can now write down an expression for the waveform at each point in the mixer circuit (indicated by the numbered nodes).

$$f_1(t) = \sin(2\pi\nu_{\mathrm{LO}}t+\pi/2) = \cos(2\pi\nu_{\mathrm{LO}}t) \tag{A.12}$$

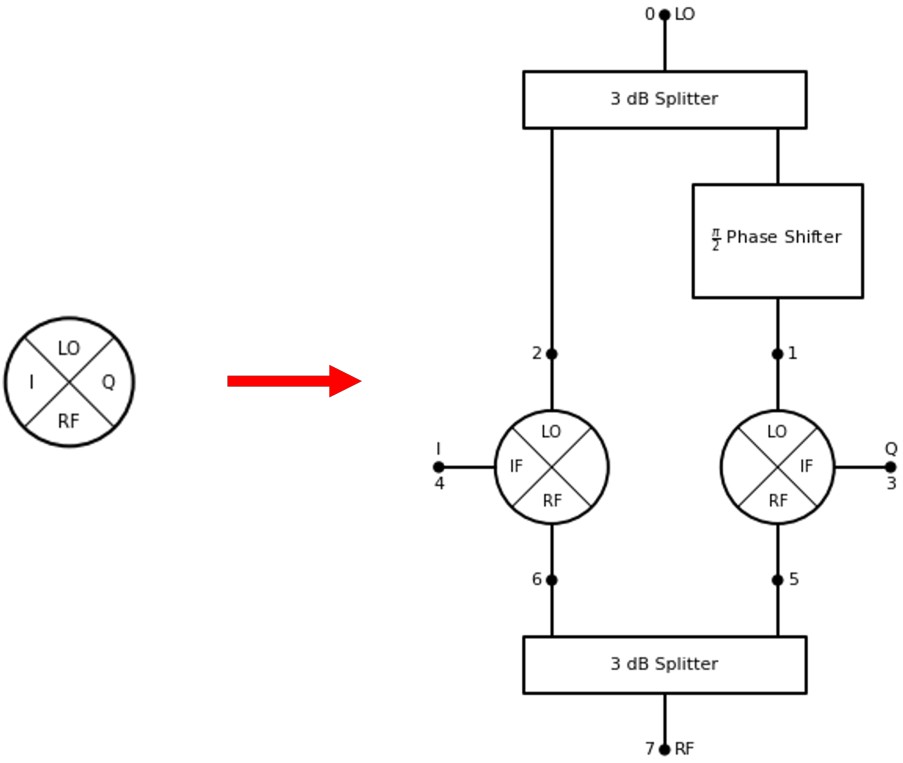

Figure A.3: IQ mixer schematic.

$$f_2(t) = f_0(t) = \sin(2\pi\nu_{\mathrm{LO}}t) \tag{A.13}$$

$$\begin{aligned} f_5(t) &= f_1(t)f_3(t) \\ &= \cos(2\pi\nu_{\mathrm{LO}}t)\cos(2\pi\nu_{\mathrm{IF}}t) \\ &= \frac{1}{2}[\cos(2\pi(\nu_{\mathrm{LO}}+\nu_{\mathrm{IF}})t) + \cos(2\pi(\nu_{\mathrm{LO}}-\nu_{\mathrm{IF}})t)] \end{aligned} \tag{A.14}$$

$$\begin{aligned} f_6(t) &= f_2(t)f_4(t) \\ &= \sin(2\pi\nu_{\mathrm{LO}}t)\sin(2\pi\nu_{\mathrm{IF}}t) \\ &= \frac{1}{2}[\cos(2\pi(\nu_{\mathrm{LO}}-\nu_{\mathrm{IF}})t) - \cos(2\pi(\nu_{\mathrm{LO}}+\nu_{\mathrm{IF}})t)] \end{aligned} \tag{A.15}$$

$$\begin{aligned} f_7(t) &= f_5(t) + f_6(t) \\ &= \cos(2\pi(\nu_{\mathrm{LO}}-\nu_{\mathrm{IF}})t) \end{aligned} \tag{A.16}$$

We see that the signal output from the RF port of the IQ mixer will have a frequencies de-tuned from the carrier frequency by the IF frequency.

We can extend this analysis to the case where we input tones with two frequencies to each of the I and Q ports of the mixer (applicable to the two-tone experiments in Section 11. Assume that waveforms input to the I and Q ports of the mixer now have the form

$$f_3(t) = f_{\mathrm{Q}} = \cos(2\pi\nu_{\mathrm{IF1}}t) + \cos(2\pi\nu_{\mathrm{IF2}}t) \tag{A.17}$$

$$f_4(t) = f_{\mathrm{I}} = \sin(2\pi\nu_{\mathrm{IF1}}t) + \sin(2\pi\nu_{\mathrm{IF2}}t) \tag{A.18}$$

We can calculate the frequency of the signals at nodes 5 and 6 with these new input tones.

$$\begin{aligned} f_5(t) = f_1(t)f_3(t) &= \cos(2\pi\nu_{\mathrm{LO}}t)(\cos(2\pi\nu_{\mathrm{IF1}}t) + \cos(2\pi\nu_{\mathrm{IF2}}t)) \\ &= \frac{1}{2}[\cos(2\pi(\nu_{\mathrm{LO}} + \nu_{\mathrm{IF1}})t) + \cos(2\pi(\nu_{\mathrm{LO}} - \nu_{\mathrm{IF1}})t)] \\ &+ \frac{1}{2}[\cos(2\pi(\nu_{\mathrm{LO}} + \nu_{\mathrm{IF2}})t) + \cos(2\pi(\nu_{\mathrm{LO}} - \nu_{\mathrm{IF2}})t)] \end{aligned} \tag{A.19}$$

$$\begin{aligned} f_6(t) = f_2(t)f_4(t) &= \sin(2\pi\nu_{\mathrm{LO}}t)(\sin(2\pi\nu_{\mathrm{IF1}}t) + \cos(2\pi\nu_{\mathrm{IF2}}t)) \\ &= \frac{1}{2}[\cos(2\pi(\nu_{\mathrm{LO}} - \nu_{\mathrm{IF1}})t) - \cos(2\pi(\nu_{\mathrm{LO}} + \nu_{\mathrm{IF1}})t)] \\ &+ \frac{1}{2}[\cos(2\pi(\nu_{\mathrm{LO}} - \nu_{\mathrm{IF2}})t) - \cos(2\pi(\nu_{\mathrm{LO}} + \nu_{\mathrm{IF2}})t)] \end{aligned} \tag{A.20}$$

Then the waveform at the output of the IQ mixer will be of the form

$$f_7(t) = \cos(2\pi(\nu_{\mathrm{LO}} - \nu_{\mathrm{IF1}})t) + \cos(2\pi(\nu_{\mathrm{LO}} - \nu_{\mathrm{IF2}})t) \tag{A.21}$$

We can see that waveforms with signals detuned from the carrier frequency by each of the input IF frequencies will be output from the mixer. This treatment is a bit naive in that it disregards the amplitude of the waveforms–effectively ignoring the possibility of LO bleedthru and the image sideband.

A.4 Hamiltonian discretization

A.4.1 Method of finite differences

The method of finite differences allows for analytically evaluating the first derivative of a function. This result can further be chained to allow for estimation of the second derivative of that function.

Theorem: For some function, $f(x)$, and sufficiently small discrete steps, a, the second derivative $\partial^2 f(x)/\partial x^2$ can be approximated as

$$\frac{\partial^2 f(x)}{\partial x^2} = \frac{f(x+a) - 2f(x) + f(x-a)}{a^2} \tag{A.22}$$

Proof: From the definition of the first derivative we have that

$$\frac{\partial f(x)}{\partial x} = \frac{f(x+a) - f(x)}{a} \text{ and } \frac{\partial f(x-a)}{\partial x} = \frac{f(x) - f(x-a)}{a}$$

and similarly, we can approximate $\frac{\partial^2 f(x)}{\partial x^2}$ as

$$\frac{\partial^2 f(x)}{\partial x^2} = \frac{1}{a}\left(\frac{\partial f(x)}{\partial x} - \frac{\partial f(x-a)}{\partial x}\right) = \frac{(f(x+a) - f(x)) - (f(x) - f(x-a))}{a^2}$$

which gives

$$\frac{\partial^2 f(x)}{\partial x^2} = \frac{f(x+a) - 2f(x) + f(x-a)}{a^2}$$

A.4.2 Application to eigenenergy problems

Consider a Hamiltonian of the form $H(q, \delta) = T(q) + U(\delta)$ for some kinetic energy, $T(q)$, and potential energy, $U(\delta)$, where q and δ are conjugate variables. Now, assume that the kinetic energy takes the form $T(q) = \alpha q^2$ for some constant, α.

Recall that q and δ are related via the transformation

$$q = -i\hbar\frac{\partial}{\partial\delta}$$

.

Then, the Hamiltonian can be rewritten in terms of δ as

$$H(\delta) = \alpha\hbar^2\frac{\partial^2}{\partial\delta^2} + U(\delta) \tag{A.23}$$

Now if we discretize δ to be a range of linearly spaced values, $(\delta_1, \delta_2, ..., \delta_{n-1}, \delta_n)$, with step size, a, the Hamiltonian can be rewritten as a matrix of the form

$$H(\delta) = \alpha\hbar^2\begin{pmatrix} \partial^2/\partial\delta_1^2 & & & & \\ & \partial^2/\partial\delta_2^2 & & & \\ & & \ddots & & \\ & & & \partial^2/\partial\delta_{n-1}^2 & \\ & & & & \partial^2/\partial\delta_n^2 \end{pmatrix} + \begin{pmatrix} U(\delta_1) & & & & \\ & U(\delta_2) & & & \\ & & \ddots & & \\ & & & U(\delta_{n-1}) & \\ & & & & U(\delta_n) \end{pmatrix}$$

And for sufficiently small step size, a, we can approximate $\partial^2/\partial\delta_i^2$ using the method of finite differences, thus rewriting the Hamiltonian as

$$H(\delta) = \alpha\hbar^2\frac{1}{a}\begin{pmatrix} 2\delta_1 & -\delta_2 & & & -\delta_n \\ -\delta_1 & 2\delta_2 & -\delta_3 & & \\ & & \ddots & & \\ & & -\delta_{n-2} & 2\delta_{n-1} & -\delta_n \\ -\delta_1 & & & -\delta_{n-1} & 2\delta_n \end{pmatrix} + \begin{pmatrix} U(\delta_1) & & & & \\ & U(\delta_2) & & & \\ & & \ddots & & \\ & & & U(\delta_{n-1}) & \\ & & & & U(\delta_n) \end{pmatrix} \tag{A.24}$$

where the elements at the elements, $-\delta_n$ and $-\delta_1$ have been added by hand to enforce cyclic boundary conditions. We now have a matrix for which we can numerically find the

eigenvalues and eigenvectors, remembering, of course that when choosing the step size, a, there is a trade off between the accuracy of the solution and the size of the resulting matrix (which will affect computation time).

This method of solving for the eigenenergies and eigenstates computationally is particularly powerful for systems where the potential is a complicated function depending on only variable, δ, systems which would otherwise be difficult to solve analytically.

The conjugate variables q and δ physically represent charge and phase respectively. Let us consider superconducting circuits consisting of an inductive element (whether that be a linear inductor, a Josephson junction, or some composite element consisting thereof) shunted by a capacitor. We can take the capacitive energy to be the kinetic energy, $T(q) = q^2/2C$, associated solely with the charge, while the inductive energy (potential energy), $U(\delta)$, will be associated with the phase.

The Hamiltonian can then be readily rewritten to be of the form given in Eq. (A.23).

$$H = \frac{\hbar^2}{2C}\frac{\partial^2}{\partial\delta^2} + U(\delta) \tag{A.25}$$

Let us apply the Hamiltonian discretization method for determining the energy eigenvalues and eigenstates to a few relevant examples, starting with one of the simplest superconducting circuits, for which we know the solution: the quantum harmonic oscillator.

Values used to generate each of the plots in this Section are given in Table A.1.

Circuit	E_J	L or E_L	C or E_C	E_2
LC Oscillator	-	8.2 nH	64.5 fF	-
Transmon	20 GHz	-	300 MHz	-
Fluxonium	3.4 GHz	130 MHz	480 MHz	-
$0 - \pi$ / $\cos(2\delta)$	-	-	0.002 K	0.2 K

Table A.1: Parameters used for simulations in this section. Quantities quoted in units of frequency are divided by Planck's constant while those quoted in units of temperature are divided by Boltzmann's constant.

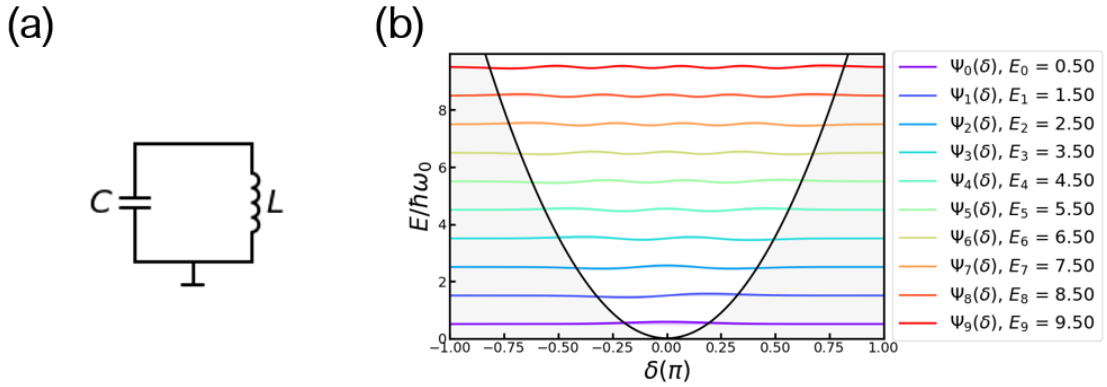

Figure A.4: (a) Circuit representation of the quantum harmonic oscillator. (b) Quantum harmonic oscillator wavefunctions, offset by the energy eigenvalues, superimposed on the harmonic oscillator potential. Energies eigenvalues are normalized by the harmonic oscillator frequency, $\omega_0 = 1/\sqrt{LC}$. The x-axis is normalized such that $\delta = 2\pi\Phi/\Phi_0$ is directly comparable to the phase variable used for the Josephson potential in subsequent sections.

A.4.3 LC oscillator

In this case the potential energy is that of a linear inductor, given by $U(\delta) = \delta^2/2L$. The Hamiltonian then takes the familiar form

$$H(\delta) = \frac{\hbar^2}{2C}\frac{\partial^2}{\partial\delta^2} + \frac{\delta^2}{2L} \tag{A.26}$$

Evaluating Eq. A.24 with this potential, and numerically solving for the eigenvectors and eigenvalues, we solve for the eigenenergies and wavefunctions. The result is shown in Fig. A.4. The wavefunctions are plotted atop the harmonic oscillator potential, offset by the energy, E_n. As expected they take the form $E_n/\hbar\omega = n + \frac{1}{2}$ [64]. From here, we can work through the same analysis for various superconducting qubits.

A.4.4 Transmon

The Transmon [5] closely resembles the LC oscillator, but with a Josephson junction in place of the linear inductor (see Fig. A.5 (a)). Associated with the junction is the

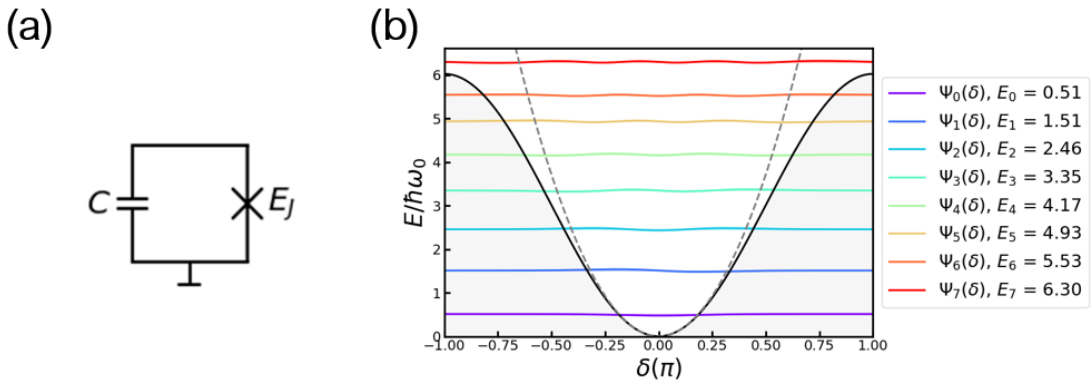

Figure A.5: (a) Circuit representation of the transmon qubit. (b) Wavefunctions of the transmon qubit, offset by the energy eigenvalues, plotted over top of the Josephson potential. The harmonic oscillator potential (grey dashed line) is plotted alongside the Josephson potential. Energies are normalized in this case by the transmon frequency, $\omega_0 = \sqrt{8E_C E_J} - E_C$

Josephson potential, $U(\delta) = -E_J \cos(\delta)$, so the Hamiltonian takes the form

$$H(\delta) = \frac{\hbar^2}{2C}\frac{\partial^2}{\partial\delta^2} - E_J \cos(\delta) \tag{A.27}$$

Again, evaluating Eq. A.24, with the transmon potential, and diagonalizing numerically we find the eigenenergies and wavefunctions (shown in Fig. A.5 (b)). The harmonic oscillator potential is shown as a dashed grey line. We see that when considering only the lowest energy states, the harmonic oscillator is a reasonable approximation of the transmon circuit. We note also, the characteristic anharmonicity of the transmon, a necessity which makes it possible to address only the two lowest lying states, making this circuit suitable for quantum computation.

A.4.5 Fluxonium

Forging ahead with progressively more exotic superconducting qubits, we arrive at the fluxonium [7, 61]. The fluxonium circuit (shown in Fig, A.6 (a)) consists of a Josephson junction in parallel with an inductance and capacitance. The capacitance can either be solely due to the overlap capacitance of the Josephson junction or it there can be an added

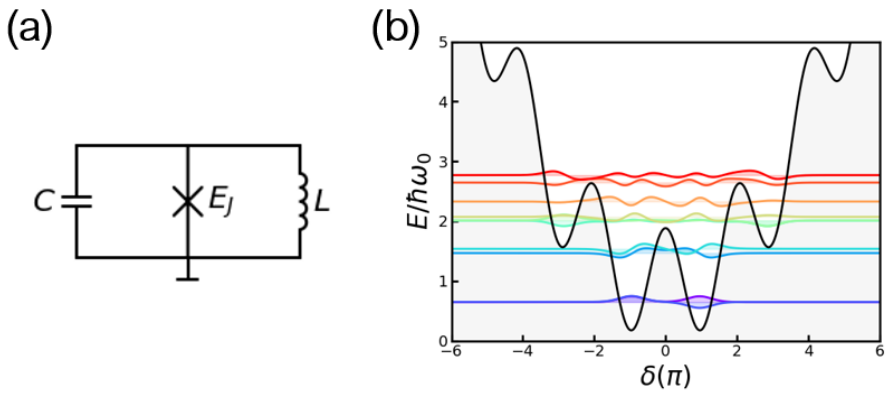

Figure A.6: (a) Circuit diagram of the fluxonium qubit. (b) The Fluxonium potential is plotted shaded in gray. The eigenstates are shown, offset by the eigenenergies.

capacitance [61].

$$H(\delta) = \frac{\hbar^2}{2C}\frac{\partial^2}{\partial\delta^2} - E_J\cos(\delta) + \frac{\delta^2}{2L} \tag{A.28}$$

Again, turning the crank we solve for the eigenenergies and eigenvalues (Fig, A.6 (b)). We see that when considering only the two lowest energy states we will have a double well potential, similar to the $0-\pi$ circuit. Again, the two lowest lying states will be symmetric and anti-symmetric superpositions of wavefunctions localized in the two wells. As a result, long inter-well relaxation times have been demonstrated in capacitvely-shunted or 'heavy' fluxonium qubits [61].

A.4.6 $0-\pi$

The $0-\pi$ qubit has a π-periodic potential, $U(\delta) = -E_2\cos(2\delta)$, as the name suggests.

$$H(\delta) = \frac{\hbar^2}{2C}\frac{\partial^2}{\partial\delta^2} - E_2\cos(2\delta) \tag{A.29}$$

Working through the Hamiltonian discretization in the same way as above (Fig. A.7 (b)), we see that similar to the fluxonium the two lowest-lying energy states will be nearly degenerate superpositions of symmetric and anti-symmetric wavefunctions. Further, we see that we will have energy doublets, and that the splitting between states in a doublet will increase as we approach the top of the potential barrier. This circuit is what we expect

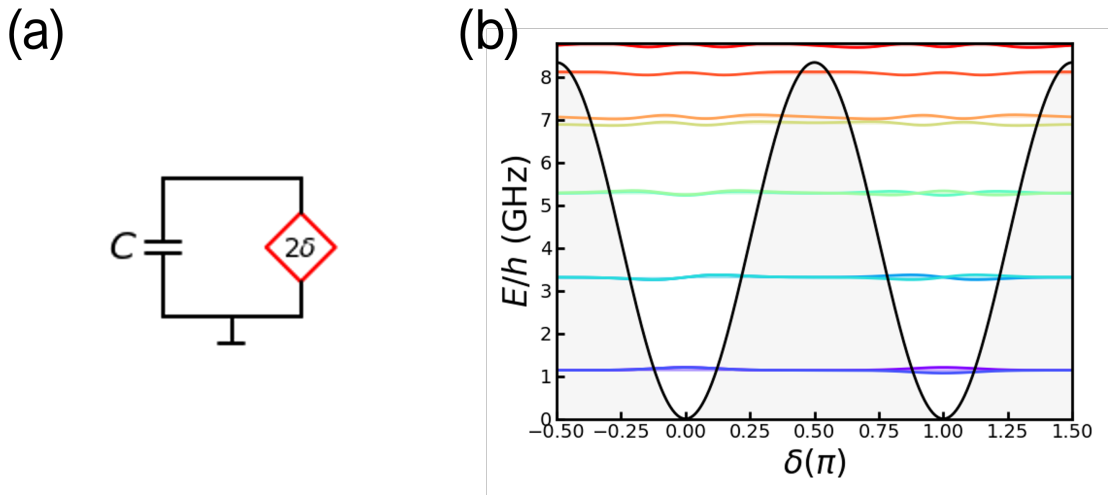

Figure A.7: (a) Charge-parity qubit circuit diagram consisting of a π-periodic Josephson element shunted by a capacitance. (b) The $\cos 2\delta$ potential is shown shaded in gray. The eigenstates of the charge-parity qubit are shown, offset by the eigenenergies.

for a plaquette device biased at exactly $\Phi_0/2$.

Appendix B

Ancillary experimental details

B.1 Josephson junction fabrication

While the procedure for fabricating Josephson junctions is well known in the superconducting qubit community, it may be new for a reader coming from the detector community. As a results, it deserves a detailed discussion. A Josephson junction, that is two superconducting films separated by a weak link, has numerous implementations: as a point contact or constriction, as two superconductors separated by a normal metal or by an insulating barrier, among others [3].

Most commonly used by academic groups in the superconducting qubit community are Al-AlOx-Al Josephson junctions, with the benefit that the two superconducting electrodes and the AlOx tunnel barrier can be deposited / grown in a single tool, without breaking vacuum. Nb junctions are also fairly common, however, they typically require multiple fabrication steps, and the use of a lossy dielectric scaffolding. As a result, the use of Nb junctions is often limited to applications that require a higher gap material than Al, allowing operation at higher temperatures or access to higher frequencies. Recently, superconducting qubits utilizing Nb junctions have reached coherence times of more than 60 μs, corresponding to a quality factor of over 10×10^5 [85, 86]. This was possible due to improvements made to the fabrication process. For the purposes of this thesis, we'll restrict our discussion to Al-AlOx-Al junctions deposited via double-angle evaporation.

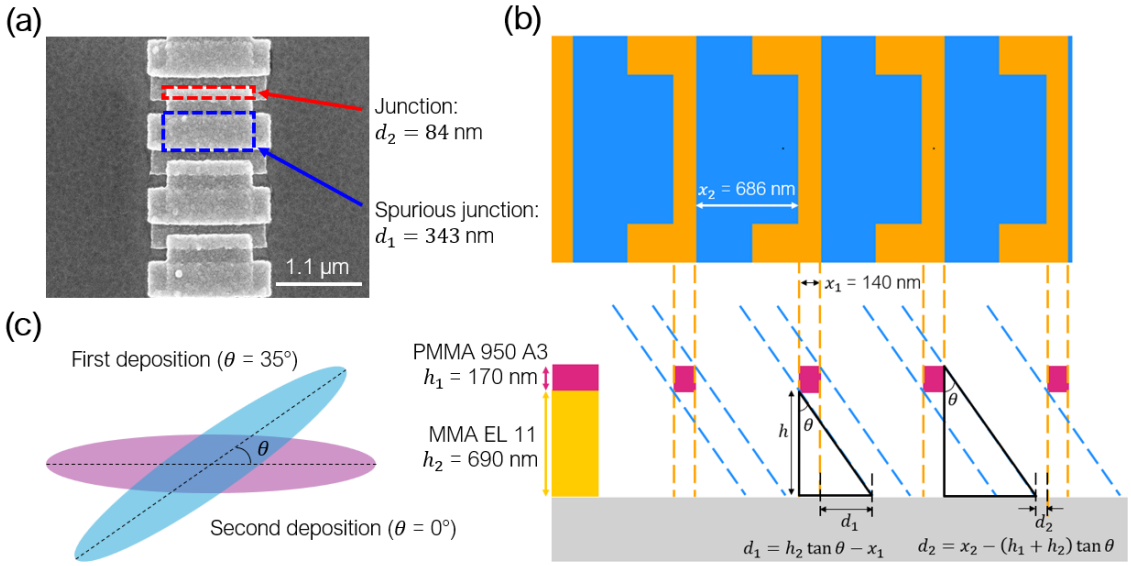

Figure B.1: Josephson junction fabrication details. (a) SEM of an array of large-area Josephson junctions deposited via double-angle evaporation. (b) Top-down view of the e-beam lithography pattern used for creation of the Josephson junctions. Blue regions indicate the 'main' dose and orange regions indicate the 'window' dose. Below, a cross-sectional side-view of the resist stack after development is shown. (c) Wafer orientation during deposition of the bottom electrode (first deposition) and top-electrode (second deposition).

The process for creating Al-AlOx-Al Josepson junctions typically requires the use of an evaporator where one can vary the substrate angle *in situ*, and a resist bridge. The first evaporation takes place at an angle, allowing the metal to be projected forward under the resist bridge. After the bottom-electrode is deposited, the sample is exposed to O_2 gas for a fixed pressure and time in order to grow the insulating oxide barrier. Finally, the top-electrode is deposited with the sample normal to the source, creating the overlap junctions.

The resist bridge is critical for junction fabrication via this method, and it is created with the use of a bi-layer e-beam resist stack. MMA EL 11 underneath PMMA 950 A3 were the resists used for the fabrication of junctions discussed in this thesis. MMA EL 11 can be exposed at a dose that is about one third of the dose required to expose PMMA. As such, one can use window dosing to create an undercut (or bridge) by explicitly exposing the lower MMA layer while leaving the PMMA layer unaffected. A top-view of the pattern

used for creating arrays of Josephson junctions, similar to those used in this thesis is shown in Fig. B.1 (b). The orange regions are areas where the lower 'window' dose is applied while blue areas are where the higher 'main' does is applied, exposing both the MMA and PMMA. After exposure, the pattern is developed in a cold mixture of IPA:DI (3:1) [87]. Cold development is used to increase resist contrast and decrease variations in junction area caused by the roughness of the resist sidewalls. Development was done at 2 C because it was readily achievable with an ice bath. A more robust fabrication process might make use of a chilled circulating bath in order to reach lower temperatures and a more spatially consistent temperature in the developer. The contrast of PMMA has been shown to increase with decreasing temperature down to 17 C [88]. A cross-sectional view of the post-development resist stack is shown on the bottom of Fig. B.1 (b), with the resist bridge shown in pink. The dashed diagonal blue lines show where the first metal layer would be projected. The orange dashed lines show where the second metal layer would be deposited.

After evaporation the excess metal film is lifted-off in NMP at 80 C. It is left untouched in NMP until the excess metal has fully cleared from the surface. The sample is then transferred to a fresh (room-temperature) beaker of NMP and sonicated for 3 min. The sample is subsequently transferred to a beaker of acetone and sonicated for 3 min before being sonicated in IPA for 3 min and finally dried with N_2.

Bibliography

[1] B. Josephson, "Possible new effects in superconductive tunnelling", Physics Letters **1**, 251–253 (1962).

[2] P. W. Anderson and J. M. Rowell, "Probable observation of the josephson superconducting tunneling effect", Phys. Rev. Lett. **10**, 230–232 (1963).

[3] T. Van Duzer and C. W. Turner, *Principles of superconductive devices and circuits* (Elsevier, 1981).

[4] M. Tinkham, *Introduction to superconductivity*, Second (Dover Publications, Inc., 1996).

[5] J. Koch, T. M. Yu, J. Gambetta, A. A. Houck, D. I. Schuster, J. Majer, A. Blais, M. H. Devoret, S. M. Girvin, and R. J. Schoelkopf, "Charge-insensitive qubit design derived from the cooper pair box", Phys. Rev. A **76**, 042319 (2007).

[6] V. Ambegaokar, U. Eckern, and G. Schön, "Quantum dynamics of tunneling between superconductors", Phys. Rev. Lett. **48**, 1745–1748 (1982).

[7] V. E. Manucharyan, J. Koch, L. I. Glazman, and M. H. Devoret, "Fluxonium: single cooper-pair circuit free of charge offsets", Science **326**, 113–116 (2009).

[8] R. L. Kautz, "Picosecond pulses on superconducting striplines", Journal of Applied Physics **49**, 308–314 (1978).

[9] J. Gao, "The physics of superconducting microwave resonators", PhD thesis (California Institute of Technology, May 2008).

[10] R. Barends, "Photon-detecting superconducting resonators", PhD thesis (Technische Universiteit Delft, June 2009).

[11] P. J. de Visser, "Quasiparticle dynamics in aluminum superconducting microwave resonators", PhD thesis (Technische Universiteit Delft, Mar. 2014).

[12] J. Bardeen, L. N. Cooper, and J. R. Schrieffer, "Theory of superconductivity", Phys. Rev. **108**, 1175–1204 (1957).

[13] N. W. Aschroft and N. D. Mermin, *Solid state physics* (Holt, Rinehart and Winston, 1976).

[14] C. Kittel, *Introduction to solid state physics*, Seventh (John Wiley & Sons, Inc., 1996).

[15] D. C. Mattis and J. Bardeen, "Theory of the anomalous skin effect in normal and superconducting metals", Phys. Rev. **111**, 412–417 (1958).

[16] C. M. Wilson and D. E. Prober, "Quasiparticle number fluctuations in superconductors", Phys. Rev. B **69**, 094524 (2004).

[17] M. Lenander, H. Wang, R. C. Bialczak, E. Lucero, M. Mariantoni, M. Neeley, A. D. O'Connell, D. Sank, M. Weides, J. Wenner, T. Yamamoto, Y. Yin, J. Zhao, A. N. Cleland, and J. M. Martinis, "Measurement of energy decay in superconducting qubits from nonequilibrium quasiparticles", Phys. Rev. B **84**, 024501 (2011).

[18] W. L. McMillan, "Transition temperature of strong-coupled superconductors", Phys. Rev. **167**, 331–344 (1968).

[19] W. Eisenmenger, *Nonequilibrium superconductivity, phonons, and kapitza boundaries* (Plenum, New York, NY, 1981).

[20] G. Catelani, R. J. Schoelkopf, M. H. Devoret, and L. I. Glazman, "Relaxation and frequency shifts induced by quasiparticles in superconducting qubits", Phys. Rev. B **84**, 064517 (2011).

[21] S. B. Kaplan, C. C. Chi, D. N. Langenberg, J. J. Chang, S. Jafarey, and D. J. Scalapino, "Quasiparticle and phonon lifetimes in superconductors", Phys. Rev. B **14**, 4854–4873 (1976).

[22] K. C. Gupta, R. Garg, I. Bahl, and P. Bhartia, *Microstrip lines and slotlines*, Second (Artech House, Norwood, MA, 1996).

[23] P. J. de Visser, J. J. A. Baselmans, J. Bueno, N. Llombart, and T. M. Klapwijk, "Fluctuations in the electron system of a superconductor exposed to a photon flux", Nature Communications **5**, 3130 (2014).

[24] A. Megrant, C. Neill, R. Barends, B. Chiaro, Y. Chen, L. Feigl, J. Kelly, E. Lucero, M. Mariantoni, P. J. J. O'Malley, D. Sank, A. Vainsencher, J. Wenner, T. C. White, Y. Yin, J. Zhao, C. J. Palmstrøm, J. M. Martinis, and A. N. Cleland, "Planar superconducting resonators with internal quality factors above one million", Applied Physics Letters **100**, 113510 (2012).

[25] B. A. Mazin, "Microwave kinetic inductance detectors", PhD thesis (California Institute of Technology, Aug. 2004).

[26] S. A. H. de Rooij, "Quasiparticle dynamics in optical mkids: single photon response and temperature dependent generation-recombination noise", MA thesis (Technische Universiteit Delft, 2020).

[27] P. Day, H. Leduc, A. Goldin, T. Vayonakis, B. Mazin, S. Kumar, J. Gao, and J. Zmuidzinas, "Antenna-coupled microwave kinetic inductance detectors", Nuclear Instruments and Methods in Physics Research Section A: Accelerators, Spectrometers, Detectors and Associated Equipment **559**, Proceedings of the 11th International Workshop on Low Temperature Detectors, 561–563 (2006).

[28] J. J. A. Baselmans, F. Facchin, A. Pascual Laguna, J. Bueno, D. J. Thoen, V. Murugesan, N. Llombart, and P. J. de Visser, "Ultra-sensitive THz microwave kinetic inductance detectors for future space telescopes", Astronomy & Astrophysics **665** (2022).

[29] `https://www.3ds.com/products/simulia/cst-studio-suite`, Accessed: 2025-01-24.

[30] O. Rafferty, S. Patel, C. H. Liu, S. Abdullah, C. D. Wilen, D. Harrison, and R. Mcdermott, "Spurious antenna modes of the transmon qubit", arXiv:2103.06803 (2021).

[31] C. H. Liu, D. C. Harrison, S. Patel, C. D. Wilen, O. Rafferty, A. Shearrow, A. Ballard, V. Iaia, J. Ku, B. L. T. Plourde, and R. McDermott, "Quasiparticle poisoning of superconducting qubits from resonant absorption of pair-breaking photons", Phys. Rev. Lett. **132**, 017001 (2024).

[32] F. Deppe, S. Saito, H. Tanaka, and H. Takayanagi, "Determination of the capacitance of nm scale josephson junctions", Journal of Applied Physics **95**, 2607–2613 (2004).

[33] N. A. Gershenfeld, *The physics of information technology* (Cambridge University Press, 2011).

[34] P. J. de Visser, J. J. A. Baselmans, P. Diener, S. J. C. Yates, A. Endo, and T. M. Klapwijk, "Number fluctuations of sparse quasiparticles in a superconductor", Phys. Rev. Lett. **106**, 167004 (2011).

[35] C. R. H. McRae, H. Wang, J. Gao, M. R. Vissers, T. Brecht, A. Dunsworth, D. P. Pappas, and J. Mutus, "Materials loss measurements using superconducting microwave resonators", Review of Scientific Instruments **91**, 091101 (2020).

[36] S. Probst, F. B. Song, P. A. Bushev, A. V. Ustinov, and M. Weides, "Efficient and robust analysis of complex scattering data under noise in microwave resonators", Review of Scientific Instruments **86**, 024706 (2015).

[37] K. Serniak, "Nonequilibrium quasiparticles in superconducting qubits", PhD thesis (Yale University, Dec. 2019).

[38] F. Yan, J. Bylander, S. Gustavsson, F. Yoshihara, K. Harrabi, D. G. Cory, T. P. Orlando, Y. Nakamura, J.-S. Tsai, and W. D. Oliver, "Spectroscopy of low-frequency noise and its temperature dependence in a superconducting qubit", Phys. Rev. B **85**, 174521 (2012).

[39] E. Leonard, M. A. Beck, J. Nelson, B. Christensen, T. Thorbeck, C. Howington, A. Opremcak, I. Pechenezhskiy, K. Dodge, N. Dupuis, M. Hutchings, J. Ku, F. Schlenker, J. Suttle, C. Wilen, S. Zhu, M. Vavilov, B. Plourde, and R. McDermott, "Digital coherent control of a superconducting qubit", Phys. Rev. Appl. **11**, 014009 (2019).

[40] E. Yelton, C. P. Larson, V. Iaia, K. Dodge, G. La Magna, P. G. Baity, I. V. Pechenezhskiy, R. McDermott, N. A. Kurinsky, G. Catelani, and B. L. T. Plourde, "Modeling phonon-mediated quasiparticle poisoning in superconducting qubit arrays", Phys. Rev. B **110**, 024519 (2024).

[41] S. J. C. Yates, J. J. A. Baselmans, A. Endo, R. M. J. Janssen, L. Ferrari, P. Diener, and A. M. Baryshev, "Photon noise limited radiation detection with lens-antenna coupled microwave kinetic inductance detectors", Applied Physics Letters **99**, 073505 (2011).

[42] R. M. J. Janssen, J. J. A. Baselmans, A. Endo, L. Ferrari, S. J. C. Yates, A. M. Baryshev, and T. M. Klapwijk, "High optical efficiency and photon noise limited sensitivity of microwave kinetic inductance detectors using phase readout", Applied Physics Letters **103**, 203503 (2013).

[43] J. Hubmayr, J. Beall, D. Becker, H.-M. Cho, M. Devlin, B. Dober, C. Groppi, G. C. Hilton, K. D. Irwin, D. Li, P. Mauskopf, D. P. Pappas, J. Van Lanen, M. R. Vissers, Y. Wang, L. F. Wei, and J. Gao, "Photon-noise limited sensitivity in titanium nitride kinetic inductance detectors", Applied Physics Letters **106**, 073505 (2015).

[44] J. Bueno, O. Yurduseven, S. J. C. Yates, N. Llombart, V. Murugesan, D. J. Thoen, A. M. Baryshev, A. Neto, and J. J. A. Baselmans, "Full characterisation of a background limited antenna coupled kid over an octave of bandwidth for THz radiation", Applied Physics Letters **110**, 233503 (2017).

[45] L. Ferrari, O. Yurduseven, N. Llombart, S. J. C. Yates, J. Bueno, V. Murugesan, D. J. Thoen, A. Endo, A. M. Baryshev, and J. J. A. Baselmans, "Antenna coupled mkid performance verification at 850 GHz for large format astrophysics arrays", IEEE Transactions on Terahertz Science and Technology **8**, 127–139 (2018).

[46] M. R. Vissers, J. E. Austermann, M. Malnou, C. M. McKenney, B. Dober, J. Hubmayr, G. C. Hilton, J. N. Ullom, and J. Gao, "Ultrastable millimeter-wave kinetic inductance detectors", Applied Physics Letters **116**, 032601 (2020).

[47] T. Guruswamy, D. J. Goldie, and S. Withington, "Quasiparticle generation efficiency in superconducting thin films", Superconductor Science and Technology **27**, 055012 (2014).

[48] J. M. Martinis, "Saving superconducting quantum processors from decay and correlated errors generated by gamma and cosmic rays", npj Quantum Information **7**, 90 (2021).

[49] J. Baselmans, S. Yates, P. Diener, and P. de Visser, "Ultra low background cryogenic test facility for far-infrared radiation detectors", Journal of Low Temperature Physics **167**, 360–366 (2012).

[50] E. Riedel, "Zum tunneleffekt bei supraleitern im mikrowellenfeld", Zeitschrift Naturforschung Teil A **19**, 1634 (1964).

[51] N. R. Werthamer, "Nonlinear self-coupling of josephson radiation in superconducting tunnel junctions", Phys. Rev. **147**, 255–263 (1966).

[52] Y. Nakamura, Y. A. Pashin, and J. S. Tsai, "Coherent control of macroscopic quantum states in a single-cooper-pair box", Nature **398**, 786–788 (1999).

[53] G. Q. AI and Collaborators, "Quantum error correction below the surface code threshold", Nature (2024).

[54] O. Dial, *Eagle's quantum performance progress*, `https://www.ibm.com/quantum/blog/eagle-quantum-processor-performance`, Accessed: 2025-01-15, 2022.

[55] A. G. Fowler, M. Mariantoni, J. M. Martinis, and A. N. Cleland, "Surface codes: towards practical large-scale quantum computation", Phys. Rev. A **86**, 032324 (2012).

[56] D. Gottesman, A. Kitaev, and J. Preskill, "Encoding a qubit in an oscillator", Phys. Rev. A **64**, 012310 (2001).

[57] M. T. Bell, J. Paramanandam, L. B. Ioffe, and M. E. Gershenson, "Protected josephson rhombus chains", Phys. Rev. Lett. **112**, 167001 (2014).

[58] P. Groszkowski, A. D. Paolo, A. L. Grimsmo, A. Blais, D. I. Schuster, A. A. Houck, and J. Koch, "Coherence properties of the 0-π qubit", New Journal of Physics **20**, 043053 (2018).

[59] A. Gyenis, P. S. Mundada, A. Di Paolo, T. M. Hazard, X. You, D. I. Schuster, J. Koch, A. Blais, and A. A. Houck, "Experimental realization of a protected superconducting circuit derived from the 0–π qubit", PRX Quantum **2**, 010339 (2021).

[60] W. C. Smith, A. Kou, X. Xiao, U. Vool, and M. H. Devoret, "Superconducting circuit protected by two-cooper-pair tunneling", npj Quantum Information **6**, 8 (2020).

[61] N. Earnest, S. Chakram, Y. Lu, N. Irons, R. K. Naik, N. Leung, L. Ocola, D. A. Czaplewski, B. Baker, J. Lawrence, J. Koch, and D. I. Schuster, "Realization of a Λ system with metastable states of a capacitively shunted fluxonium", Phys. Rev. Lett. **120**, 150504 (2018).

[62] H. Zhang, S. Chakram, T. Roy, N. Earnest, Y. Lu, Z. Huang, D. K. Weiss, J. Koch, and D. I. Schuster, "Universal fast-flux control of a coherent, low-frequency qubit", Phys. Rev. X **11**, 011010 (2021).

[63] K. Dodge, Y. Liu, A. R. Klots, B. Cole, A. Shearrow, M. Senatore, S. Zhu, L. B. Ioffe, R. McDermott, and B. L. T. Plourde, "Hardware implementation of quantum stabilizers in superconducting circuits", Phys. Rev. Lett. **131**, 150602 (2023).

[64] J. J. Sakurai and J. Napolitano, *Modern quantum mechanics*, Second (Cambridge University Press, 2017).

[65] K. Dodge, "Characterization of superconducting hardware for implementing quantum stabilizers", PhD thesis (Syracuse University, 2022).

[66] Y. Liu, "Design and modeling of superconducting hardware for implementing quantum stabilizers", PhD thesis (Syracuse University, 2022).

[67] T. M. Hazard, A. Gyenis, A. Di Paolo, A. T. Asfaw, S. A. Lyon, A. Blais, and A. A. Houck, "Nanowire superinductance fluxonium qubit", Phys. Rev. Lett. **122**, 010504 (2019).

[68] L. Grünhaupt, M. Spiecker, D. Gusenkova, N. Maleeva, S. T. Skacel, I. Takmakov, F. Valenti, P. Winkel, H. Rotzinger, W. Wernsdorfer, A. V. Ustinov, and I. M. Pop, "Granular aluminium as a superconducting material for high-impedance quantum circuits", Nature Materials **18**, 816–819 (2019).

[69] A. Shearrow, G. Koolstra, S. J. Whiteley, N. Earnest, P. S. Barry, F. J. Heremans, D. D. Awschalom, E. Shirokoff, and D. I. Schuster, "Atomic layer deposition of titanium nitride for quantum circuits", Applied Physics Letters **113**, 212601 (2018).

[70] V. E. Manucharyan, "Superinductance", PhD thesis (Yale University, 2012).

[71] A. Klots, *Super quant model*, `https://github.com/andreyklots/SuperQuantPackage`.

[72] L. D. Landau, "Zur theorie der energieübertragung. ii", Physics of the Soviet Union, Vol. 2, 46–51 (1932).

[73] C. Zener, "Non-adiabatic crossing of energy levels", Proc. R. Soc. Lond. A **137**, 696–702 (1932).

[74] N. Earnest, "Engineering light-matter interactions with metastable states in a heavy fluxonium", PhD thesis (University of Chicago, 2019).

[75] T. Hazard, "Improving quantum hardware: building new superconducting qubits and couplers", PhD thesis (Princeton, 2019).

[76] A. Premkumar, "Hamiltonian and materials engineering for superconducting qubit lifetime enhancement", PhD thesis (Princeton University, 2023).

[77] `https://meetings.aps.org/Meeting/MAR18/Session/F33`, Accessed: 2025-04-20.

[78] `https://meetings.aps.org/Meeting/MAR18/Session/L39`, Accessed: 2025-04-20.

[79] `https://meetings.aps.org/Meeting/MAR24/Session/M48`, Accessed: 2025-04-20.

[80] `https://meetings.aps.org/Meeting/MAR24/Session/N48`, Accessed: 2025-04-20.

[81] A. Opremcak, "High-fidelity measurement of a superconducting qubit using an on-chip microwave photon counter", PhD thesis (University of Wisconsin-Madison, Aug. 2020).

[82] D. Sank, *Q Factor of parallel rlc circuit in series with a capacitor and resistor*, Physics Stack Exchange, URL:https://physics.stackexchange.com/q/139023 (version: 2018-09-18).

[83] D. T. Sank, "Fast, accurate state measurement in superconducting qubits", PhD thesis (University of California Santa Barbara, 2014).

[84] F. Marki and C. Marki, *Mixer basics primer a tutorial for rf & microwave mixers*, tech. rep. (Marki Microwave, 2010).

[85] A. Anferov, K.-H. Lee, F. Zhao, J. Simon, and D. I. Schuster, "Improved coherence in optically defined niobium trilayer-junction qubits", Phys. Rev. Appl. **21**, 024047 (2024).

[86] A. Anferov, S. P. Harvey, F. Wan, J. Simon, and D. I. Schuster, "Superconducting qubits above 20 ghz operating over 200 mk", PRX Quantum **5**, 030347 (2024).

[87] S. Yasin, D. Hasko, and H. Ahmed, "Comparison of mibk/ipa and water/ipa as pmma developers for electron beam nanolithography", Microelectronic Engineering **61-62**, Micro- and Nano-Engineering 2001, 745–753 (2002).

[88] B. Cord, J. Lutkenhaus, and K. K. Berggren, "Optimal temperature for development of poly(methylmethacrylate)", Journal of Vacuum Science & Technology B: Microelectronics and Nanometer Structures Processing, Measurement, and Phenomena **25**, 2013–2016 (2007).